Metal-organic frameworks for water adsorption applications in the automotive filtration industry

DISSERTATION

zur Erlangung des akademischen Grades

Doctor rerum naturalium
(Dr. rer. nat.)

vorgelegt

der Fakultät Mathematik und Naturwissenschaften
der Technischen Universität Dresden

von

Pia Küsgens
geboren am 29. Mai 1981 in Düren

Gutachter
Prof. Dr. S. Kaskel
Prof. Dr. W. Reschetilowski

eingereicht am 07. Oktober 2009
Tag der Verteidigung: 29. Januar 2010

Contents

1. Introduction and motivation **1**

1.1. Porous materials and air drying 2

1.2. Porous materials and diesel drying 5

2. Porous materials **7**

2.1. Metal-organic frameworks - MOFs 8

2.1.1. $Cu_3(BTC)_2$ 9

2.1.2. MIL-101 10

2.1.3. MIL-100(Fe) 11

2.1.4. ZIF-8 11

2.2. Zeolites 12

2.2.1. Zeolite A 14

2.2.2. Zeolite X 15

2.3. Silica gel 16

3. Characterization techniques **18**

3.1. Gas adsorption 18

3.1.1. Fundamentals of adsorption 18

3.1.2. Nitrogen physisorption isotherms 20

3.1.3. Langmuir and BET theory 21

3.1.4. Water adsorption isotherms 22

3.2. Karl-Fischer titration 24

3.2.1. Fundamentals of the Karl-Fischer reaction 24

3.2.2. Coulometric Karl-Fischer method 26

3.3. Instruments and settings 27

4. Preparation of samples **30**

4.1. $Cu_3(BTC)_2$@ceramic 30

4.1.1. Preparation and characterization of $Cu_3(BTC)_2$@ceramic samples 32

4.2. $Cu_3(BTC)_2$ monoliths . . . 37
4.2.1. Manufacturing of $Cu_3(BTC)_2$ monoliths . . . 37
4.2.2. Characterization of $Cu_3(BTC)_2$ monoliths . . . 44
4.3. $Cu_3(BTC)_2$ paper sheets . . . 49
4.3.1. Preparation and characterization of $Cu_3(BTC)_2$ paper sheets . . . 49
4.4. $Cu_3(BTC)_2$@pulp . . . 53
4.4.1. Preparation and characterization of $Cu_3(BTC)_2$@pulp . . . 53

5. Water adsorption **59**
5.1. Water adsorption isotherms . . . 59
5.1.1. Water adsorption isotherms of powdered samples . . . 60
5.1.2. Water adsorption isotherms of molded samples . . . 72
5.2. Water adsorption kinetics . . . 76
5.3. Water stability . . . 81

6. Air drying **84**
6.1. Air drying with commercial samples . . . 87
6.2. Air drying with monolithic samples . . . 89

7. n-Heptane drying **92**
7.1. *n*-Heptane drying isotherms . . . 93
7.1.1. Drying isotherms of $Cu_3(BTC)_2$ . . . 96
7.1.2. Drying isotherms of zeolitic samples . . . 99
7.1.3. Drying isotherms of silica gel . . . 102
7.2. *n*-Heptane and diesel fuel stability . . . 102

8. Summary and conclusion **105**

A. Acknowledgement **115**

List of Figures

1.1. Compressed air braking system 2
1.2. The concept of pressure swing adsorption 3
1.3. Air drying cartridge 4

2.1. Structure of MOF-5 8
2.2. Structure of $Cu_3(BTC)_2$ 9
2.3. Structure of MIL-101 10
2.4. Structure of MIL-100(Fe) 11
2.5. Structure of ZIF-8 12
2.6. Sodalite cages forming different zeolitic frameworks 14
2.7. Silica gel surface with its different types of silanol groups 16
2.8. Structure and formation of silica gel 17

3.1. Lennard Jones potential 19
3.2. Graphical description of physi- and chemisorption 19
3.3. IUPAC isotherms 20
3.4. Nitrogen and water adsorption isotherms - activated carbon 23
3.5. Structure of imidazole 25
3.6. Mettler Toledo DL39 25
3.7. Karl-Fischer generator electrode 26
3.8. Ionic conduction in the Karl-Fischer titration 27

4.1. Picture - NGK cordierite honeycomb 32
4.2. Experimental setup - $Cu_3(BTC)_2$@ceramic sample preparation 33
4.3. Picture - $Cu_3(BTC)_2$@ceramic sample 34
4.4. SEM images - $Cu_3(BTC)_2$@ceramic sample 34
4.5. XRD patterns - $Cu_3(BTC)_2$@ceramic samples 35
4.6. Picture - Lab-scale kneader and ram extruder 38
4.7. Picture - Ram extruding and kneading process 39
4.8. Picture - $Cu_3(BTC)_2$ monolith 40

4.9. Cross-linking of methoxy methyl siloxane ether 42
4.10. Proposed binding mechanism between $Cu_3(BTC)_2$ and binding agent . . 43
4.11. Structure - methyl cellulose 43
4.12. SEM images - $Cu_3(BTC)_2$ monolithic sample 45
4.13. EDX analysis - $Cu_3(BTC)_2$ monolithic sample 46
4.14. TGA - $Cu_3(BTC)_2$ powdered and $Cu_3(BTC)_2$ monolithic samples 46
4.15. XRD pattern - $Cu_3(BTC)_2$ monolithic sample 47
4.16. Paper formation in a *Rapid-Köthen* Sheet Mold 49
4.17. SEM image - $Cu_3(BTC)_2$ paper sheet 51
4.18. Nitrogen adsorption isotherm - $Cu_3(BTC)_2$ paper sheet 51
4.19. XRD pattern - $Cu_3(BTC)_2$ paper sheet 52
4.20. XRD patterns - $Cu_3(BTC)_2$@pulp samples 54
4.21. SEM images - $Cu_3(BTC)_2$@pulp samples 56
4.22. MOF-5 anchored to a carboxylic acid terminated SAM 57

5.1. TGA - $Cu_3(BTC)_2$ samples 60
5.2. Water adsorption isotherms - $Cu_3(BTC)_2$ at 25 °C 61
5.3. Water adsorption isotherms - $Cu_3(BTC)_2$ at 50 °C 62
5.4. Water adsorption isotherms - ZIF-8 at 25 °C 63
5.5. Water adsorption isotherms - ZIF-8 at 50 °C 63
5.6. Water adsorption isotherms - MIL-100(Fe) at 25 °C 64
5.7. Water adsorption isotherms - MIL-100(Fe) at 50 °C 65
5.8. Water adsorption isotherms - MIL-101 at 25 °C 66
5.9. Water adsorption isotherms - MIL-101 at 50 °C 67
5.10. Nitrogen adsorption isotherm - silica gel 68
5.11. Water adsorption isotherms - silica gel at 25 and 80 °C 68
5.12. Hydrolysis of silica gel 69
5.13. Water adsorption on polar surfaces 70
5.14. Water adsorption isotherms - $Cu_3(BTC)_2$ monolithic samples at 25 and 50 °C 73
5.15. Water adsorption isotherms - $Cu_3(BTC)_2$ monolithic samples at 80 °C . . 74
5.16. Water adsorption isotherms - zeolite NaA samples at 25 °C 74
5.17. Water adsorption isotherms - zeolite NaA samples at 80 °C 75
5.18. TG-DSC experimental setup 76
5.19. TGA - powdered and monolithic NaA and $Cu_3(BTC)_2$ samples 78
5.20. Kinetic water adsorption - NaA and $Cu_3(BTC)_2$ powdered samples . . . 79
5.21. Kinetic water adsorption - NaA and $Cu_3(BTC)_2$ monolithic samples . . . 80

5.22. XRD pattern - $Cu_3(BTC)_2$ after contact with water 82

6.1. Flow chart of the air drying test rig 85
6.2. Temporal course of the air drying test rig test procedure 86
6.3. Picture - the air drying test rig 87
6.4. Results of the test rig experiment with silica gel and zeolite NaA commercial samples 88
6.5. Picture - Air drying cartridge with $Cu_3(BTC)_2$ monoliths 89
6.6. Result of the test-rig experiment using $Cu_3(BTC)_2$ monoliths and commercial $Cu_3(BTC)_2$ pellets 90
6.7. Result of the test-rig experiment using zeolite NaA monoliths 91

7.1. *n*-Heptane drying isotherm - $Cu_3(BTC)_2$ at 25 °C 96
7.2. *n*-Heptane drying isotherm - $Cu_3(BTC)_2$ at 80 °C 99
7.3. *n*-Heptane drying isotherm - zeolite NaA at 25 °C 100
7.4. *n*-Heptane drying isotherm - zeolite NaA at 80 °C 100
7.5. *n*-Heptane drying isotherm - zeolite X at 25 °C 101
7.6. *n*-Heptane drying isotherm - zeolite X at 80 °C 102
7.7. *n*-Heptane drying isotherm - silica gel at 25 °C 103

List of Tables

4.1. List of chemicals 31
4.2. Specific surface areas - $Cu_3(BTC)_2$@ceramic samples 36
4.3. Composition of $Cu_3(BTC)_2$ molding batches 39
4.4. Specific surface areas of $Cu_3(BTC)_2$ monolithic samples 48
4.5. Content of $Cu_3(BTC)_2$ in $Cu_3(BTC)_2$ paper sheets 50
4.6. Properties of $Cu_3(BTC)_2$@pulp samples 55

5.1. Total pore volume and heats of adsorption of MOF materials 70
5.2. Water adsorption capacity of NaA and $Cu_3(BTC)_2$ samples 80
5.3. Specific surface areas of $Cu_3(BTC)_2$ after water adsorption at 25, 50 and 80 °C 82

7.1. Data recording of a *n*-heptane drying isotherm 98
7.2. Specific surface areas of $Cu_3(BTC)_2$, zeolite NaA and zeolite X 104

1. Introduction and motivation

Porous materials are due to find their way in everyday life applications. Nowadays, porous materials already had their breakthrough in adsorption processes like gas separation and purification, catalysis and medical applications. Still, there are some fields where porous materials seem to offer long looked-for solutions.

The most popular example is hydrogen storage. In the so-called "Hydrogen Economy" [1], hydrogen is proposed as an alternative transportation fuel to replace fossil fuels. One of the major problems to overcome is the safe and effective storage of the highly volatile gas. Among others, carbon nanotubes are proposed as storage material as well as metal hydrides. Recently, metal-organic frameworks (MOFs) have shown remarkable storage capacities.

As MOFs are due to find their way in industrial applications, other possibilities to employ these promising materials are looked for. In this work, the water adsorption behavior of some new porous materials was investigated. The focus was to evaluate the suitability of these materials regarding technical applications such as the drying of compressed air and diesel fuel. This included the detailed analysis of the water adsorption and desorption behavior, which were used to characterize the materials in-depth. Additionally, the most promising material $Cu_3(BTC)_2$ (BTC = benzene-1,3,5-tricarboxylate) was investigated regarding the suitability for the use in air drying of compressed air streams and the drying of diesel fuel.

The evaluation of these applications craved for a suitable immobilization of $Cu_3(BTC)_2$. At the moment when this work was started, $Cu_3(BTC)_2$ was neither commercially available as powder, nor was there a useful immobilized form of $Cu_3(BTC)_2$ obtainable. Thus, different approaches to deposit the material on different carriers were developed and characterized. In many cases, the new material was compared with known desiccants like hydrophilic zeolites and silica gel. The resulting samples of the materials were characterized regarding their water adsorption, both statically and kinetically. Finally, the materials were classified regarding stability towards water and diesel fuel.

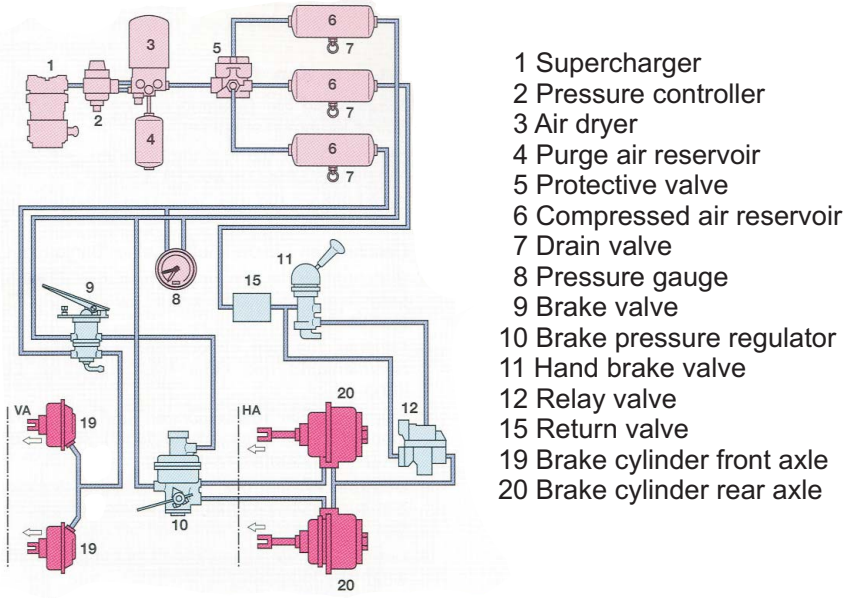

Figure 1.1.: Scheme of a compressed air braking system [2].

1.1. Porous materials and air drying

The automotive industry has long taken advantage of porous materials for different purposes and there are still emerging future applications. These include for example the afore mentioned on-board storage of hydrogen using porous materials like active carbon or MOFs. Nowadays, especially emission control is targeted by using porous materials. One known field where adsorbents are used is the adsorption of gasoline vapors in fuel tanks using so-called carbon canisters, which are filled with active carbon [3]. These adsorb all gasoline vapors during the refueling of the car and diminish fuel vapor emissions, which can emerge at high temperatures during daytime when the vehicle is parked.

Another use is the air drying of compressed air in medium and heavy-duty commercial vehicles [4]. These are usually equipped with compressed air braking systems because of their high weight. The on-board turbocharger generates the required air, which is directly fed into the braking system. To avoid corrosion, freezing or loss of lubricity all water has to be removed from the air stream employing the air drying cartridge. An overview of the braking system with integrated drying unit is shown in figure 1.1.

Adsorption separation processes require an adsorbent that preferentially adsorbs one component from a mixed feet. The driving force in the separation is either based on kinetic or equilibrium selectivity. The process is based on two principal steps. In the adsorption step, the component is removed from the feed. In the desorption or regener-

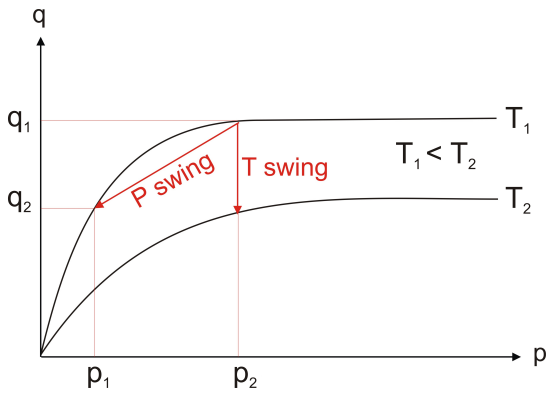

Figure 1.2.: The concept of a PSA and TSA processes. The partial pressure p is plotted against the amount of adsorbed species q.

ation step, the adsorbed species is removed from the adsorbent and the cycle can restart with the adsorption step. Regeneration can be accomplished by a rise in temperature (TSA = Temperature Swing Adsorption) or by a decrease in pressure (PSA = Pressure Swing Adsorption) [5]. The general principle is shown in figure 1.2.

PSA can be operated on a fast cycle, as it is relatively easy to perform the change in pressure compared to other techniques like for example thermal swing. This is a major advantage as the throughput is very high. However, PSA also has its restrictions. The change in pressure may not be too stringent, since the generation of a high vacuum is not economically. Therefore, only components that are not too strongly adsorbed to the adsorbent are suitable for PSA processes.

Air drying processes use the pressure swing adsorption process. An early commercial use is attributed to *C. Skarstrom* as an assignee of *Esso Research and Engineering* (today *Exxon Mobil*), who filed a patent on gas separation by adsorption [6]. Skarstroms invention was followed by *P. Montgareuil*, an assignee of the *Air Liquide Company*, who developed a process for separating binary gaseous mixtures [7]. Today, PSA processes have become an essential technical process in industry, mainly for separation of gases, among them the purification of hydrogen, air separation and air drying. The air drying cartridge is an example of a small scale drying application that applies PSA. Since PSA makes use of a pressure change for regeneration, the air dryer is also known as the so-called *"Heatless Drier"*.

The air drying cartridge usually contains a porous desiccant, mostly silica gel or zeolite molecular sieves. As the whole system has to be small in size, both because of costs and

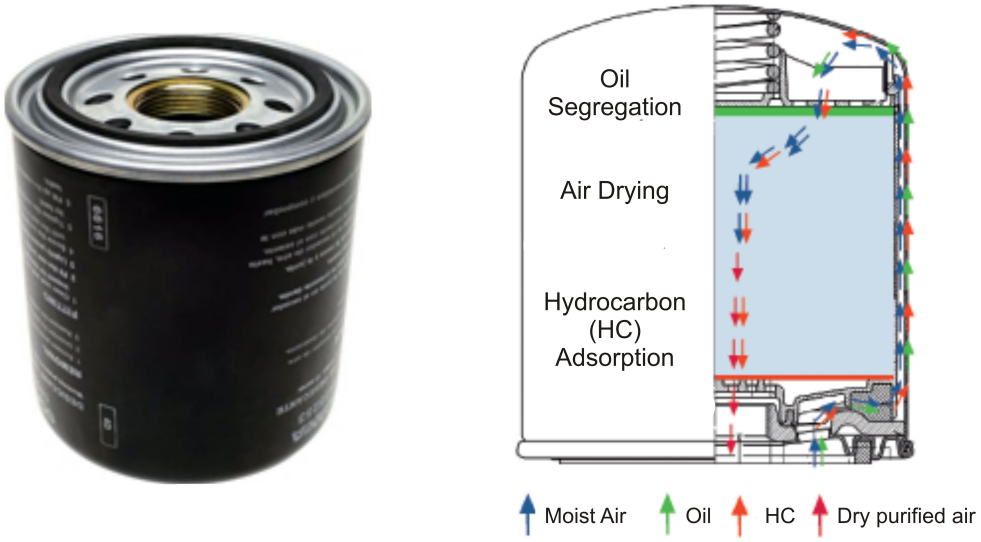

Figure 1.3.: A picture of the air drying cartridge and a sketch of its function.

constructed space, the material should be capable of both adsorbing and desorbing the water coming from the feed stream. The air drying cartridge is constantly recovered by PSA. Figure 1.3 shows the air drying cartridge as well as a rough sketch of its function. Before the humid air enters the desiccant bed (shown in blue), it passes a filter fleece (shown in green) that segregates small oil droplets from the air. After that the moisture is adsorbed in the desiccant bed. An additional function is the adsorption of volatile hydrocarbons that can be formed by the turbo charger due to cracking of the lubricating oil.

The desiccant used in the air drying cartridge usually is silica gel or zeolite shaped to beads (diameter 0.8-2.2 mm). Zeolitic materials are preferred to amorphous silica gel, since they are usually less costly due to the simpler production process. However, silica gels also are advantageous in terms of PSA, as they are more easily reactivated by the pressure swing cycle. The desiccant has to fulfill certain requirements in order to ensure a safe operation of the braking system. The primary goal is the complete removal of moisture from the turbo charged feed stream. The relative humidity of the feed can vary enormously depending on the driving conditions. Thus, one has to presume 100% relative humidity when choosing the appropriate material for drying. Another important property is the efficient regeneration of the adsorbent to ensure an adequate drying performance. Apart from the drying properties, the material needs to provide a low pressure drop to manage high feed streams. The geometrical shape of the drying

agent is therefore of great importance and has to be carefully chosen. Furthermore, the mechanical stability is also of particular concern. As the air dryer is mounted closely to the engine, the beaded bulk material is exposed to extensive mechanical forces. Abrasion can damage the braking system when dust or particles are carried to the machinery. Finally, low production costs of both the raw material and the desired forming into shapes like beads or pellets has to be given.

1.2. Porous materials and diesel drying

In industrial countries, personal mobility and transportation has become a key issue of everyday life. We are living in an environment that totally depends on fast and reliable transport of goods to even remote places. However, the means of transportation require energy in form of combustible fuels, which originate mainly from a petroleum base. Transportation leads to an increased emission production not only in form of exhaust gases like NO_x and CO_2, but also particulate matter (PM). The automotive industry tries to face this problem by developing technologies that support the reduced emission of PM. One striking step was the introduction of the common rail fuel injection system. The new technology operates under high pressure and provides completely electric control. Compared to conventional systems, precise injection of fuel regarding quantity and time is ensured, which automatically leads to reduced emission of PM. However, these systems are highly sensitive and harsh requirements are stated to protect the systems.

Water in diesel fuel is a potential hazard for the injection systems, since it leads to corrosion, reduced lubricity and microbiological growth. Therefore, immiscible or unsolved water has to be removed from the fuel before it enters the injection system. In actual fact, the maximum water content in diesel fuel is specified to 200 ppm [8]. This value is higher for markets with minimal requirements based on fundamental vehicle performance as specified in the World-Wide Fuel Charter of April 2000 with 500 ppm [9]. Although these requirements are fulfilled by the big petroleum groups, water contaminated diesel fuel is of serious concern in some countries. The contamination can occur during transportation or simply by bad housekeeping of the distributing service stations.

The problem is overcome by employing efficient fuel filters with water separating units. The emulsified water droplets approach at a hydrophilic surface of the filter element leading to a coagulation of the droplets. Due to the higher density of water compared to diesel fuel, the water droplets fall into a collecting space that is mounted below the filter element. These diesel filters achieve separation efficiencies of up to 99%. The separated water is usually disposed during maintenance of the vehicles. A newly developed filter

enables the water to be drained during operation; it is no longer necessary to dispose the water during maintenance [10, 11]. This filter consists of an active carbon-cleaning unit that purifies the separated water from all diesel contaminants. As the cleaned water can be drained at any times, maintenance is no longer necessary and operation costs of commercial vehicles are reduced.

Aviation turbine fuels require even harsher conditions regarding water contents. At temperatures below 0 °C, the formed ice can block orifices, screens and filters [12]. Large quantities will even lead to an interrupted fuel flow. Here, the immiscible water is removed by special separating filters with a similar operating mode like the diesel fuel filter [12].

Although the water separating efficiency adds up to almost 99%, an additional drying unit after the water separation is useful to completely secure the injection system from corrosion.

2. Porous materials

According to IUPAC classification (*International Union of Pure and Applied Chemistry*), porous materials are divided into three groups depending on the pore size [13]: Materials with pores larger than 50 nm are called macroporous materials. Mesoporous materials are the second group with pores from 2 to 50 nm in diameter and microporous materials possess pores with diameters of less than 2 nm.

Macroporous materials usually do not have a high specific surface area. The porous structure is rather used as carrier for other porous materials, for example as monolithic support for catalysts. The large pores enhance the performance as they allow high gas streams to pass through them with only minor pressure drops. The preparation of macroporous materials is achieved by using large template molecules or simply by mechanical treatment [14].

Typical representatives of mesoporous materials are aerogels and xerogels. They are usually non-crystalline and have a broad pore size distribution, which makes them less suitable for sieving purposes. However, in 1992 the *Mobil Company* (today *Exxon Mobil*) first managed to synthesize ordered mesoporous silica materials (M41S) with narrow pore size distribution [15]. Mesoporous materials possess high inner surface areas and are thus suitable for the adsorption of large molecules such as enzymes that cannot fit into micropores.

Until the late 1990ies, two classes of microporous materials were dominating. Among them inorganic materials and special microporous activated carbons. The class of inorganic porous materials can be subdivided into several groups, the most prominent of them being alumosilicates (zeolites) and aluminumphosphates. Besides these, there are other crystalline oxides like siliciumalumniumphosphates (SAPOs), metallosilicates, metalloaluminumphosphates and metalphosphates. Recently, the class of microporous materials was expanded by porous metal-organic frameworks (MOFs), which are both highly porous and crystalline. Microporous materials find a large application in catalysis [16] and adsorption processes [17, 18, 20, 21].

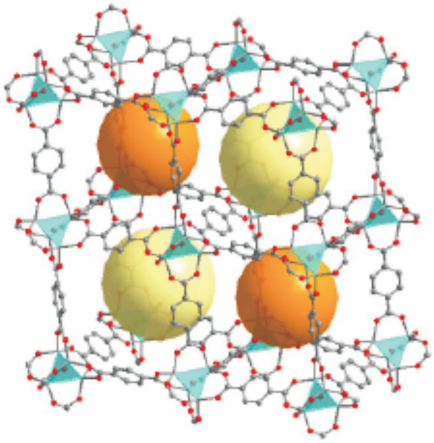

Figure 2.1.: Structure of MOF-5 - Yellow and orange spheres depict the pores.

2.1. Metal-organic frameworks - MOFs

Recently, metal-organic frameworks (MOFs) have received considerable attention in the field of porous materials due to their outstanding properties [22–25]. MOFs are composed of metal-ions combined with polyfunctional organic linkers, a concept that has been known already since the late 1980ies [26].

The synthesis of MOF-5 was one of the milestones in the history of MOFs. This highly porous material is composed of Zn_4O^{6+}-clusters linked with terephtalic acid [27]. The reported specific surface area adds up to $2900\,m^2g^{-1}$ with a pore volume of 0.54-$0.61\,cm^3g^{-1}$. The denomination "MOF" was founded by Omar Yaghi, one of the pioneers in MOF-chemistry, who also reported first on the synthesis of MOF-5 [27]. The structure is shown in figure 2.1.

MOFs are characterized by their high inner surface areas and pore volumes, which exceed those of the known commercial adsorbents like active carbons or zeolite molecular sieves. Moreover, their thermal and chemical stability is quite remarkable. The basic concept of MOF synthesis is the combination of metal-clusters as connectors and polyfunctional ligands as linkers. The transition metals of the first row were shown to be suitable as metal-clusters, but also main group element metals were used recently. The most popular linkers are di-, tri- or tetracarboxylates as well as heterocyclic carboxylates with N-donor function. Combination of these two building blocks yields porous three-dimensional networks with large pore volumes and high inner surface areas. The introduction of a conceptual approach to design predetermined structures that provides the desired material was made by Yaghi and co-workers in 2003. In so-called reticular

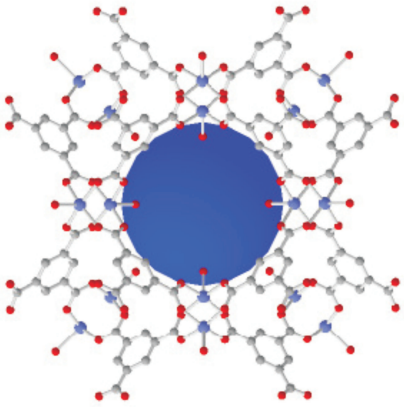

Figure 2.2.: Structure of $Cu_3(BTC)_2$- The blue sphere depicts the large pore.

synthesis [28, 29], rigid molecular building blocks are assembled to the predetermined structure resulting in tailor-made frameworks for specific applications [30, 31]. The pore size for example can be adjusted by choosing the appropriate linker. Still, the pore size is limited to some extent, as the use of long linkers does not always result in a larger pore size, but to interpenetrated or interwoven frameworks with reduced pore size.

MOFs show promising properties regarding hydrogen [18, 21, 32–34], methane [17, 19, 25] or CO_2 storage [35]. Other supposed applications are gas separation [36, 37], catalysis [38–41], separation of isomers [42] or even medical applications [43, 44]. From the time when this work was initiated until today, no commercial application of MOFs is known yet. The fact that most MOF materials are made of synthetically demanding and therefore expensive linkers is one reason why MOFs have not have had their breakthrough in industrial implementation so far. Nevertheless, the *BASF Group* recently developed processes to synthesize some MOFs on a larger scale at reasonable prices. Hence, commercial use does not seem far away [45].

2.1.1. $Cu_3(BTC)_2$

The most popular and most investigated MOF so far is $Cu_3(BTC)_2 \cdot 3\ H_2O$ (BTC = benzene-1,3,5-tricarboxylate) also called HKUST-1 (*HKUST = Hongkong University of Science and Technology*). $Cu_3(BTC)_2$ is among the first MOFs that are commercially available. Its synthesis and structure was reported by Chui et al. [46]. In $Cu_3(BTC)_2$, a binuclear copper complex is linked in a paddle-wheel fashion by the carboxylate linkers yielding a cubic network, which is shown in figure 2.2. It exhibits a bimodal pore size

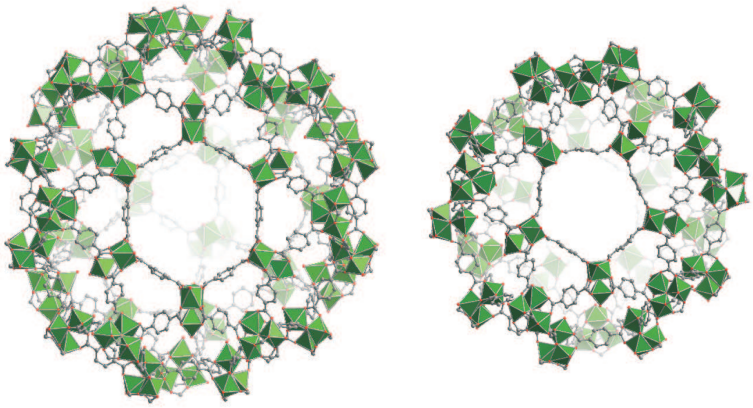

Figure 2.3.: Structure of MIL-101 with the larger cage on the left and the smaller cage on the right. The green octahedra depict the CrO_6 clusters.

distribution with pores of 9 and 6 Å in diameter. The larger and more hydrophilic pore is composed of twelve Cu(COO) subunits whereby the copper sites account for the hydrophilic character. The smaller pore is more hydrophobic as its inner pore walls are constituted only by benzene rings. The pore volume amounts to $0.76\,cm^3g^{-1}$ [19] and the specific surface area can be as large as $1500\,m^2g^{-1}$. The axially coordinated water at the copper sites can easily be removed at elevated temperatures up to 150 °C. The removal ("activation") leads to a color change from deep purple to turquoise blue.

$Cu_3(BTC)_2$ was extensively studied regarding its adsorptive properties. Wang et al. performed studies in gas purification and separation [37]. Other investigations for potential use in catalysis have been made by Schlichte et al. [40]. Here, the cyanosilylation of benzenealdehyde was studied. $Cu_3(BTC)_2$ is also a promising material for hydrogen storage as shown among others by Krawiec [18] and Panella [32].

2.1.2. MIL-101

MIL-101 (Matérial Institut Lavoisier) is one of the MOFs that was discovered by Férey et al. [47]. It is a mesoporous terephtalate. Materials with giant pores are of special interest for applications like gas storage, but are also conceivable for the use in catalysis and drug delivery. The concept of reticular synthesis mentioned before limits the synthesis of materials with large pores because there is the risk of interpenetration. Therefore, MIL-101 is a remarkable example for the advanced design of materials with large pores. The structure is composed of supertetrahedra (ST) as building blocks forming two types of mesoporous cages of 29 and 34 Å in diameter. The structure of these cages is shown in

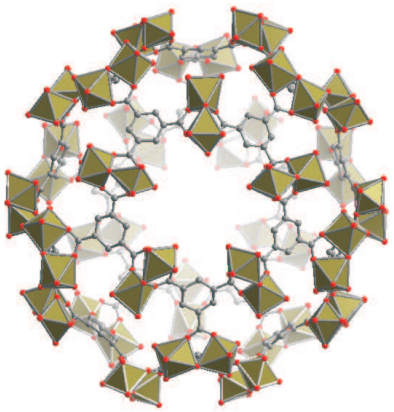

Figure 2.4.: Structure of MIL-100(Fe). The brown octahedra depict the FeO_6 clusters.

figure 2.3. The ST themselves have a microporous character with a pore size of 8.7 Å and consist of three chromium trimers that are connected through the terephtalate linkers. The specific surface area exceeds $4100\,m^2g^{-1}$. Due to the high inner surface area and the mesoporous character, MIL-101 is a good candidate for various applications, such as adsorption of large molecules and catalysis [48].

2.1.3. MIL-100(Fe)

Another mesoporous MOF is MIL-100(Fe) [49], which consists of iron(III)-benzene-tricarboxylate and has been found to be isostructural to MIL-100(Cr) [50]. Like MIL-101 it has two types of mesopores with cages of 25 and 29 Å in diameter. These cages are also formed by ST, which are constructed of iron trimers linked by the tricarboxylate linkers. Here, the pore diameter of the ST is slightly smaller than in MIL-101 with 6.6 Å. The structure is shown in figure 2.4. Nitrogen physisorption experiments revealed a Langmuir surface area larger than $2800\,m^2g^{-1}$. MIL-100(Fe) shows a high activity and selectivity in benzylation of Friedel-Crafts reaction type. As this MOF is based on iron it is much more suitable regarding toxicity for industrial use than copper and chromium MOFs.

2.1.4. ZIF-8

ZIF-8 (Zeolitic Imidazolate Frameworks) belongs to a subgroup of MOFs, in which imidazolates are exclusively employed as linkers [37,51]. ZIF-structures closely resemble zeolitic frameworks, since the transition metal-imidazolate angle is 145° like the Si-O-Si

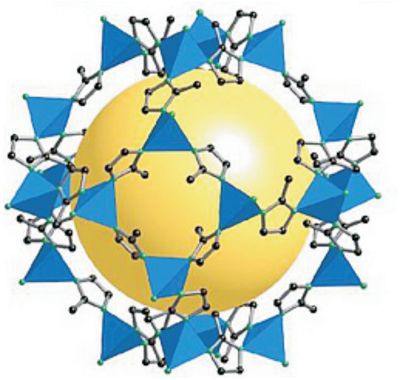

Figure 2.5.: Structure of ZIF-8. The yellow sphere depicts the pore.

angle in the zeolitic network. The possibility of functionalizing the imidazolate linker provides a large structural diversity in ZIF-materials and the syntheses of ZIFs with zeolitic nets have already been achieved [36, 37]. Moreover, ZIFs show a great thermal and chemical stability. The ZIF-8 network shows promising hydrogen storage capacities [52]. In the ZIF-8 network, ZnN_4 tetrahedra are connected through imidazolate linkers forming cages of 11.6 Å in diameter. These apertures are accessible through window openings of 3.4 Å in diameter. The topology is analogous to the SOD topology found in zeolites (Sodalite) [53], except the fact that the pore size of ZIF-8 is about twice as large as in zeolites with SOD frameworks. The structure of ZIF-8 is shown in figure 2.5.

2.2. Zeolites

Zeolites are naturally occurring crystalline porous materials, which are already known since the 18th century. The name originates from Greek and means *"boiling stone"*. In 1756, the Swedish mineralogist *von Cronstedt* named these minerals zeolites when he observed that the material seemed to bop around when heated up rapidly.

Zeolites are microporous alumosilicates that are composed of TO_4 tetrahedra (T =Si, Al), whereas according to *Löwensteins rule* [54], the amount of $AlO^-_{4/2}$ can never exceed the amount of $SiO_{4/2}$ tetrahedra. The ratio of aluminum and silicium fundamentally determines the hydrophilicity and thermal stability of the framework. The negative charge at the aluminum atom requires a cation for compensation resulting in an ion exchange property. The choice of different cations offers the possibility to influence the pore size. Zeolite A for example is available as type 3A (K^+-cations), 4A (Na^+-cations) or 5A (Ca^+-cations) whereby the number approximately describes the pore size.

Zeolites are often called molecular sieves, which refers within adsorption to the cor-

relation of pore size and adsorbed molecule size. Water molecules remain bound to the framework after the synthesis, which can easily be removed giving zeolites their water adsorbing character. The adsorbed water can be reversibly desorbed whereby the framework does not collapse and remains intact. This unique feature differs zeolites from other porous hydrates like $CaSO_4$, whose structure changes upon dehydration. The main composition can be written as follows:

$$M^{m+}_{n/m} \cdot [Si_{1-n}Al_nO_2] \cdot [nH_2O]$$

Zeolites are naturally occurring minerals. Up to now, about forty different structures are known [55], which mostly have a low Si/Al ratio. However, zeolites are also synthetically accessible and structures with low Si/Al ratio as well as almost purely siliceous structures can be synthesized artificially. The first period of prosperity of commercial applications of zeolites and the accompanying investigation of synthetic zeolites started in the 1950ies with large scale syntheses of zeolites by the *Union Carbide Laboratories* (today *UOP*). The cutting-edge research of the synthetic materials was codetermined by Barrer and Breck [56, 57]. The current *Atlas of Zeolite Framework Types* [53] lists 133 zeolitic structures and describes them in-depth. In zeolite nomenclature, every framework type was assigned a three-letter code. Some of these codes refer to the finder of the material or also its structural characteristics. The name of the framework SOD (Sodalite) for example stems from the fact that it is entirely composed of sodalite units. The structural diversity of zeolites is due to a kind of building block approach like in MOF chemistry. Single rigid building blocks (SBUs - secondary building units) are variable linked and thus compose frameworks with different structures and pore sizes. All known structures can be build up by only 18 simple SBUs. Figure 2.6 shows for example how the sodalite subunit can be combined differently to yield three different frameworks. The figure also points out the difficulty in zeolite synthesis: The different combination of the TO_4 subunits can lead to several phases when only one pure phase is desired. Moreover, isostructural frameworks can still possess different characteristics depending on the Si/Al ratio. Zeolite X and Y for example show the same structure, but zeolite X is much more hydrophilic due to its higher aluminum content.

The most suitable route of zeolite synthesis is hydrothermal. Aluminum and silicium sources are mixed together as suspensions, solutions or colloids resulting in an amorphous synthesis gel. In the majority of cases organic templates serve as structure directing agents. Hydroxides are added to enhance the solubility of the Al- and Si-sources. The synthesis gel is mostly an amorphous precipitate, for example an alumosilicate, which is finally crystallized under hydrothermal conditions.

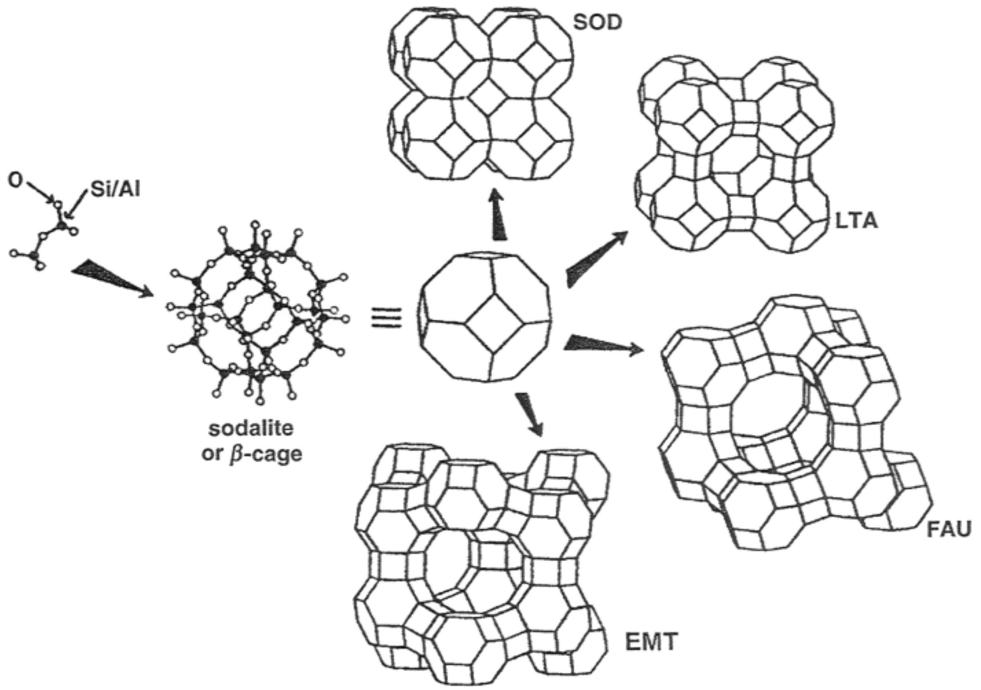

Figure 2.6.: Four different zeolite framework types constructed by the sodalite or β-cages. The sodalite cage unit is found in SOD, LTA, FAU and EMT frameworks [58].

Industrial applications of zeolites are numerous. Among the most important ones within catalysis are the use in catalytic cracking of crude oil distillates or the Fischer-Tropsch synthesis. The adsorption of CO_2 from flue gases or the drying of natural gas are examples for the use in adsorptive applications. The ion-exchange properties lead to the use in detergents to reduce water hardness. Another utilization is within purification, for example the removal of ammonia from wastewater.

2.2.1. Zeolite A

Zeolite A is of structure type LTA (Linde Type A). It is composed of sodalite units, which is shown in figure 2.6. The cages are connected through 4-ring-windows forming a cage composed of eight sodalite units (α − cage), which are accessible via eight-ring-windows (4.1 Å), shown as LTA in figure 2.6. The chemical composition of the sodium type of zeolite A is expressed by the following formula:

$$Na_{12}[(AlO_2)_{12}(SiO_2)_{12}]. 27\ H_2O$$

Zeolite A crystallizes in a cubic fashion ($Fm\bar{3}c$) and exhibits usually a cubic-shaped morphology. It has not been found in nature as mineral and is the first synthetic zeolite

discovered by *Milton* in 1956 [59, 60]. The charge of the anion has to be neutralized by cations, which govern the pore size of the material. The sodium type has a pore size of approximately 4 Å and is therefore named 4A. Consequently, the potassium type is called 3A and the calcium type 5A.

Since the molar ratio of Al/Si in zeolite A is nearly one, it is among the frameworks with the maximum aluminum content possible, if one accepts *Löwensteins rule*. These frameworks are called "low-silica" zeolites. As a consequence, it contains the maximum amount of exchangeable cations balancing the framework aluminum. This composition yields the most heterogeneous surface known among porous materials. The framework is therewith also polar and polarizable giving it excellent water adsorption capacities. The possibility of exchanging the cations represents a possibility to tune the pore size depending on the desired application.

Zeolite A is worldwide the zeolite that is produced in the largest amount due to its application in ion exchange, as desiccant and as molecular sieve in various engineering applications. Isotopic synthetic materials are $AlPO_4$-42, SAPO-42 [61], GaPO-42 and zeolite alpha [62].

2.2.2. Zeolite X

Zeolite X is of structure type FAU (Faujasite) and belongs like zeolite A to the group of "low-silica" zeolites. Its framework is also composed of sodalite cages (see FAU in figure 2.6). In this structure, nine sodalite units are connected through 6-ring-windows yielding an adamantane isomorphous structure. The nine sodalite units form a giant cage, which is accessible through 12-ring windows (7.4 Å). The chemical composition is expressed via the following formula:

$$(Na, Ca, Mg)_{29}[Al_{58}Si_{134}O_{384}]. 240H_2O$$

Zeolite X crystallizes like diamond in a cubic fashion ($Fd\bar{3}m$) and forms octahedral shaped crystals. It is found in nature, but relatively rare, the only known deposits are on Hawaii or at the Kaiserstuhl in Germany. The name Faujasite origins from the French geologist and volcanologist *Faujas De Saint Font* (1741-1819). As already mentioned, zeolite X is a low-silica zeolite with a Si/Al ratio of 1-1.5. Due to its slightly lower alumina content it is less hydrophilic than zeolite A. The larger pore size was the key leading to the introduction of zeolite X as a cracking catalyst.

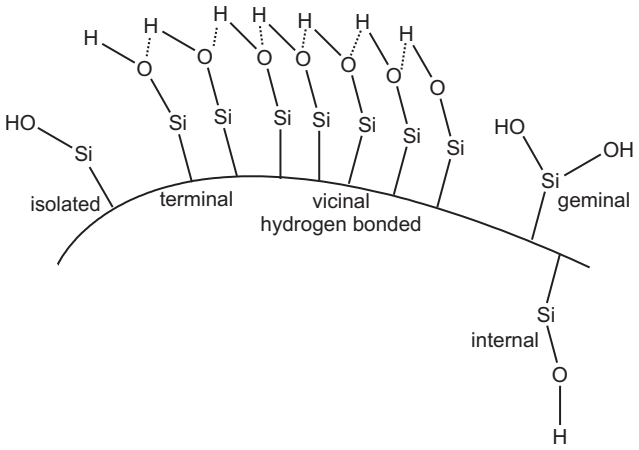

Figure 2.7.: Silica gel surface with its different types of silanol groups.

2.3. Silica gel

Silica gels are the only amorphous porous materials discussed in this work. They belong to the group of synthetic amorphous silica. The pioneering work in the discovery and development of silica gels is mainly attributed to *T. Graham*, who published his first findings on silica gel in 1861 [63]. In 1919, *Patrick* patented the industrial process for manufacturing of silica gels, which was commercialized by the *Silica Gel Corporation* (today part of *W. R. Grace & Co*) [64].

Silica gel is an amorphous porous solid with the following chemical formula:

$$SiO_2 \cdot xH_2O$$

It is composed of randomly linked colloidal silicate particles, the so-called primary particles. The nature of the surface chemistry and the state of aggregation of the primary particles governs the properties of the silica gel. Silica gels are highly porous structures with a hydrophilic surface. The surface chemistry is dominated by the presence of different types of silanol groups, which determine the hydrophilic character (see figure 2.7).

The synthetic route for generating silica gels is mostly of the sol-gel type. It is a wet-chemical method involving sodium silicate as raw material. By mixing an aqueous solution of sodium silicate with aqueous sulfuric acid, the hydrolysis of sodium silicate generates silicic acid, followed by condensation of the latter forming chains, networks and finally gels. The theoretical mechanism is shown in figure 2.8. The surface area, porosity and surface chemistry can be influenced during the production process by adjusting the pH during gel formation. Another possibility is to aftertreat the raw gel by aging,

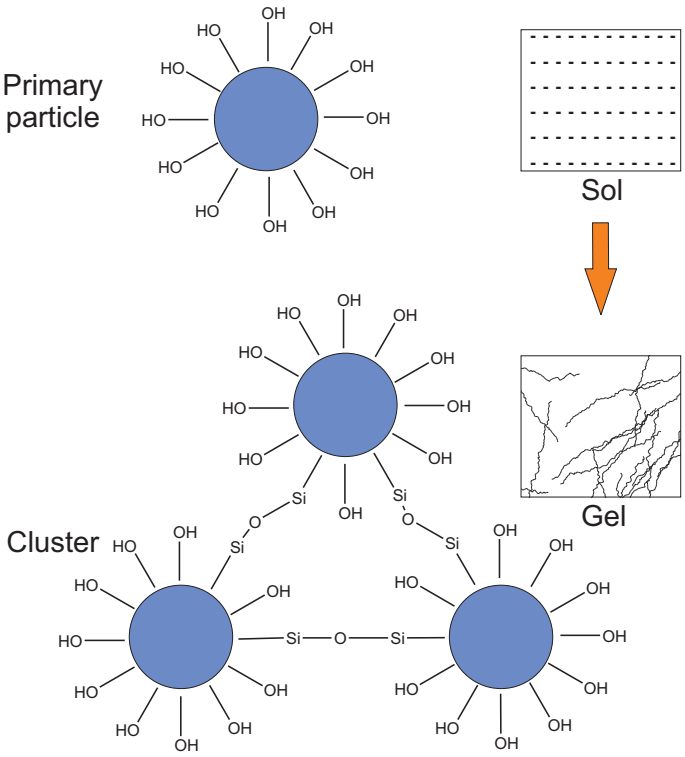

Figure 2.8.: Formation of silica gel. The primary particles condense to clusters forming three-dimensional amorphous networks.

washing and drying [65]. The resulting gel can be quite different in its properties. Drying of silica gel for example can lead to various products depending on drying conditions. Usually, the drying process leads to the formation of a xerogel. When drying occurs under supercritical conditions, the outcome is called aerogel, since almost no shrinkage occurs and air constitutes most of the total volume.

The main difference of silica gels compared to the crystalline materials is their broad pore size distribution. The mean pore diameter can add up to 2-20 nm in average. Other silica gels made from the same raw gel can possess a mean pore diameter of 25 nm. BET-surface areas can vary from 250-1000 $\mathrm{m^2 g^{-1}}$ depending on the treatment of the raw gel. The applications of silica gel are numerous and start with the use in chromatography. Here, it is used as stationary phase in reversed-phase, ion exchange, size-exclusion and affinity-chromatography. They are also used as rheological control additives as they impart a change in viscosity in the liquid phase in which they are suspended. Regarding adsorption applications they are used as ink-receptive coatings or matting agents. The largest area of use is as drying and purification materials.

3. Characterization techniques

In the following chapter, the most important experimental techniques employed in this work are described and the underlying theory is discussed in detail. These are nitrogen physisorption as well as water adsorption and Karl-Fischer coulometry, which were used to characterize the adsorption behavior of the materials in gaseous and liquid phase.

3.1. Gas adsorption

3.1.1. Fundamentals of adsorption

When a fluid (i.e. a gas or liquid) concentrates on a solid surface resulting in an increase in density at the surface compared to the density in the fluid phase it is called adsorption. The adsorbed gas molecules exhibit a minimum in potential energy at approximately one molecular radius from the solid surface. The potential curve for the molecule approaching the solid surface is known as *Lennard-Jones potential* [66]. Figure 3.1 shows the potential energy curve for a physisorbed and chemisorbed gas molecule on a solid surface. The potential is comprised of the contribution of repelling electrostatic forces ($-\mathrm{B}/\mathrm{r}^6$) and the attracting forces ($\mathrm{A}/\mathrm{r}^{12}$) between the gas molecule and the adsorbent. The potential energy passes a minimum when these forces are in equilibrium ($\mathrm{r_g}$). As the adsorption phenomenon increases when an extent amount of surface is present, all industrial adsorbents have specific surface areas greater than $100\,\mathrm{m^2 g^{-1}}$. The nature of both the adsorbent and the adsorbate governs the strength of the interaction. Strong forces between the fluid and the surface lead to chemisorption, which is characterized by the formation of a monolayer on the surface of the adsorbent [66]. Small adsorption enthalpies occur in physical adsorption or physisorption when only weak forces like van der Waals interactions appear between the phases. The formation of multilayers is common in this case. A graphical sketch of both types of adsorption is shown in Figure 3.2.

The most common technique to investigate micro- and mesoporous materials is the isothermal physisorption of gases yielding *adsorption isotherms*. Nitrogen is a suitable adsorbate in this case, as it is non-destructive towards the adsorbent, easy to handle

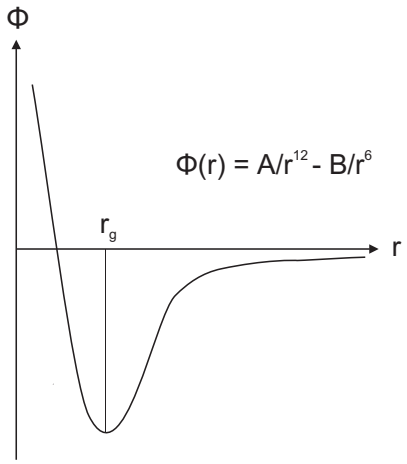

Figure 3.1.: Lennard Jones potential ϕ as a function of the distance of the molecule r to the solid surface as both graphical and mathematical description. A and B are constants.

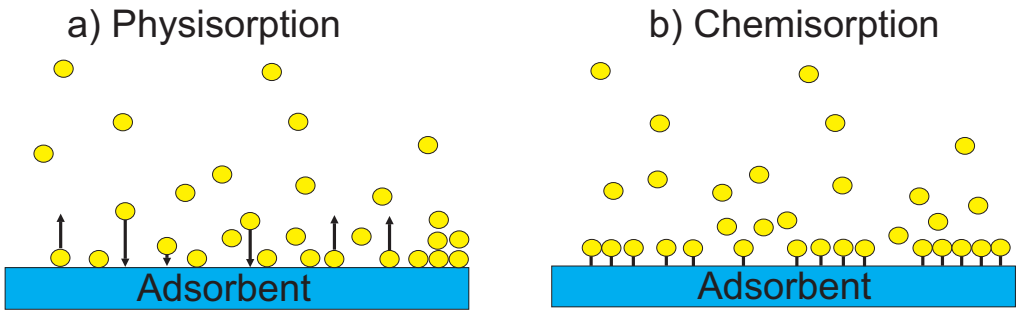

Figure 3.2.: Solid-gas interaction. Figure a) shows the reversible physisorption. Figure b) shows chemisorption where a strong and irreversible bond is formed with the solid surface.

and cheap. With a kinetic diameter of 3.64 Å it can in some cases be too large for some adsorbents as it does not fit in micropores, for example some zeolites. In this case other adsorbents with a smaller diameter like argon (3.44 Å) are used. Water (2.65 Å) can also be an alternative adsorbate in this case, but it often leads to different isothermal forms as it strongly interacts via hydrogen bridging. Additionally, it is unsuitable for adsorbents that are unstable towards moisture. Still, water as adsorbent allows precise characterization of zeolites and other hydrophilic adsorbents.

In a typical nitrogen gas adsorption experiment, the sample is first outgassed under vacuum to remove any adsorbate molecules. The outgassing temperature has to be chosen carefully, since high temperatures might cause partial decomposition, whereas insufficiently high temperature might lead to incomplete outgassing falsifying the result.

The weighed sample cell is then cooled down to 77 K and a defined volume of nitrogen is dosed into the sample cell. When the pressure in the cell is stable, equilibrium is attained. At this moment the first point of the isotherm is recorded as a function of dosed volume to pressure.

3.1.2. Nitrogen physisorption isotherms

Nitrogen adsorption isotherms have a wide variety of shapes depending on the gas-solid systems. Originally, *Brunauer* classified the commonly observed isotherms in five different groups. The classification was extended by IUPAC [67], which grouped the isotherms in six different classes shown in figure 3.3.

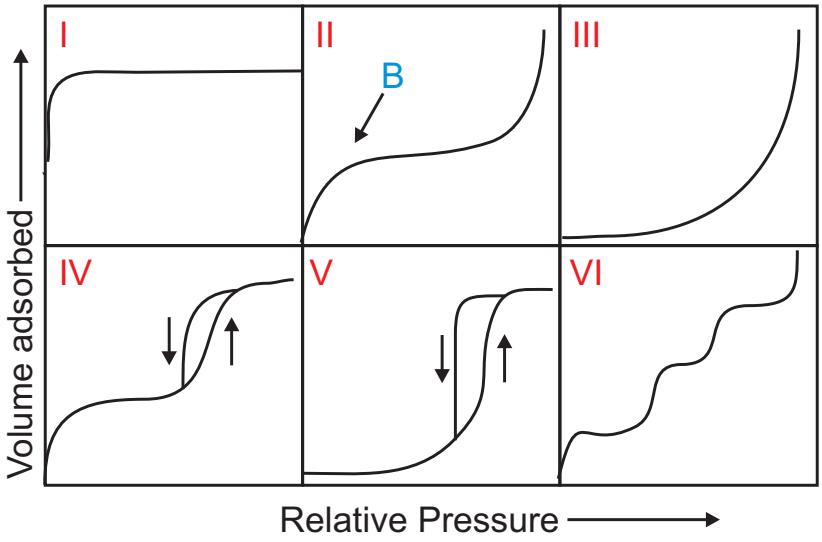

Figure 3.3.: IUPAC-types of physisorption isotherms.

The reversible *type I* isotherm applies to microporous materials showing a steep increase at low relative pressures indicating condensation of adsorbate in the pores. A decrease in the micropore size leads to an increased adsorbent-adsorbate interaction and therewith a micropore filling in the lower p/p_0-region. The total volume adsorbed reaches a saturation value at $p/p_0 = 1$. An almost linear plateau hints at very small external surface area.
The reversible *type II* isotherm is typical for either non-porous or macroporous solids. It is first convex to the x-axis, proceeds to an almost linear shape and turns finally concave to the p/p_0-axis. The formation of monolayer adsorption takes place in the lower pressure region. At point B, monolayer formation is complete and multilayer formation

begins and continues until condensation starts.
The *type III* isotherm is also reversible and characterizes a weak adsorbate-adsorbent interaction. This leads to almost no adsorption in the lower pressure region. Only at high pressures the formation of multilayers can be observed resulting in an isotherm concave to the p/p_0-axis
The *type IV* isotherm exhibits a hysteresis loop in the higher pressure region due to the capillary condensation in mesopores. It is first similar to the *type II* isotherm showing monolayer formation in the lower pressure region followed by multilayer-formation. At relative pressures close to 1, it reaches a saturation value.
The *type V* isotherm is relatively rare and it is similar to the *type III* showing weak adsorbate-adsorbent interactions. Still, there is a porous structure indicated by the hysteresis loop.
The *type VI* isotherm is shown by materials with multi-modal pore size distribution, which show stepwise layer by layer adsorption.

3.1.3. Langmuir and BET theory

The most prominent information that can be determined from the adsorption isotherm besides its IUPAC type is the specific surface area. The first theory was derived by Langmuir [68, 69], who made the following assumptions:

- only monolayer adsorption occurs
- all adsorption sites possess the same energy
- only one molecule can be adsorbed to the adsorption site
- there is no interaction between the adsorbed molecules

The Langmuir equation 3.1, shows how the coverage of adsorbate on the surface depends on the pressure. It can also be expressed in its linear form 3.2, which is used for the calculation of the monolayer volume. As it assumes monolayer coverage it is only sometimes used for microporous materials whose pores are too small for multilayer formation to occur. Chemisorption is based on monolayer formation, which makes the Langmuir theory suitable for the investigation of it.

$$\theta = \frac{\mathrm{k_{ads}\ p}}{\mathrm{k_{ads}\ p + k_{des}}} \tag{3.1}$$

$$\frac{\mathrm{p}}{\mathrm{V}} = \frac{\mathrm{p\ k_{ads}}}{\mathrm{k_{des}\ V_{max}}} + \frac{\mathrm{k_{des}}}{\mathrm{k_{ads}\ V_{max}}} \tag{3.2}$$

with
θ = surface coverage
k_{ads} = gas adsorption rate
k_{des} = adsorbate desorption rate
p = gas pressure
V = volume of adsorbate
V_{max} = volume of monolayer
The *Brunauer-Emmet-Teller* theory (BET-theory) is commonly used to determine the specific surface area for microporous materials. It remains the most used of all adsorption isotherm equations and is based on the following assumptions made by *S. Brunauer*, *S. Emmet* and *E. Teller* in 1938 [70]:

- multilayer adsorption occurs
- the second and all following layers are less strongly adsorbed than the first layer.

Therefore it is somehow an extension of the Langmuir model for multilayer adsorption and describes the *type II* isotherm for mesoporous materials relatively well [70]. Typically, the BET-equation is written in a linear form:

$$\frac{\mathrm{p}}{(\mathrm{p_0}-\mathrm{p})\mathrm{V}} = \frac{1}{\mathrm{aV_{max}}} + \frac{\mathrm{a}-1}{\mathrm{aV_{max}}}\frac{\mathrm{p}}{\mathrm{p_0}} \tag{3.3}$$

with
p = pressure at given temperature
p_0 = saturation pressure at given temperature
V = volume
V_{max} = monolayer volume
a = constant

The measured points will fit a line in case of true multilayer physisorption. The range of the chosen points is usually between p/p_0= 0.05-0.3. The so-called single point BET-equation can be applied in order to shorten the measurement time. In this case, the $(aV_{max})^{-1}$ term equals zero.

3.1.4. Water adsorption isotherms

Water adsorption isotherms are relatively rare compared to nitrogen adsorption isotherms. The fact that water interacts strongly via hydrogen bridges yields completely different

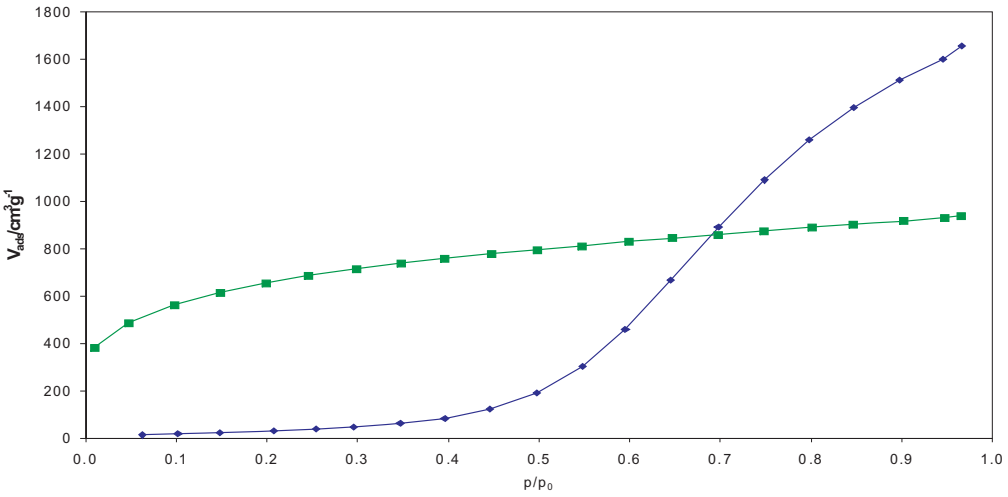

Figure 3.4.: Nitrogen adsorption isotherm recorded at 77 K, shown in green, and water adsorption isotherm recorded at 298 K, shown in blue, of an activated carbon sample.

results as the nitrogen experiment. Moreover, the adsorbate itself can damage the adsorbent if it is not stable towards humidity.

Keeping this in mind, it is not surprising that water is not the adsorbate of choice when it comes to characterization of porous materials by gas adsorption. A prominent example underlining this theory is the characterization of activated carbon. These hydrophobic materials are characterized by nitrogen adsorption to determine the specific surface area and pore volume.

The data in figure 3.4 show both the nitrogen adsorption and the water adsorption isotherm of an activated carbon sample. The typical outcome of the nitrogen experiment depicts a *type I* isotherm as most activated carbons exhibit microporous and mesoporous fractions. The water adsorption isotherm clearly shows a *type V* shape. The surface is here not wetted with the water molecules as these interact here more strongly with each other than with the hydrophobic surface. Adsorption occurs exclusively at primary adsorption locations on and around active sites. With increasing pressure, water molecules form various clusters around these sites by hydrogen bridging. Thus, BET theory cannot be applied to this example, as the major assumption is that molecules wet the surface.

Still, water provides a reasonable method when investigating hydrophilic adsorbents like zeolite molecular sieves with high alumina contents. Here, nitrogen and water isotherms are of the same type according to IUPAC classification. Moreover, water has an advantage over nitrogen as it is smaller in diameter and can also access micropores

that cannot incorporate nitrogen molecules.

In summary, water adsorption isotherms are a useful extension to nitrogen adsorption isotherm already hinting at possible applications of the material: Estimation of hydrophilicity of the adsorbent is the main point when applying water adsorption.

3.2. Karl-Fischer titration

Karl-Fischer titration is a classic analyzing technique for the determination of water in liquids. Depending on the water content, either coulometric or volumetric methods are applied.

3.2.1. Fundamentals of the Karl-Fischer reaction

R. Bunsen [71] described a reaction that can be used to determine the water content in liquid phases:

$$I_2 \ + \ SO_2 \ + \ 2\ H_2O \ \longrightarrow \ 2\ HI \ + \ H_2SO_4 \tag{3.4}$$

K. Fischer discovered that this reaction is suitable for water determination in non-aqueous systems with methanol as an appropriate solvent [72]. In order to shift the equilibrium to the right he used pyridine (Py) as a base to neutralize the acids, which are formed during the reaction.

$$I_2 \ + \ SO_2 \ + \ 3\ Py \ + H_2O \quad \longrightarrow \quad 2\ Py - H^+I^- \ + \ Py \cdot SO_3 \tag{3.5}$$

$$Py \cdot \ SO_3 \ + \ CH_3OH \quad \longrightarrow \quad Py - H^+CH_3SO_4^- \tag{3.6}$$

As shown in reaction 3.6 methanol directly participates in the reaction and does not only function as a solvent. In an alcoholic solution, the reaction of water and iodine takes place in a stoichiometric ratio of 1:1. Further studies of *E. Barenrecht* and *J. Verhoff* [73] showed that the Karl-Fischer reaction rate (3.7) depends on pH-value. A pH-range of 5.5-8.5 yields ideal conditions for the Karl-Fischer reaction, as almost all sulfur dioxide is present as methyl sulfite ions and the reaction rate obtains its maximum.

$$-\frac{d[I_2]}{dt} = k[I_2][SO_2][H_2O] \tag{3.7}$$

The relation of pH-value and reaction rate is not caused directly depending on the sulfur dioxide that is oxidized by iodine, but the formation of the methyl sulfite ion, which is formed from sulfur dioxide and methanol according to the following reaction scheme:

$$2\ CH_3OH \ + \ SO_2 \ \longrightarrow \ CH_3OH_2^+ \ + \ CH_3OSO_2^- \tag{3.8}$$

Furthermore they found that pyridine is only reacting as a buffer in the system and can therefore be replaced by other bases.

Based on these findings, in 1984 *E. Scholz* developed a pyridine-free Karl-Fischer reagent with imidazole as a base [74, 75]. Imidazole has two advantages over pyridine, as it is less toxic and also buffers in a more favorable pH-range than pyridine making the reaction much more accurate. Additionally, he discovered that methanol could be replaced by other alcohols such as ethanol, 2-propanol or ethoxyethanol. Scholz's findings led to the following reaction scheme for the Karl-Fischer titration:

$$\mathrm{ROH} + \mathrm{SO_2} + \mathrm{RN} \longrightarrow (\mathrm{RNH}) \cdot \mathrm{SO_3R} \tag{3.9}$$

$$(\mathrm{RNH}) \cdot \mathrm{SO_3R} + \mathrm{I_2} + \mathrm{H_2O} \longrightarrow (\mathrm{RNH}) \cdot \mathrm{SO_4R} + 2\,(\mathrm{RNH})\mathrm{I} \tag{3.10}$$

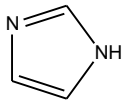

Figure 3.5.: Imidazole = RNH

The development of the pyridine free reagent with imidazole as buffer (Figure 3.5) was a milestone in the use of the Karl-Fischer titration. Imidazole is predominantly used in both Karl-Fischer techniques.

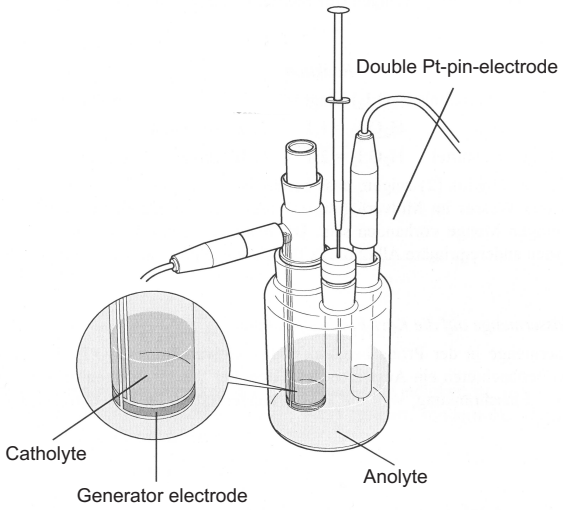

Figure 3.6.: Mettler Toledo Karl-Fischer Coulometric Titrator DL 39 [118].

3.2.2. Coulometric Karl-Fischer method

Volumetric vs. coulometric method

In this work, coulometric Karl-Fischer titration was used to determine the water content of n-heptane samples. Compared to volumetric Karl-Fischer titration, where the titrant is added externally to the reaction vessel by using a burette, the coulometric method makes use of the electrochemical in-situ generation of the titrant. Since the coulometric method allows the generation of small increments it is extremely accurate. For example, the formation with a constant current flow of 10 μA for 10 ms generates only 10^{-8} mol of titrant. These circumstances allow determination of water contents from 1 ppm to 5 %. The volumetric method is suitable for the determination of higher water contents ranging from 5-100%.

Coulometry

One Coulomb is the amount of electric charge transported in one second by a steady current of one ampere:

$$1C = 1A \cdot 1s \tag{3.11}$$

A chemical reaction with single electron transfer requires 96485 C. Regarding the Karl-Fischer reaction, two electrons are needed to generate iodide from iodine. Iodine reacts in the presence of water meaning that 1 mol of water needs 2 x 96485 C. In coulometry, current (ampere) and time (seconds) are measured to calculate the amount of water present in the sample. Figure 3.6 shows a sketch of a typical Karl-Fischer coulometer, in this case the DL39 from Mettler-Toledo. The titration vessel is composed of two

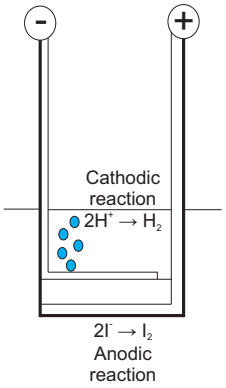

Figure 3.7.: Karl-Fischer generator electrode.

main parts, the anodic and cathodic region. The anodic reaction oxidizes the iodide in

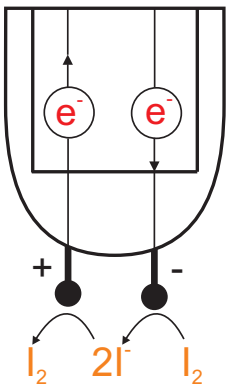

Figure 3.8.: Ionic Conduction - Iodide withdraws an electron at the negatively charged electrode and is reduced to iodine. The iodine releases an electron and is again oxidized to iodide.

the anolyte to iodine, which then reacts with water according to equation 3.10. The cathodic reaction reduces protons to hydrogen, a detailed sketch is shown in figure 3.7.

Indication

The indication of the coulometric Karl-Fischer titration is carried out bivoltrametrically. A small constant current (usually 2 μA) is applied to a double platinum pin electrode (measuring electrode, see figure 3.6). As long as there is water present in the reaction vessel, no free iodide is present. After all water has reacted, free iodide will be present in the solution leading to an ionic conduction, see figure 3.8. In order to keep the current constant, the voltage has to be reduced. The drop in potential that is detected at the pin electrode leads to the termination of the reaction.

3.3. Instruments and settings

Nitrogen Physisorption

Nitrogen physisorption was measured at 77 K using a Quantachrome NOVA 2000 apparatus or a Quantachrome Quadrasorb apparatus. Prior to the measurement, the samples were outgassed under vacuum at 120-200 °C for at least 8 hours. The BET specific surface area was typically calculated in the pressure range of p/p_0= 0.05-0.3.

Water Adsorption

Water adsorption was measured at 298 K or 323 K on a Quantachrome Hydrosorb 1000 apparatus with an equilibration time of 60 seconds. Prior to the measurements, the samples were outgassed under vacuum at 120-200 °C for at least 8 hours. The BET specific surface area was typically calculated in the pressure range of p/p_0= 0.05-0.3. The heats of adsorption were calculated via the Quantachrome^{TM} software Hydrowin.

Karl-Fischer Coulometry

Water content was measured using a Mettler Toledo DL39 Karl-Fischer Coulometer. At least 5 ml of sample was analyzed. Prior to analysis, the sample syringe was rinsed with 2 ml of sample. The mixing time prior to analysis was 10 seconds. The stirring speed of the stirrer was set to 40 rpm. A maximum titration time of 300 sec was chosen. A slow titration rate was applied. As both anolyte and catholyte, Riedel-de-Häen Coulomat AG-H was used. It was mixed with 30% (v/v) of octanol (Applichem). The octanol was dried beforehand over 4A molecular sieve for at least 12 hours.

X-ray diffraction

Powder X-ray diffraction (XRD) patterns were recorded using a Stoe Stadi-P diffractometer and Cu $k_{\alpha 1}$ radiation (λ=0.15405 nm) with a position sensitive detector.

Scanning electron microscopy and energy dispersive X-ray spectroscopy

Scanning electron micrographs (SEM) and energy dispersive X-ray spectroscopy (EDX) were recorded using a Tescan Vega TS5136 XM. Prior to the recordings, the samples were vapor-coated with carbon using a Biorad Polarion Division SEM Coating System.

Thermal gravimetric analysis

Thermal gravimetric analysis (TGA) was performed using a Perkin Elmer TGA7 apparatus with a heating rate of 10 K/min and a gas stream of 20 ml/min (synthetic air).

Thermal gravimetric analysis with coupled differential scanning calorimetry

Thermal gravimetric analysis with coupled differential scanning calorimetry TG-DSC was performed using a Setaram Instrumentation TG-DSC 111 with a B111 microbalance.

Nitrogen gas streams were regulated using Wagner EL-Flow mass flow controllers (50 ml flow type F-201CV-050-RA and 100 ml flow type F-201C-RAD)

Mechanical stability tests

The crushing strength was measured using a Zwick 1455 using a 1000 N force sensor. The preliminary test force was set to 0.5 N. All samples were cut in pieces (dimensions 3.5 x 5 x 8 mm).

4. Preparation of samples

Porous materials synthesized hydrothermally are mostly generated as fine-particle powders. The materials discussed in this thesis have particle sizes from $3 \leq d_p \geq 8$ nm. For the use in any process and chemical engineering facility or apparatus it is indispensable to provide the material in appropriate shape or form, for example as beads, pellets, monoliths or as thin films on suitable carrier materials. The chosen type of form has to provide both the appropriate mechanical stability and a high secondary surface area to ensure a low pressure drop and therewith enhance performance. Another important point is of course a simple and low-cost production process. Therefore the thorough use of expensive materials has to be avoided as well as extensive production processes and pricy carrier materials. In the following section, different possibilities and solutions to form these powders into a useful shape are described and discussed.

4.1. $Cu_3(BTC)_2$@ceramic

Several research groups already made approaches to deposit thin films on different carriers. The carriers were made of α-alumina [76, 77] or copper mesh [78]. Other suitable carriers for porous materials are monoliths made of ceramic materials. They are less costly than copper mesh, easy to form into shaped bodies and have a low weight. They are already known from catalytic applications for example as catalyst carriers for exhaust gas reduction in three-way catalytic converters. They are usually macroporous themselves and have a high surface area due to their thin honeycomb-like channels. Catalysts are deposited on these structures through wash-coating procedures. The advantage of monoliths is the high mechanical stability and the advantageous volume to surface ratio. The high mechanical stability leads to low abrasion, which can be a problem in packed beds where beads are employed. Another benefit of this structure is the low flow resistance and the resulting low pressure drop. The following section describes the deposition of $Cu_3(BTC)_2$ crystals on cordierite monoliths. The samples were generously supplied by the company *NGK*, see figure 4.1.

Chemical (Formula)	Purity	Supplier
Benzene-1,3,5-tricarboxylic acid ($H_3(BTC)_2$)	$\geq$ 97%	Sigma Aldrich
Copper(II) nitrate hemipentahydrate ($Cu(NO_3)_2 \cdot 2.5H_2O$)	$\geq$ 98%	Merck KGA
N,N-dimethylformamide (C_3H_7NO)	98.5 %	Merck KGA
Ethanol (CH_3OH)	$\geq$ 99.5%	Merck KGA
Dichloromethane (CH_2Cl_2)	$\geq$ 99.8%	Merck KGA
Sodium hydroxide (NaOH)	$\geq$ 99%	Merck KGA
Diethyl ether (CH_3OCH_3)	$\geq$ 99.7%	Merck KGA
Silres MSE 100 ($(CH_3Si(O)_{1.1}(OCH3)_{0.8}$)	-	Wacker-Chemie GmbH
Culminal MHPC 20000 P	-	Hercules Aqualon
Basolite^{TM}C300 ($Cu_3(BTC)_2$)	-	BASF
Fe-powder (Fe)	$\geq$ 99.5%	Merch KGA
Hydrofluoric acid (HF)	-	Merck KGA
Nitric acid 65 % (HNO_3)	p.a. ISO	Roth
1,4-benzene dicarboxylic acid ($H_2(BDC)$)	$\geq$ 98%	Merck KGA
Chromium nitrate nonahydrate ($Cr(NO_3)_3 \cdot 9H_2O$)	$\geq$ 98%	Sigma Aldrich
Basolite^{TM}Z1200 (ZIF-8)	-	BASF
n-Heptane (C_7H_{14})	$\geq$ 99%	Prolabo VWR
n-Octanol ($C_8H_{17}OH$)	p.a. ISO	Applichem
Coulomat AG-H (Karl Fischer analyte)	-	Riedel-de-Häen
Nitrogen (N_2)	5.0	Air Liquide

Table 4.1.: List of chemicals

Figure 4.1.: Cordierite monolith, supplied by the company *NGK*.

4.1.1. Preparation and characterization of $Cu_3(BTC)_2$@ceramic samples

Experimental

The synthetic procedures used to prepare the $Cu_3(BTC)_2$@ceramic samples are based on the methods according to *Kaskel* [40] and *Yaghi* [79]. However, there were slightly modified as described in the following.

1. Benzene-1,3,5-tricarboxylic acid (0.89 g, 4.25 mmol) and copper(II) nitrate hemipentahydrate (1.66 g, 6.9 mmol) were stirred for 15 minutes in 120 ml of solvent consisting of equal parts of DMF (N,N-dimethylformamide), ethanol and deionized water in a 250 ml polyethylene bottle. The pretreated cordierite honeycomb (1 x 1 x 1 cm) was tied to a piece of yarn, which was attached to the bottle cap (see figure 4.2). By doing so, the honeycomb was hanging freely in the reaction solution. The bottle was then placed in an oven at 85 °C for 20 hours to yield small octahedral crystals. The resulting sample was taken out and rinsed with DMF and dichloromethane. The sample was treated with ultrasonic sound for 10 minutes to ensure a complete removal of crystals that only precipitated on the surface. Finally, the samples were immersed in dichloromethane for three days. The dichloromethane was freshly replenished every day. The sample was taken out and dried briefly in air before it was activated at 120 °C for several hours. The same procedures were performed using a 400 ml stainless steel vessel (Parr Instruments) with an external heating jacket. The vessel was equipped with a magnetic stirrer with a speed of 150 rpm.

2. Benzene-1,3,5-tricarboxylic acid (2.523 g, 12 mmol) was solved in 70 ml of ethanol. Copper(II) nitrate hemipentahydrate (5.192 g, 22 mmol) was solved in 70 ml of deionized water. Both solutions were mixed in a 400 ml stainless steel vessel (Parr Instruments). A pretreated cordierite honeycomb (1 x 1 x 1 cm) was tied to a piece of yarn and attached to the lid of the vessel. By doing so, the cordierite was hanging freely in the reaction solution. The vessel was heated to 120 °C and held at this temperature for 24 hours. After the solution had cooled down to room temperature, the cordierite honeycomb was taken out and rinsed several times with ethanol. The sample was treated with ultrasonic sound for 10 minutes to ensure a complete removal of crystals that only precipitated on the surface. Finally, it was briefly dried in air before it was activated at 120 °C for several hours.

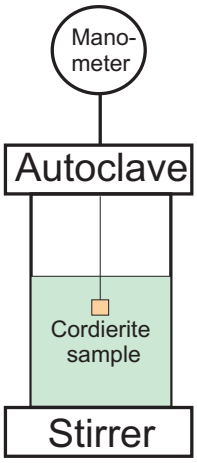

Figure 4.2.: Experimental setup of the $Cu_3(BTC)_2$@ceramic sample preparation.

Pretreatment of samples

Various attempts were made in order to enhance the deposition of $Cu_3(BTC)_2$ on the honeycomb samples. In the first attempt, the synthesis procedure was changed from the Yaghi procedure to the one according to Kaskel. In another approach all samples were pretreated with sodium hydroxide solutions with different concentrations. The samples were immersed in solutions of 2.5 M, 5 M and 10 M sodium hydroxide solution, respectively for one hour. They were taken out, rinsed with ethanol and dried in air prior to synthesis. A third experiment comprised the pretreatment of all samples with diethyl ether for 15 minutes to free them from fat or other impurities. None of the attempts led to a change of the XRD patterns shown in figure 4.5, the crystal growth of $Cu_3(BTC)_2$

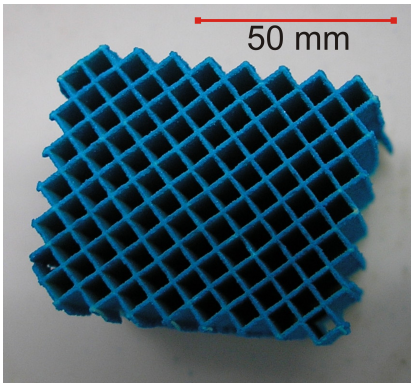

Figure 4.3.: Picture of a $Cu_3(BTC)_2$@ceramic sample.

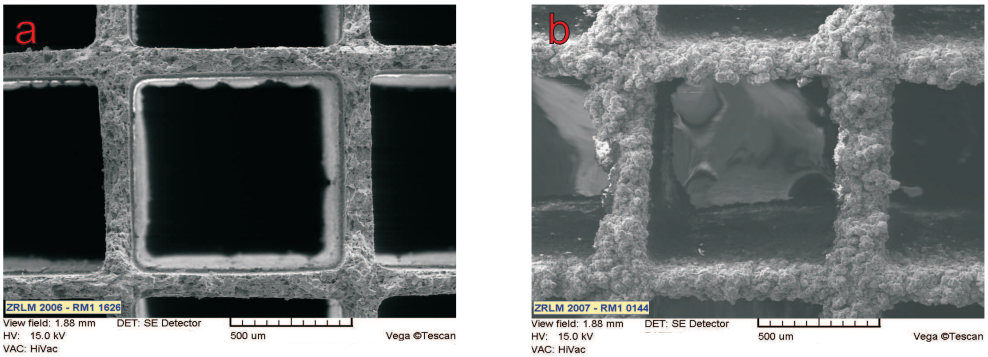

Figure 4.4.: SEM images of cordierite honeycomb samples, a shows the untreated sample, b shows the sample after the synthesis of $Cu_3(BTC)_2$.

on the surface was still scarce. It was therefore decided to move over to another solution. The extrusion of $Cu_3(BTC)_2$ with methylcellulose and mineral binding agent was chosen to produce $Cu_3(BTC)_2$ monolithic structures.

Specific surface area and XRD pattern

To confirm the formation of $Cu_3(BTC)_2$, all samples were finely grinded and analyzed by XRD, some of the results are shown in figure 4.5. The calculated XRD patterns of $Cu_3(BTC)_2$ as well as a reference pattern of cordierite are included in the diagram. The patterns of samples **a**, **b** and **c** show no peaks of $Cu_3(BTC)_2$, only the cordierite peaks are present. The XRD experiment could thus not confirm the formation of $Cu_3(BTC)_2$. Still, the formation of some $Cu_3(BTC)_2$ material on the samples could be verified by gas sorption experiments. The single point BET surface areas of almost all the samples averaged to about $50\,m^2g^{-1}$, see table 4.2, whereas the original sample showed no inner

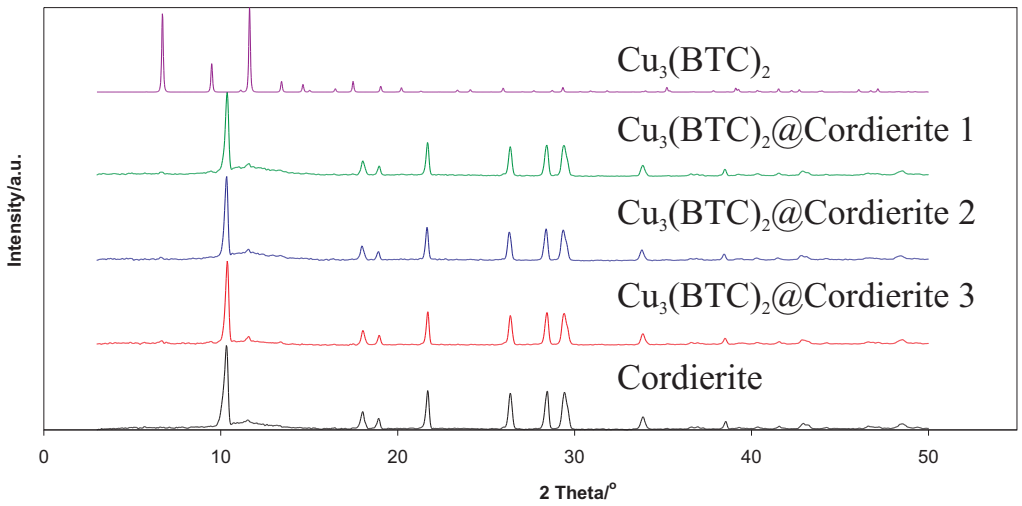

Figure 4.5.: XRD patterns of different $Cu_3(BTC)_2$@ceramic samples.

surface area. To estimate the content of deposited crystals, the samples were weighed before and after the synthesis. Since in most of the cases the reaction mixture was stirred during synthesis, it was difficult to obtain reasonable results. The inner channels of the monoliths are relatively fragile and the risk of breaking small pieces was high. The differences in weight are shown in table 4.2. If one assumes $Cu_3(BTC)_2$ to have a specific inner surface area of about $1300\,m^2g^{-1}$, which is a typical value for both synthetic routes, $50\,m^2g^{-1}$ should account for approximately 33 mg of $Cu_3(BTC)_2$ per gram cordierite. None of the weight differences of the sample showed these values, they were always lower.

Scanning electron microscopy (SEM)

A photograph of one sample is shown in figure 4.3, showing a clear blue color of the honeycomb indicating a formation of $Cu_3(BTC)_2$. Figure 4.4 shows SEM images of the cordierite honeycomb before and after the synthesis of $Cu_3(BTC)_2$. It can clearly be seen that there is a deposition of crystals on the cutting edge of the honeycomb, whereas no crystals are in the inner channel walls. The crystals show the typical octahedral shape of $Cu_3(BTC)_2$. As only small amounts of material were deposited on the cutting edges of the honeycombs, it is assumed that the amount of material was simply too low to generate $Cu_3(BTC)_2$ peaks in the XRD pattern.

Sample description	S_a [m^2g^{-1}]	Δ_m[mg]
Untreated, synthesis 1	44	4.1
Untreated, synthesis 2	58	4.2
Etched (2.5 M), synthesis 1	55	-140.1
Etched (2.5 M), synthesis 2	41	0.2
Etched (5 M), synthesis 1	48	26.5
Etched (5 M), synthesis 2	46	3.6
Etched (10 M), synthesis 1	52	12.2
Etched (10 M), synthesis 2	40	10.5

Table 4.2.: Specific surface area (S_a) (Single point BET surface area calculated at $p/p_0 = 0.3$) and increase/decrease in weight (Δ_m) of $Cu_3(BTC)_2$@ceramic samples.

Conclusion

Although the specific surface area of the samples was slightly higher than for the untreated cordierite, no peaks of $Cu_3(BTC)_2$ could be obtained in the XRD pattern. The SEM images revealed that the deposition takes place only on the cutting edges of the monolith, where the surface is relatively rough. None of the attempts to improve the synthesis by pretreating the cordierite led to satisfying results. Etching the cordierite had almost no impact on the degree of deposition. Degreasing the samples with diethyl ether led to even lower surface areas and was therefore not listed in table 4.2. In all cases, the deposition of $Cu_3(BTC)_2$ on the ceramic surface was scarce. The specific surface area for all samples was not higher than $50\,m^2g^{-1}$. It was therefore decided to move over to another solution. The extrusion of $Cu_3(BTC)_2$ with methylcellulose and mineral binding agent was chosen to produce $Cu_3(BTC)_2$ monolithic structures.

4.2. $Cu_3(BTC)_2$ monoliths

State of the art

There are two techniques known from industrial applications to produce monolithic structures made of zeolitic materials. The first technique makes use of the ceramic structures, which were also used in the foregoing section. The porous material is mixed with a binding agent and coated on the monolith, so-called washcoating. In the second technique, the material is applied onto long bands of paper or fabric. These are then wound to monolith like structures [80]. Both techniques are relatively complex technologies compared to the extrusion. Moreover, they reduce the solid fraction of the active material extensively. Regarding the shaping of $Cu_3(BTC)_2$, there are no technologies known that describe the shaping of $Cu_3(BTC)_2$ to monoliths. The only noteworthy products available on the market are pellets made of $Cu_3(BTC)_2$ in a cylindrical shape from the *BASF group*.

The manufacturing of monoliths made of porous materials comprises both advantages and disadvantages depending on the interests of the observer. Compared to the $Cu_3(BTC)_2$@ceramic approach, this process and the already known ones require a binding agent in order to provide a certain mechanical stability of the monolith structure. The use of additives decreases the solid fraction of the monolith and therewith its performance by reducing the accessible inner surface area. In spite of this aspect, the use of powders is impossible and a certain treatment of the material is indispensable, as already mentioned before. However, the use of additives can also be of great advantage, for example by introducing materials prior to extrusion, which can later be removed by calcination. The resulting secondary porous structure is beneficial for mass transport. Compared to beads, the monolith structures benefit from a more advantageous pressure drop. Beads are also causing problems in packed beds because of abrasion, which is not the case for monolithic structures [81]. In the following, the manufacturing and characterization of $Cu_3(BTC)_2$ monoliths is described.

4.2.1. Manufacturing of $Cu_3(BTC)_2$ monoliths

Experimental

The fabrication of $Cu_3(BTC)_2$ monoliths was based on the work of C. Trefzger [82], who examined the processing technology for the manufacturing of monolithic structures based on zeolitic powders. Among others, the focus of his thesis was the investigation of different additives that were used for the forming step, among them polysiloxanes,

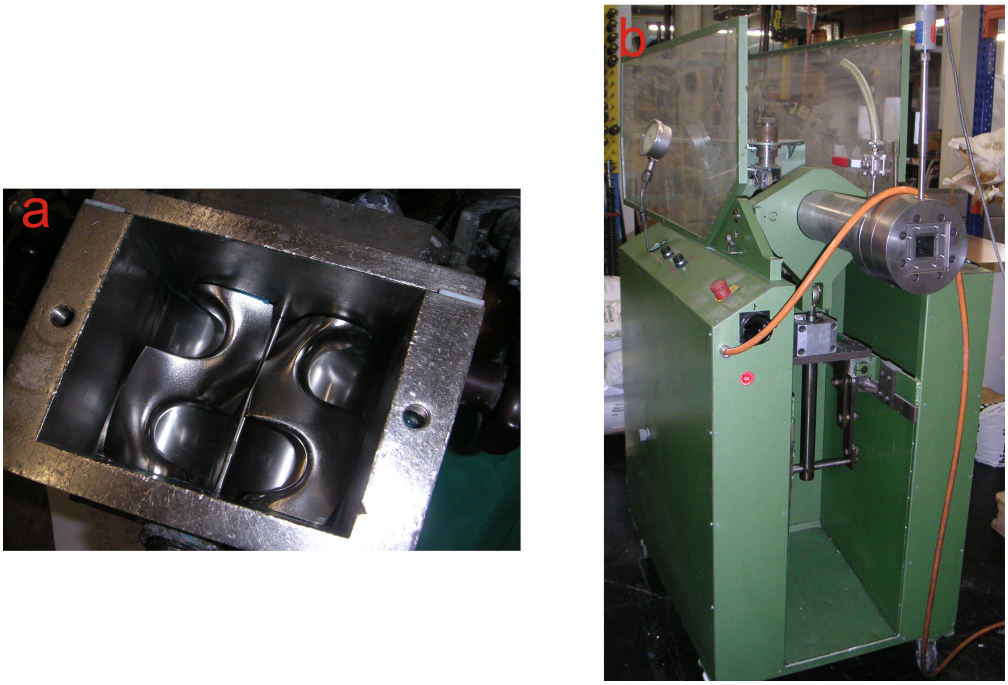

Figure 4.6.: Picture a shows the lab-scale kneader, picture b the ram extruder.

silicic acid esters, silica gel and pyrogenic silicic acid. In this work, Silres MSE 100 ($CH_3Si(O)_{1.1}(OCH_3)_{0.8}$ Wacker-Chemie GmbH) was used as binding agent. Culminal MHPC 20000 P (Methylcellulose, Hercules-Aqualon) was used as plasticization additive. The fabrication of $Cu_3(BTC)_2$ monoliths was a two-step process. First, $Cu_3(BTC)_2$ was mixed with binding agent and plasticization additive in a lab-scale kneader until the molding batch was of homogeneous appearance. The second step was the extrusion of the molding batch to a monolith in a ram extruder. The monolith was cut into 200 mm long pieces, which were treated by microwave drying for twenty minutes. The monoliths were finally dried at ambient pressure at 120 °C for several hours. Both the equipment and a picture of the kneading and the extrusion is shown in figures 4.6 and 4.7.

Several molding batches with differing ratios of Culminal MHPC 20000 P, Silres MSE 100, water and $Cu_3(BTC)_2$ had been prepared and extruded in the ram extruder yielding different results. The final composition, batch number two in table 4.3, was used for extrusion for all samples. All other compositions were either too soft or sticky for the forming process or the monolith deformed after having passed the extrusion tool.

The same monoliths were fabricated using zeolite 4A powder based on the recipes derived by Trefzger [82]. A picture of the $Cu_3(BTC)_2$ monolith is shown in figure 4.8.

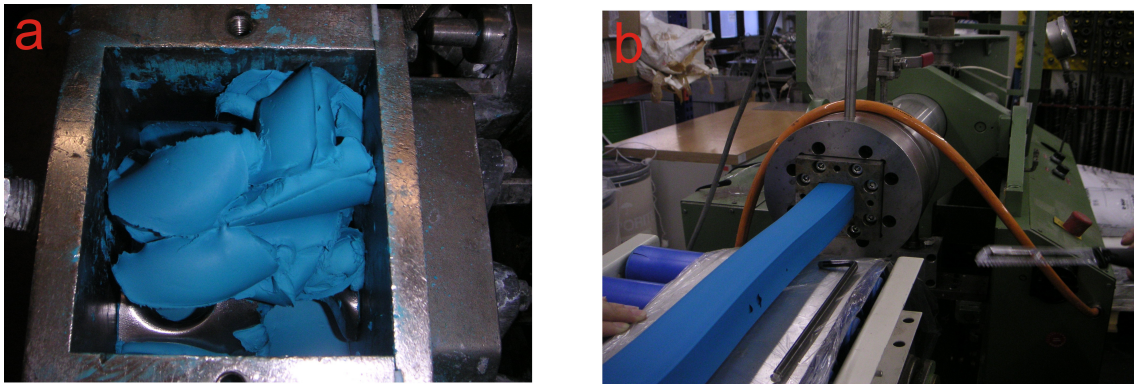

Figure 4.7.: Picture a shows the ram extruder during the extrusion process, picture b shows the kneading of the $Cu_3(BTC)_2$ molding batch.

	Water [g]	Culminal MHPC 20000 P [g]	Silres MSE 100 [g]	$Cu_3(BTC)_2$ [g]	Result
Batch 1	80	25	50	180	too sticky
Batch 2	80	20	25	180	best result
Batch 3	70	15	20	180	too soft
Batch 4	50	12	12	180	deformation after extrusion
Batch 5	40	12	12	180	too soft

Table 4.3.: Different composition and description of the fabricated molding batches for the $Cu_3(BTC)_2$ monoliths.

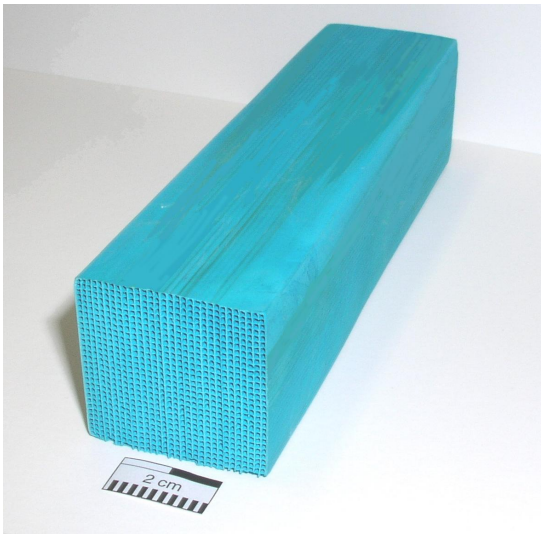

Figure 4.8.: Picture of $Cu_3(BTC)_2$ monolith.

The molding batch

As already discussed, the formation of monolith like structures requires the use of a binding agent to provide the mechanical stability of the monolithic structures. The binder should not hinder the mass transport between the $Cu_3(BTC)_2$ particles and the adsorbate. Binding agents that are small enough to penetrate the $Cu_3(BTC)_2$ pores are also not suitable. Liquid substances are advantageous, as they are easily distributable with the active material during the kneading process. Since powders like zeolite A and $Cu_3(BTC)_2$ are not plastic when mixed with water, the use of an additive is needed. The main task of a plasticization additive is to transform the powder suspensions to a molding batch with suitable flow characteristics. Several molding batches with differing ratios of methyl cellulose, methyl siloxane ether, water and $Cu_3(BTC)_2$ had been prepared and extruded in the ram extruder yielding different results. The final composition, batch number two in table 4.3, was used for extrusion of all samples. Obviously, a minimum amount of plasticization additive is needed to provide appropriate flow characteristics. As the additive is a liquid, the amount must not be too high either, since this led to a rather sticky molding batch like number one. The composition of molding batch two contained less plasticizer, which automatically produced a drier batch, which still had a sufficient flow characteristic. The other compositions three to five were too soft for extrusion or the monolith deformed after having passed the extrusion tool.

Methyl siloxane ether as binding agent

The use of binders is known from the already approved techniques that were discussed above. The thesis of *Hammond* [83] recommends the use of hydrolyzates based on silicic acid esters. According to Hammond, the hydrolyzation of tetra methyl orthosilicate yields the best results. However, generating these solutions is difficult, as the hydrolyzate has to have a pH less than 7 during the forming process in order to avoid the precipitation of silicic acid. Others propose the use of clays like attapulgite, kaolin, bentonite or montmorillonite [84]. The last two of these clays exhibit an irreversible phase changes at temperatures above 700 °C. Thus, the bonded product is not fired off because most hydrophilic zeolitic structures loose the structural stability at this temperature. The patents of *Wusirika* [85] propose the use of silicone resins as permanent binder. However, the calcination temperature is advised to be at least 400 °C. The binding agents investigated by Trefzger is most suitable as they decompose at about 200 °C, so in the range of the thermal stability of $Cu_3(BTC)_2$ that decomposes at about 280 °C. He examined silicone resins as suitable binding agents. The commercial application of silicone resins are as binder in heat resistant paint. Their temperature resistance ranges from 200-650 °C, which is also in the temperature range of zeolitic materials. Silicone resins are partly cross-linked polysiloxanes, whereas some silicon atoms possess functional groups like silanol- and alkoxy groups. The degree of functionalization governs the reactivity of the silicone. In order to achieve complete cross-linking, hydrolysis or condensation is induced at elevated temperatures. The mechanism of hydrolysis and cross-linking of the resin is shown in figure 4.9.

Silicone resins are suitable binding agents as they are available as liquids, due to the only partly crossed-linked properties. Thus, the blending with the molding batch is simple and after formation the shaped structures are heated to induce the cross-linking. Depending on the organic substituent of the silicone resin one distinguishes between methyl-, ethyl, phenyl- and vinyl siloxane ethers. The siloxane ether chosen for the $Cu_3(BTC)_2$ monoliths was a methyl siloxane ether, since it is the most temperature resistant one compared to other silicone resins. At 200 °C oxidation of the organic methyl group starts and at 400 °C all organic parts are pyrolytically decomposed and only a SiO_2 framework remains. The most suitable function for the methyl siloxane ether turned out to be of the methoxy type, its structure is shown in figure 4.9. The mechanism of condensation and concurrent binding to the surface of $Cu_3(BTC)_2$ is shown in figure 4.10. The structure of $Cu_3(BTC)_2$ consists of paddle-wheel subunits with two active copper sites in its center. They represent a hydrophilic site where water is reversibly coordinated. Thus the surface of $Cu_3(BTC)_2$ carries some already coordinated water

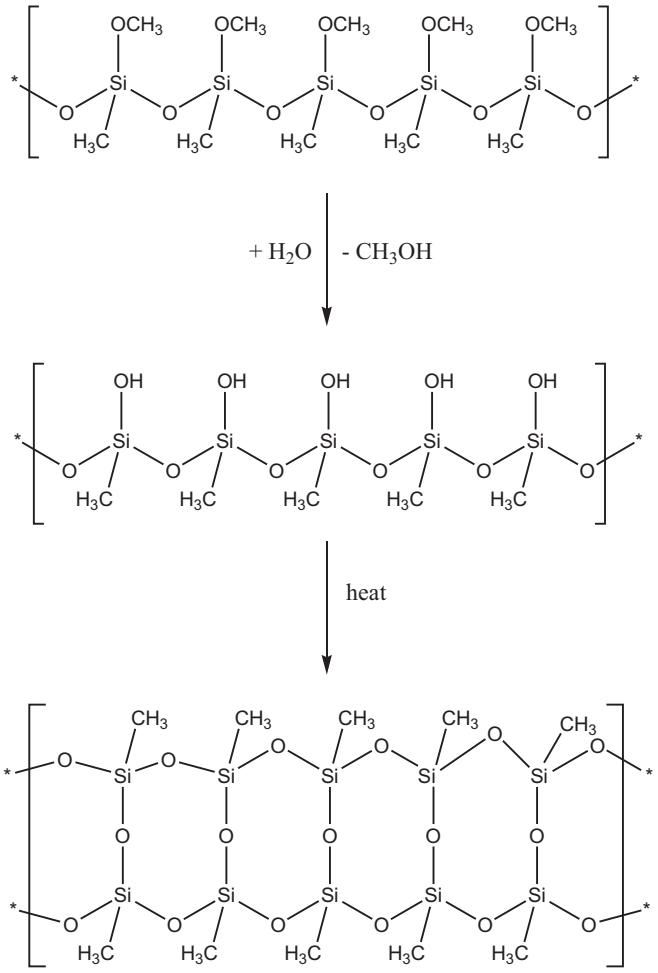

Figure 4.9.: Structure of methoxy methyl siloxane ether. The first reaction step shows its reaction with water, the second step shows the heat-induced cross-linking.

molecules to which the hydroxyl groups of the silicone resin can coordinate and yield the desired mechanical stability of the monolith. The same is valid for the zeolite surface which carries siloxyl groups. These groups also coordinate to the silicone resin.

Methyl cellulose as plasticization additive

As $Cu_3(BTC)_2$ particles like zeolite A show no plastic properties after immersing them in water, an appropriate plasticization additive has to be used. Methyl cellulose is an appropriate plasticization additive, as it is soluble in water and can therewith easily be blended with the powder and the binding agent. It is non-toxic and commercially available because of its extensive use in food processing industry as thickening agent and plastic flow additive [86]. Cellulose is almost completely insoluble in water due to

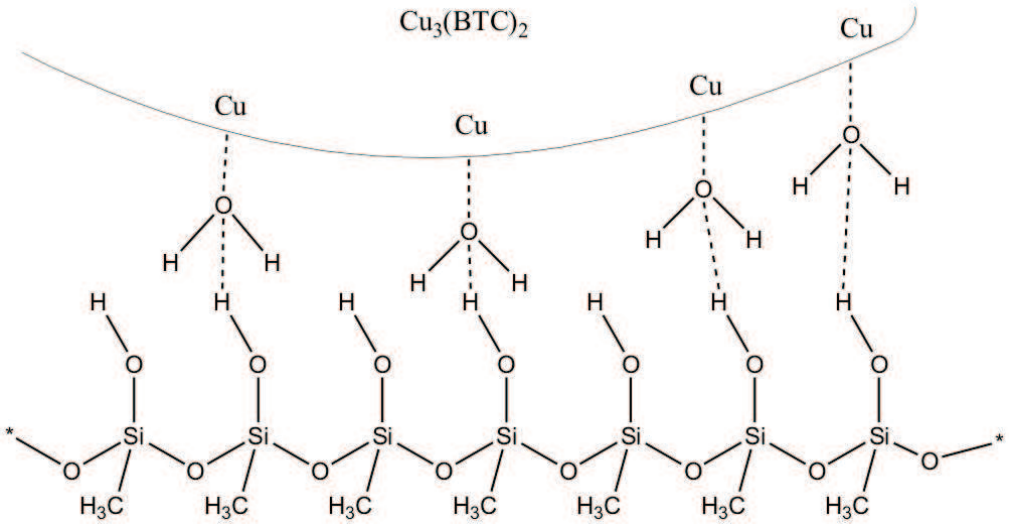

Figure 4.10.: Proposed binding mechanism of $Cu_3(BTC)_2$ and poly siloxane ether.

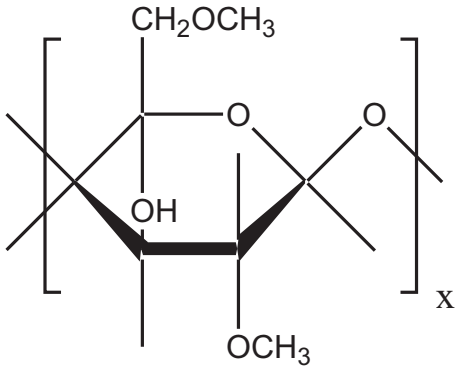

Figure 4.11.: Structure of methyl cellulose.

the hydrogen bridging between the polymeric chains. In the methoxy functionalized cellulose, hydroxyl groups are exchanged with methoxy functions, see figure 4.11. These reduce the amount of hydrogen bridges and therewith enhance the solubility in water. The higher the degree of methoxy functionalization, the better the water solubility. Thus, the viscosity of the water methyl cellulose solution is easily controllable by choosing the appropriate type of methyl cellulose. The plastic behavior of methyl cellulose is based on the interaction of the hydrated layers that are found on the surface of zeolite particles [82]. The same should be valid for the $Cu_3(BTC)_2$ particles that are also highly hydrophilic due to the copper coordination sites. The water solubility of methyl cellulose and the resulting interaction with the water layers supports the plasticizing properties of methyl cellulose [87].

The function of the plasticizer is no longer necessary after the forming step. Plasticization additives that are of organic nature are therefore of special interest, as they can be burned off afterwards. Furthermore, the burn off leads to the formation of a secondary pore structure, which promotes a good mass transfer. Methyl cellulose starts to decompose at 200 °C. This was one reason to choose methyl cellulose as plasticizing agent for zeolite A molding batches, as it easily tolerates temperatures higher than 200 °C. $Cu_3(BTC)_2$ decomposes at lower temperatures and a complete removal is in this case not possible. As a burn-off is not obligated, methyl cellulose is still a suitable additive for the manufacturing of $Cu_3(BTC)_2$ monoliths.

4.2.2. Characterization of $Cu_3(BTC)_2$ monoliths

This section will summarize the basic characterization of the $Cu_3(BTC)_2$ monoliths. The detailed characterization regarding water adsorption and stability will be discussed in chapter 5 and 5.3. The zeolite A monolith will not be discussed in this chapter, as they were already investigated by Trefzger.

Thermal gravimetric analysis, EDX and SEM

The SEM images of the sample (figure 4.12) show an overview as well as two detailed scans of the surface of the monolith. Image b shows a homogenous surface with regularly distributed crystals in the silicone resin matrix. The detail in image c shows clearly sharp edged crystals bound in a matrix. The typical octahedral shape of $Cu_3(BTC)_2$ crystals is not recognizable, but an EDX analysis that was performed on one of the crystals and the surrounding matrix indicated a much higher content of copper in the crystal like structures (see figure 4.13). Vice versa, the matrix showed higher silica content in the EDX experiment.

The thermal gravimetric analysis diagram in figure 4.14 shows the curve for $Cu_3(BTC)_2$ powder and the $Cu_3(BTC)_2$ monolith sample. The data are mostly similar to each other showing two distinct weight losses. After desorption of water in the temperature range from 40-150 °C, the curve levels off in a plateau up to 320 °C when $Cu_3(BTC)_2$ starts to decompose. The only difference here is the distinct plateau of the powdered sample, which reveals the stability of $Cu_3(BTC)_2$ up to 320 °C. The monolithic curve already shows a slight decrease before at approximately 260 °C, which can be assigned to the decomposition of the additives. In summary, the thermal stability of the monolith is comparable to the powder.

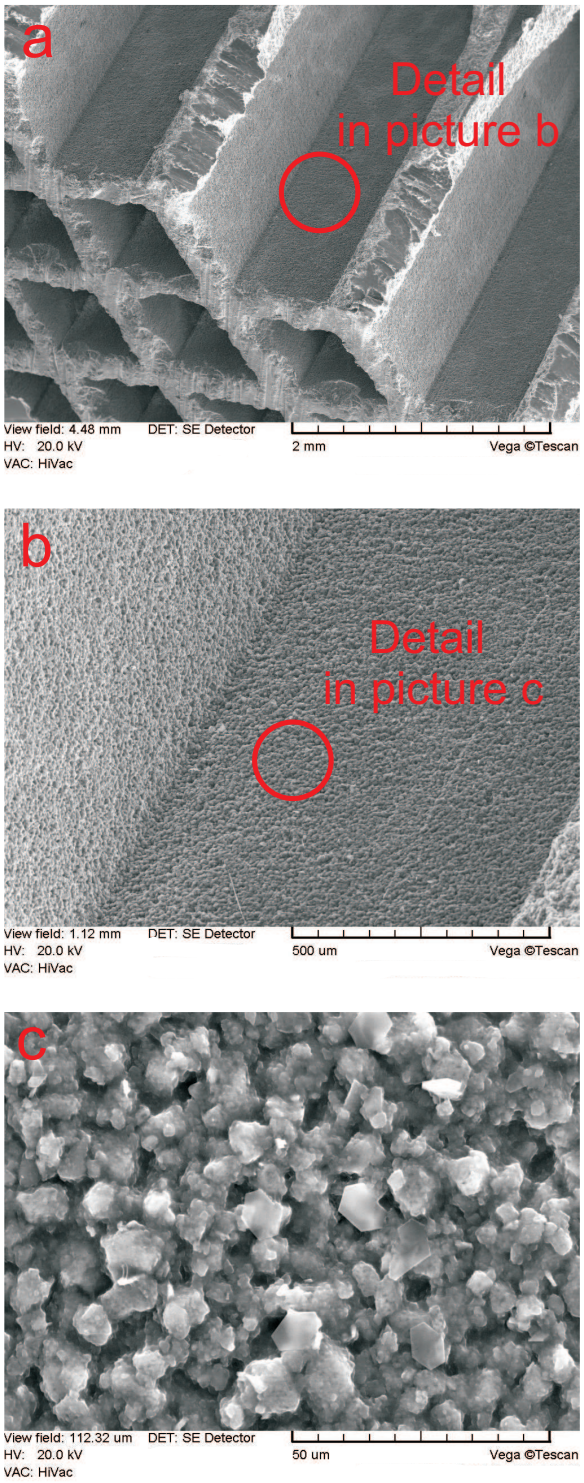

Figure 4.12.: SEM images of a $Cu_3(BTC)_2$ monolithic sample, picture a shows an overview of the monolith, b and c are more detailed views.

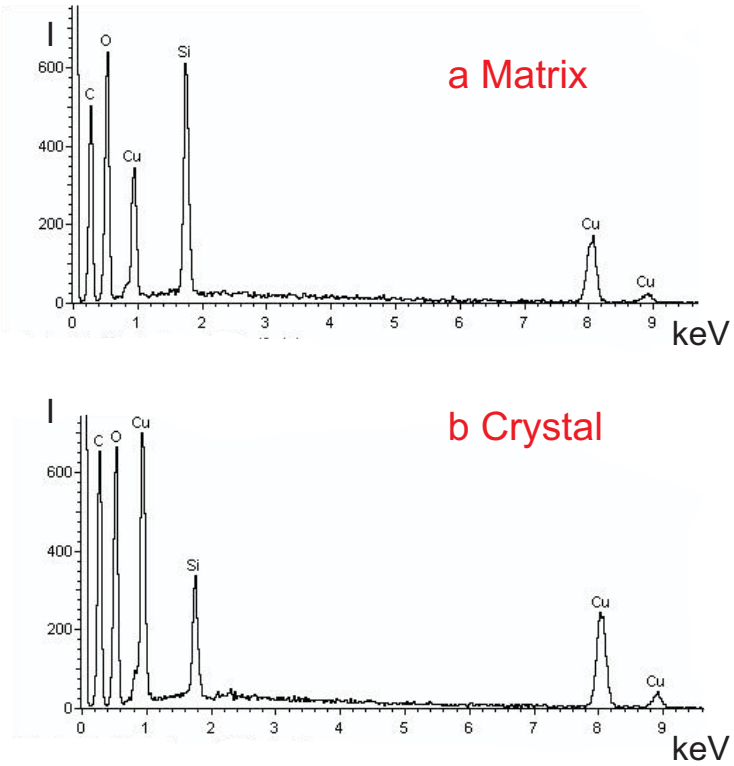

Figure 4.13.: EDX Analysis of matrix (a) and crystal (b) of the $Cu_3(BTC)_2$ monolith.

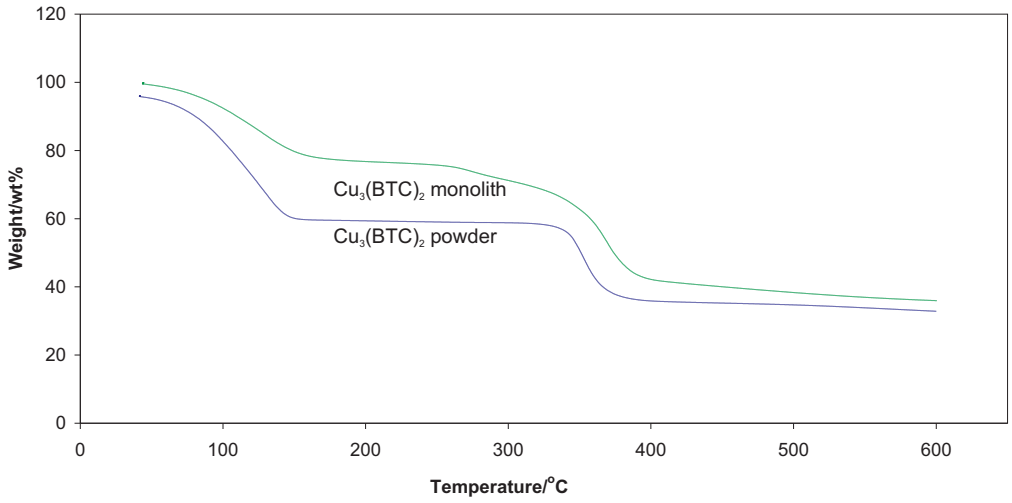

Figure 4.14.: Thermal gravimetric analysis of $Cu_3(BTC)_2$ powder and $Cu_3(BTC)_2$ monolithic samples.

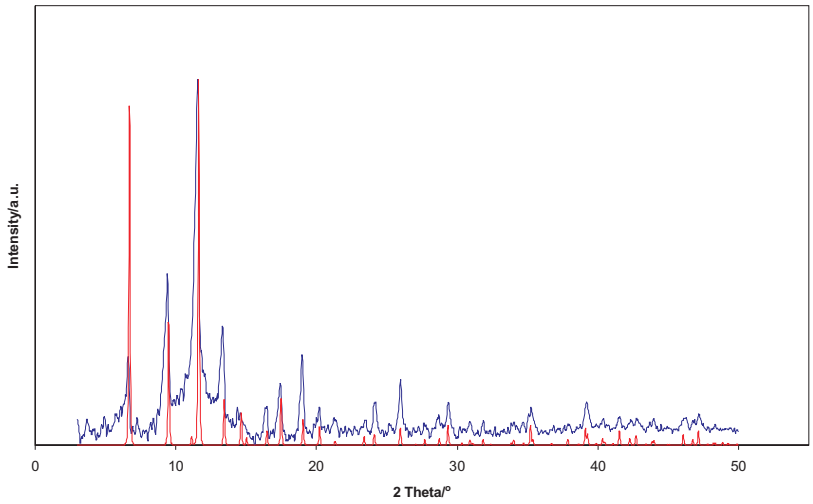

Figure 4.15.: X-ray powder diffraction pattern of a $Cu_3(BTC)_2$ monolithic sample in blue and the calculated pattern of $Cu_3(BTC)_2$ in red.

Mechanical stability

In order to evaluate the mechanical stability of the monoliths, the crushing strength of the samples was determined using a Zwick material testing equipment yielding excellent results. Both the as-made samples and activated samples (150 °C) were tested. The as-made samples showed a lower stability with averaged 281 N. Activated samples were slightly harder with 320 N. Tests with the commercial codierite honeycomb yielded a crushing strength of 104 N.

Specific surface area and XRD pattern

The XRD pattern clearly confirms the existence of $Cu_3(BTC)_2$ in the monoliths, see figure 4.15. Several BET surface measurements have been performed to investigate the specific surface area. In a first experiment, the specific surface area amounted to $484\,m^2g^{-1}$, which is an excellent result. The commercial pelleted product of the *BASF* company shows approximately the same value with $486\,m^2g^{-1}$. Unfortunately, the value of the $Cu_3(BTC)_2$ monolithic samples decreased after a certain time to $287\,m^2g^{-1}$, see table 4.4. As it turned out, the outgassing temperature was here of great importance. For the first measurements, which were performed immediately after manufacturing, 150 °C was chosen. Later, the value decreased to $189\,m^2g^{-1}$ even though the same activation temperature was used. Lower activation temperatures showed a better result for the second series of measurements. Enhanced temperatures resulted in decreased

Activation Temperature [^{0}C]	S_a [m^2g^{-1}]
150	484
100	340
120	370
150	189
170	215

Table 4.4.: Specific surface areas (S_a) of $Cu_3(BTC)_2$ monolithic samples (Single point BET surface area calculated at p/p_0= 0.3 from nitrogen physisorption at 77 K).

specific surface areas. Since the plasticization additive is only needed during the extrusion process, it can be removed or burned off after the forming and drying process. As mentioned before, the methyl cellulose starts to decompose at 200 °C, which was confirmed in the thermal gravimetric analysis (see figure 4.14). An activation temperature above this should therewith be advantageous, as the resulting burn off yields a secondary porous structure that promotes a fast mass transfer. Despite this, experiments showed that at elevated activation temperatures the values for the inner surface area decreased, see table 4.4.

Since the molding batch contains water, it was assumed that a certain degradation of $Cu_3(BTC)_2$ is induced, which automatically leads to decreased surface areas. A detailed discussion of the water stability of $Cu_3(BTC)_2$ will be given in chapter 5.

Conclusion

In conclusion, the fabrication of $Cu_3(BTC)_2$ monoliths was successful and yielded satisfying samples with high mechanical stability with a crushing strength of 320 N. Additionally, the samples show a inner surface area of 370 m^2g^{-1}. The product is comparable to available commercial products in terms of inner surface areas. The most suitable temperature for outgassing is 120 °C, at which no removal of the plasticizing agent occurs. The fabrication or rather the molding batch composition can be reconsidered in order to obtain samples with even better properties.

4.3. $Cu_3(BTC)_2$ paper sheets

Filtration industry benefits from a well-known and inexpensive technology. Filter paper is a relatively cheap material used to separate coarse and fine particles from either liquid or gaseous streams. The filtration efficiency is mostly attained by choosing the right type of fibers for the needed application. The incorporation of powders into the papers is also a known method. One example is the use of fillers, which give the paper certain stability. The possibility to incorporate powders into paper sheets is of great advantage as these forms are exceptionally flexible. Paper manufacturing is also well-known and cheap technology and thus a good solution to immobilize expensive materials for specific applications.

4.3.1. Preparation and characterization of $Cu_3(BTC)_2$ paper sheets

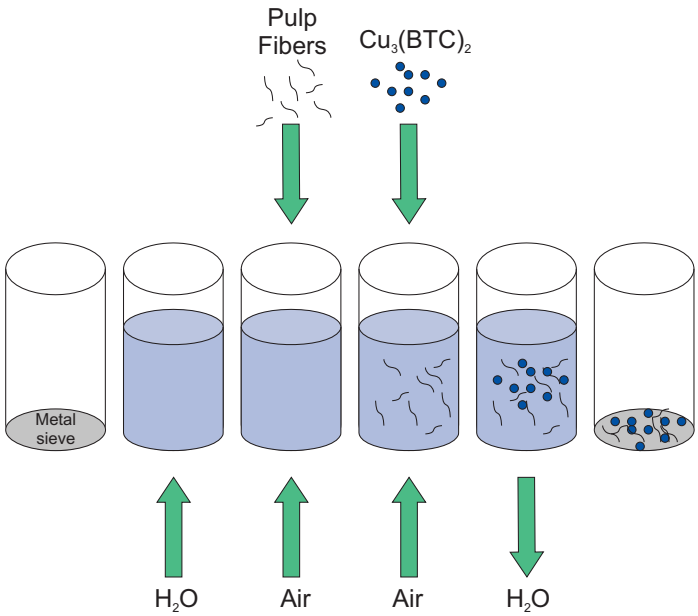

Figure 4.16.: Schematic description of the paper formation in a *Rapid-Köthen Sheet Mold*.

Experimental

$Cu_3(BTC)_2$ paper sheets were prepared using a *Rapid-Köthen* Sheet Mold [88]. This apparatus is mostly used in paper industry to analyze the effects of pulp modifications. Small amounts of paper can be produced and characterized before introducing a certain pulp mixture in an industrial-scale production.

In the *Rapid-Köthen* Sheet Mold, which is schematically shown in figure 4.16, approximately 7 liters of water are pumped into a 10 liters cylinder through a metal sieve that is located at the cylinder bottom. A pulp-water slurry is added and the mixture is agitated vigorously by purging the water with air through the metal sieve. A $Cu_3(BTC)_2$-water slurry is given to the mixture and the water is sucked off through the sieve. The pulp fibers and the powder form a paper sheet on the metal sieve. The cylinder is removed from the sieve and the $Cu_3(BTC)_2$ paper sheet is knocked off. The paper is placed between two thick cardboard sheets and the water is squeezed out by wheeling a rubber castor over it. Finally, the paper sheet is dried at 120 °C for 10 minutes.

For one paper sheet, 4 g of pulp fibers (Rayonnier pulp, Hamacell pulp and CTMP, 1:1:1) and 2 g of $Cu_3(BTC)_2$ powder were used.

Thermal gravimetric analysis and SEM

The paper sheets were analyzed regarding their content of incorporated $Cu_3(BTC)_2$ powder and the resulting specific surface areas. A visual investigation was performed by scanning electron microscopy. The paper sheets turned out to possess an inhomogeneous

Sample	m_{CuO} [wt%]	$m_{Cu_3(BTC)_2}$ [wt%]
1	12.7	14.6
2	11.9	13.6
3	10.4	11.9
4	9.4	10.8
5	9.2	10.3
6	5.8	6.4

Table 4.5.: Content of $Cu_3(BTC)_2$ in various $Cu_3(BTC)_2$ paper sheets, determined from thermal gravimetric analysis.

distribution of powder. Various samples were taken from one sheet and analyzed by thermal gravimetric analysis (TGA). The amount of $Cu_3(BTC)_2$ was determined by recalculating the residual CuO at 600 °C of the TGA diagrams yielding results from 6.5 to 14.6 wt% as shown in table 4.5. The scanning electron micrography (SEM) images in figure 4.17 confirm the mentioned inhomogeneity. The crystals are only loosely bound between the fiber bundles.

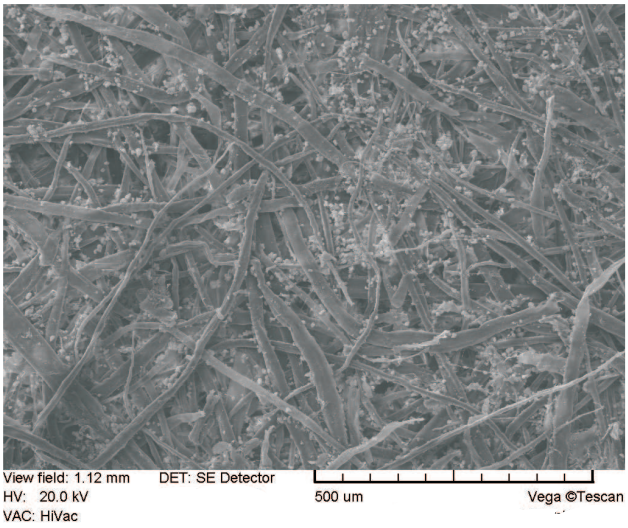

Figure 4.17.: SEM image of a $Cu_3(BTC)_2$ paper sheet, top view.

Specific surface area and XRD pattern

Single point BET-surface area in average was around $170\,m^2g^{-1}$, see figure 4.18. The relative low surface area cannot only be attributed to a low content of powder, but also to the eventual degradation of the framework. During the *Rapid-Köthen* process, the powder was immersed in water. As it turned out later, the material is not completely stable when it is in direct contact with water.

First, the specific surface area decreases followed by an irreversible change of the crystal structure [89]. The water stability will be discussed in detail in chapter 5. However, the XRD pattern in figure 4.19 confirms the presence of $Cu_3(BTC)_2$ in the paper sheets.

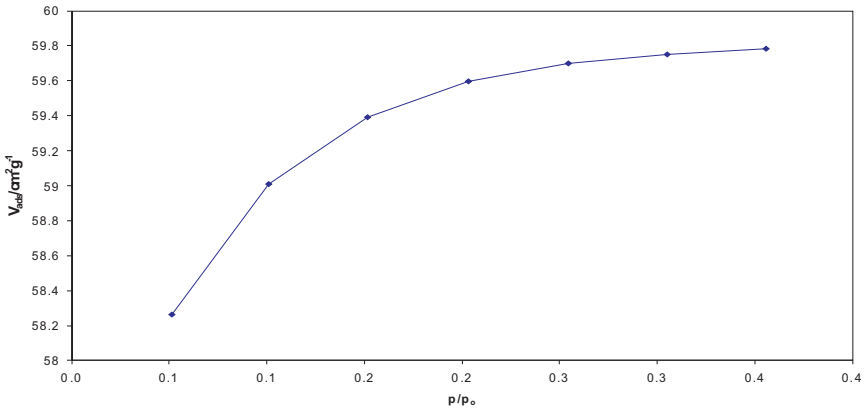

Figure 4.18.: Nitrogen adsorption isotherm of the $Cu_3(BTC)_2$ paper sheet recorded at 77 K.

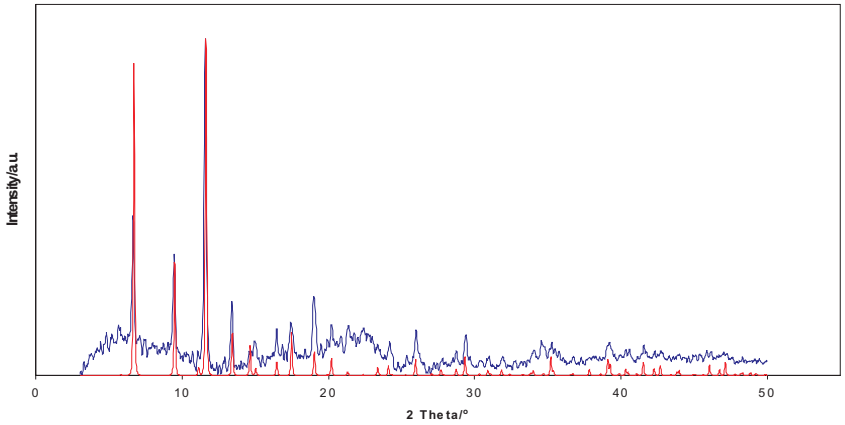

Figure 4.19.: X-ray powder diffraction pattern of the $Cu_3(BTC)_2$ paper sheet in blue and the calculated pattern of $Cu_3(BTC)_2$ in red.

Conclusion

In summary, $Cu_3(BTC)_2$ paper sheets were fabricated in a *Rapid Köthen* Sheet Mold. The resulting papers showed an inhomogeneous powder content ranging from 6.5-14.6 wt%. The specific surface area of the papers was in average $170\,m^2g^{-1}$. SEM images showed that the crystals were only loosely bound between the cellulose fibers. As the incorporation of powder in paper sheets cannot really be regarded as an ideal solution to immobilize $Cu_3(BTC)_2$ powder, another approach had to be considered. The in-situ synthesis of $Cu_3(BTC)_2$ on pulp fibers was chosen, which will be discussed in the following section.

4.4. $Cu_3(BTC)_2$@pulp

As discussed in chapter 4.3, an in-situ approach to deposit $Cu_3(BTC)_2$ crystals on pulp fibers has advantages compared to the $Cu_3(BTC)_2$ paper sheets [90]. The concept of depositing porous materials has previously been investigated by *Mintova* and *Valtchev* [91, 92], who deposited zeolite NaA on vegetal fibers.

4.4.1. Preparation and characterization of $Cu_3(BTC)_2$@pulp

Experimental

Benzene-1,3,5-tricarboxylic acid (1.68 g, 8 mmol) was dissolved in 100 ml of ethanol, dimethyl formamide (1:1 v/v) and mixed with an aqueous solution (50 ml) of copper(II) nitrate hemipentahydrate (1.86 g, 8 mmol). After addition of 1 g of pulp fibers, the solution was stirred for 15 minutes. The slurry was gradually heated to 358 K in a 400 ml Teflon-lined steel vessel and kept at this temperature for 24 hours. The resulting product was filtered and washed several times with $EtOH/H_2O$ until the filtrate turned clear. The blue fibers were briefly dried in air and finally activated at 433 K for 18 hours.

Wood pulp

Pulp is fibrous material prepared by chemical or mechanical separation of fibers from wood or fiber crops. The fibrous material can easily be dispersed in water and reformed to a web or paper [93]. In this study, three different types of wood pulp samples were used:

- CTMP (Chemithermomechanical pulp)
- bleached kraft pulp (Chemical pulp)
- unbleached kraft pulp (Chemical pulp)

There are different categories of wood pulping processes, among them chemical, semi-chemical, chemimechanical and mechanical pulping [93]. These are in order of increasing mechanical energy required to separate the fibers. Chemical methods make use of chemicals to separate fibers, whereas mechanical methods only use physical energy. The resulting pulps from these processes have different properties. Chemical pulps like the ones obtained from kraft pulping processes have a much better strength than chemimechanical pulps. As the use of chemicals leads to more efficient degradation of wood components

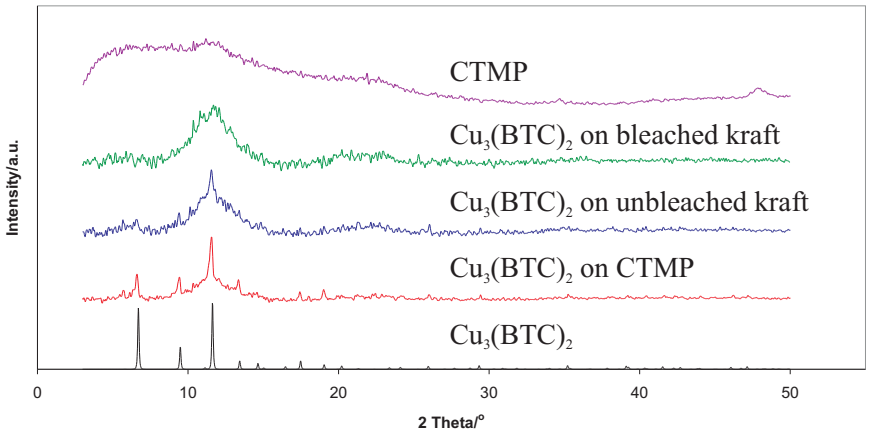

Figure 4.20.: XRD patterns of the different $Cu_3(BTC)_2$@pulp samples.

like lignin and hemicellulose, the yield of chemical pulping processes is much lower. On the other hand, chemical pulping yields fibers, which are uncut compared to mechanical pulping. The applications for the different pulps are also different, the chemical pulp is mainly used for bags and wrapping while mechanical pulps are employed in newsprint and magazines.

XRD pattern

The first step to characterize all samples was to confirm the formation of $Cu_3(BTC)_2$ on the pulp samples. Since cellulose fibers themselves are semi crystalline, the XRD patterns showed only the peaks of $Cu_3(BTC)_2$, see fig 4.20. With increasing degree of coverage those are more pronounced hinting at a higher content of $Cu_3(BTC)_2$ as well as an enhanced specific surface area, which will be discussed later.

Thermal gravimetric analysis and specific surface areas

Thermal gravimetric analysis was used to determine the content of $Cu_3(BTC)_2$ deposited on the pulp fibers. Table 4.6 shows the direct correlation of specific surface area and content of $Cu_3(BTC)_2$. Surprisingly, the outcome of both values is different for the different pulp qualities. At the first sight, one reason for the differences might be the chemical composition of the pulp fibers. In order to investigate this further, the pulp samples were analyzed regarding their residual lignin content.

Pulp sample	$C_{Cu_3(BTC)_2}$ [wt%]	κ	S_a [m^2g^{-1}]
Bleached kraft	0	0.3	10
Unbleached kraft	10.69	27.6	165
CTMP	19.95	114.5	314

Table 4.6.: Content of $Cu_3(BTC)_2$ (C - calculated from thermal gravimetric analysis diagrams), κ – numbers (κ – determined according to ISO 302) and specific surface area (S_a - Single point BET surface area calculated at p/p_0= 0.3 from nitrogen physisorption at 77 K).

Lignin residue and kappa number

Wood or crop material consists of cellulose, hemicellulose and lignin. During the pulping process, lignin and hemicellulose are removed from the wood material to obtain cellulose that is employed in paper industry. There are various pulping processes, among them the already mentioned kraft process and chemithermomechanical pulping. The kappa number (k-number) is an indirect indication of the residual lignin content of a pulp sample. It is measured indirectly by determining the consumption of a sulfuric permanganate solution [94]. Chemithermomechanically treated pulps are usually less delignified than those produced by purely chemical processes like the kraft or sulfite process. The goal of this process is here not to remove lignin completely, but to provide easily processable fibers. Kraft pulp is of a much lower lignin residue and it is therefore used in high quality applications, which require high strength of the fibers. As kraft pulps are darker than other wood pulps they can be bleached further to yield white and non-yellowing pulps. Bleached pulps contain even less lignin than the unbleached ones.

The k-numbers of the used pulp samples are listed in table 4.6. They correspond like the content of $Cu_3(BTC)_2$ with the measured specific surface areas of the samples.

SEM

The recorded SEM images confirmed the values given in table 4.6. The SEM images of the $Cu_3(BTC)_2$@CTMP samples show a regular distribution of the crystals along the fiber surface, see figure 4.21.

The explanation for the different outcome of the experiments is the differing amount of lignin residue of the pulp samples. Lignin is a high molecular weight structure mainly consisting of phenyl propane units linked with several radicals [95]. The structure of lignin is not fully understood yet, but the occurrence of functional groups like carbonyl or carboxylic groups is well known [96]. As the copper clusters in $Cu_3(BTC)_2$ are also

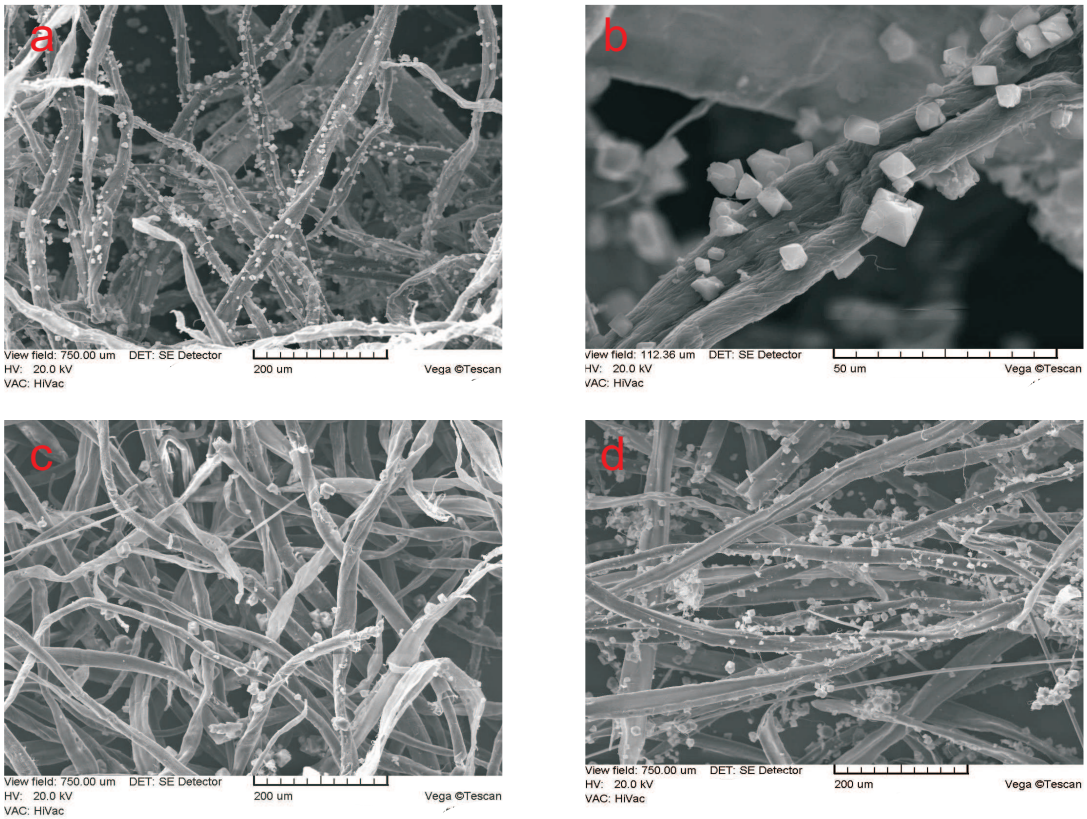

Figure 4.21.: SEM images of different $Cu_3(BTC)_2$@pulp samples, pictures a and b show $Cu_3(BTC)_2$@CTMP, c shows $Cu_3(BTC)_2$@unbleached pulp and d shows $Cu_3(BTC)_2$@bleached pulp.

linked by carboxylic functions, the adhesion to pulp samples with higher lignin residue could be favored. Similar observations have been made by other groups investigating the deposition of MOFs on carboxylate terminated self-assembled monolayers (SAMs). In these studies, they deposited MOF-5, $[Zn_2(BDC)_2(DABCO)]$ (BDC = benzene-1,4-dicarboxylate) (DABCO = 1,4-diazabicyclo[2.2.2]octane) and $Cu_3(BTC)_2$ on bare silica and alumina surfaces as well as on functionalized SAM surfaces [76, 97, 98].

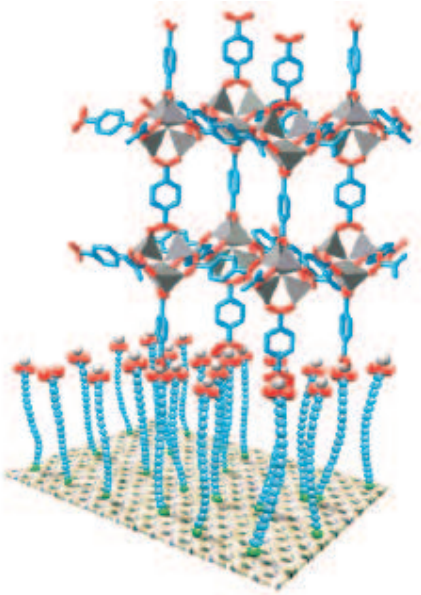

Figure 4.22.: The concept of anchoring a typical MOF-5 building unit to a carboxylic acid-terminated SAM [98].

The surfaces were terminated either with CF_3 or COOH functions. In all studies, the MOF selectively anchor to the carboxylate terminated areas of the SAM. The CF_3 terminated SAMs show no adhesion with the porous materials. The bare surfaces of SiO_2 and Al_2O_3 are not covered with crystals. The concept of linkage is shown in figure 4.22. A similar mechanism can be applied to the $Cu_3(BTC)_2$@pulp series. The higher the amount of lignin and therewith carboxylic functions, the better the adhesion of the $Cu_3(BTC)_2$ crystals to the fiber surface.

Conclusion

The deposition of the crystals on the surface was shown to be directly dependent on the lignin content of the pulp sample. The higher the lignin residue, the more $Cu_3(BTC)_2$ grows on the fiber surface. $Cu_3(BTC)_2$@CTMP showed best results with almost 20 wt% $Cu_3(BTC)_2$ and a specific surface area of $314\,m^2g^{-1}$. In contrast, there was almost no

crystal growth on bleached Kraft pulp with almost any lignin content. Compared to $Cu_3(BTC)_2$ paper sheets, the crystals are homogeneously distributed over the surface area, which ensures effective use of all material. In summary, a suitable carrier for a promising microporous material was identified. The substrate is inexpensive and pliable and it can be formed to papers that could be used in the filtration industry.

5. Water adsorption

In the following chapter, the materials described in chapter 2 are characterized by water adsorption isotherms. The aim was on the one hand to investigate the materials by their water adsorption behavior and on the other hand to select some materials that are possible candidates for both compressed air and diesel fuel drying. Regarding stability and capacity, the experiments include the investigation of the monolithic samples, discussed in section 4.2. Requirements for these applications are high water adsorption capacities, fast adsorption kinetics and adequate stability towards water.

5.1. Water adsorption isotherms

Water adsorption isotherms are not as common in the field of porous materials. Still, they are a useful extension to nitrogen physisorption experiments. In this work, the use of MOF materials as desiccant was one topic of investigation. The recording of water adsorption isotherms was thus indispensable [89] to receive information about hydrophilicity, total water adsorption capacity and water stability. Nitrogen physisorption isotherms are well known from literature, but water adsorption studies are still scarce [99–106]. For all materials, isotherms were recorded at 25 °C in order to characterize the MOF materials regarding their water adsorption behavior. $Cu_3(BTC)_2$ was also investigated at 80 °C to define an expected working capacity for the adsorbing and desorbing cycle in a temperature swing. Zeolite NaA was investigated in powdered, beaded and monolithic shape in order to estimate the loss of water adsorption capacity caused by the addition of binding agent. This was done at both 25 and 80 °C for the same reason than for $Cu_3(BTC)_2$. Although the water adsorption properties of zeolite X and silica gel are already known, the water adsorption isotherms at 25 and 80 °C will also be presented to establish a basis for discussion for the drying isotherms presented in chapter 7.

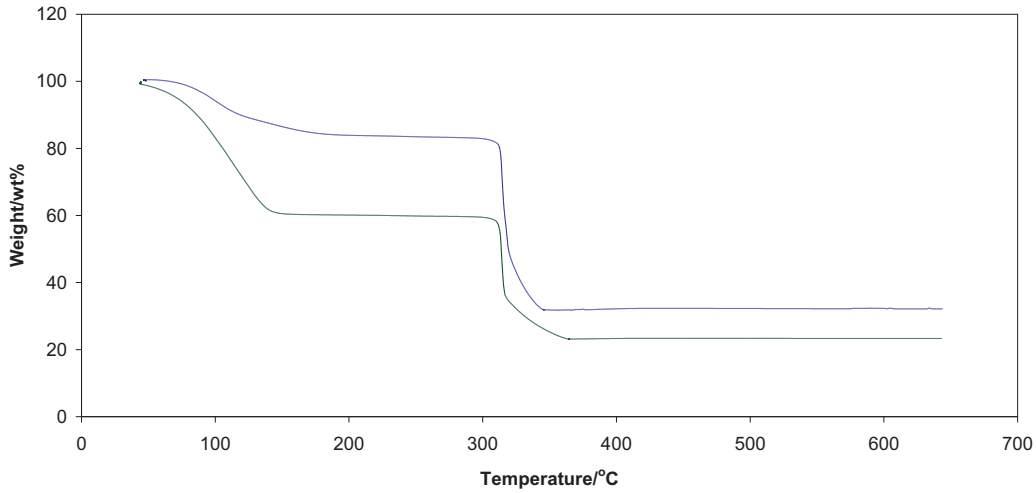

Figure 5.1.: Thermal gravimetric analysis of $Cu_3(BTC)_2$ samples. The blue curve shows the analysis of the $Cu_3(BTC)_2$ activated sample. The green curve belongs to a $Cu_3(BTC)_2$ sample that was stored at 50 % rel. humidity.

5.1.1. Water adsorption isotherms of powdered samples

The structure and characteristics of all investigated materials were discussed in chapter 2. The nitrogen physisorption isotherms of these materials are already known from literature and will not be discussed in detail, but only used as comparison to the water adsorption isotherms.

$Cu_3(BTC)_2$ water adsorption isotherms

$Cu_3(BTC)_2$ was chosen as possible water adsorbing agent, as it has free copper coordination sites available for adsorption of polar species. The water adsorbing property is already observable when activated $Cu_3(BTC)_2$ comes in contact with air and changes rapidly its color from turquoise blue to deep purple. The color change can be attributed to the coordination of water molecules to the copper sites. The thermal gravimetric analysis data of $Cu_3(BTC)_2$ (see figure 5.1) shows a steep decrease in weight in the temperature range from 25-100 °C indicating the loss of water adsorbed in the pores. $Cu_3(BTC)_2$ powder which was stored at defined relative humidity of 50% at 25 °C showed an even more pronounced weight loss. A possible use of $Cu_3(BTC)_2$ as desiccant was therefore anticipated and further investigated.

The nitrogen physisorption isotherm of $Cu_3(BTC)_2$ is of *type I* according to IUPAC classification. A two step adsorption process is also observed in the lower pressure region

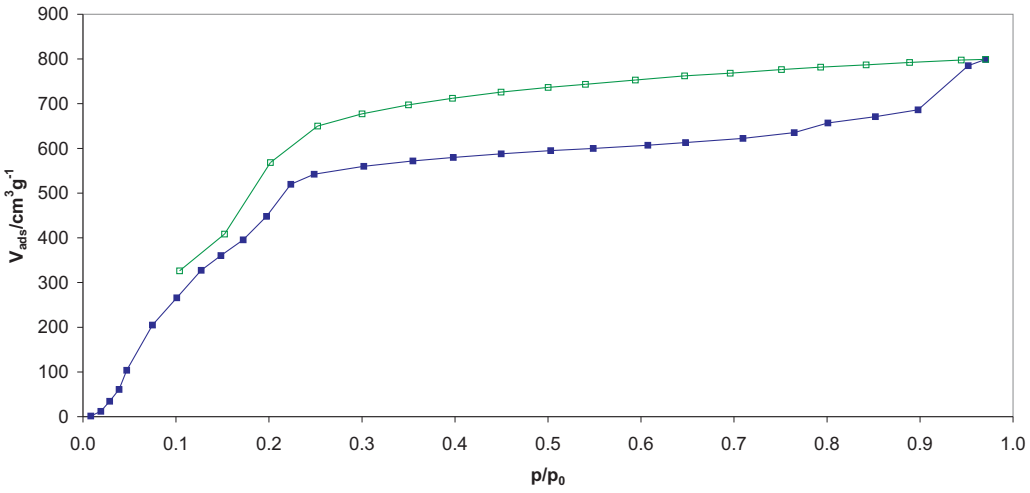

Figure 5.2.: Water adsorption (filled blue squares) and desorption (open green squares) of $Cu_3(BTC)_2$ at 25 °C.

due to the consecutive filling of the smaller and bigger pores, respectively [18]. Here, the smaller and more hydrophobic 6 Å pores are filled first followed by filling of the larger 9 Å pores. In contrast to the nitrogen isotherm, the water adsorption experiment yielded a completely different shape of both adsorption and desorption branch (see figure 5.2). The adsorption branch shows a two step adsorption process, with the first step in the region from p/p_0= 0.05-0.2. A second adsorption step that is much less pronounced occurs from p/p_0= 0.2-0.3, indicating the filling of the smaller pore, which is exclusively constituted of benzene rings. As the bigger pores are formed of paddle-wheel units, which are composed of copper clusters in their centers, the first filling step can be assigned to the filling of the bigger pores. Additionally, the adsorbed volume in the first step is much higher ($400\,cm^3g^{-1}$) than in the second adsorption step ($120\,cm^3g^{-1}$), which also accounts for the filling order. The isotherm then reaches a saturation plateau in the pressure range from p/p_0= 0.3-0.8. A third increase of adsorbed volume in the pressure range from p/p_0= 0.8-0.95 is the result of condensation in the interparticular voids of the powder. The desorption branch shows a slight hysteresis and noteworthy desorption only starts to begin at p/p_0= 0.25. Strong hydrogen bridging between the water molecules probably is the main reason for the hysteresis. Desorption occurs in a similar two step process like the adsorption. The smaller pore is emptied first in the pressure range from p/p_0= 0.25-0.1. The desorption of the water molecules in the bigger pores is not fully completed, it ends at p/p_0= 0.1. A part of the water remains adsorbed to the copper coordination sites. In spite of this assumption, the quantity of water molecules that

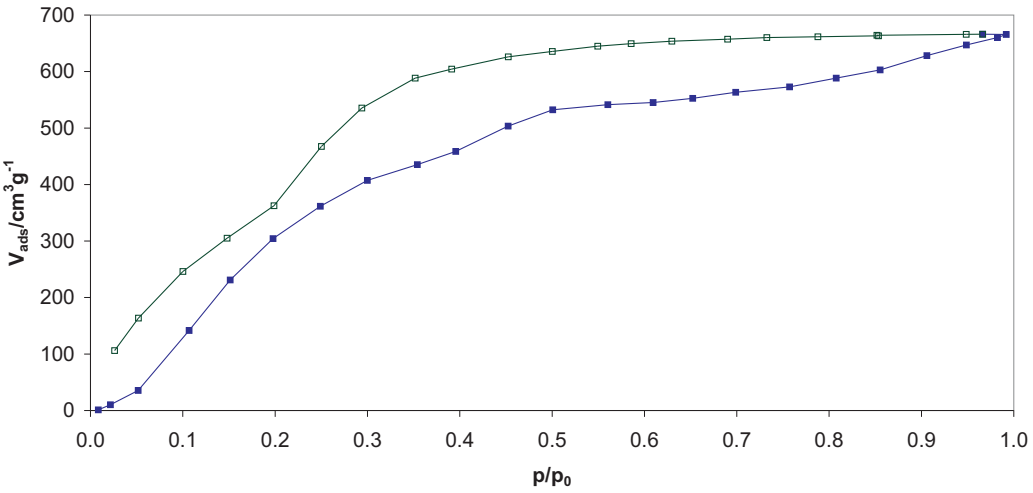

Figure 5.3.: Water adsorption (filled blue squares) and desorption (open green squares) of $Cu_3(BTC)_2$ at 50 °C.

remain in the pores is larger than the quantity that can be chemisorbed to the available copper sites. Both the missing closure of the hysteresis and the incomplete desorption of water can be attributed to a partial decomposition of the $Cu_3(BTC)_2$ framework. Moreover, a second recording of the isotherm on the same sample did not lead to the same result and confirmed the assumption that the material is not completely stable towards water. The water stability of $Cu_3(BTC)_2$ will be explicitly discussed in section 5.3.

The water adsorption isotherms of $Cu_3(BTC)_2$ were also recorded at 50 °C in order to investigate the amount of water that could be desorbed in a temperature swing. The isotherm is shown in figure 5.3. Since adsorption is an exothermic process, the usual outcome of the experiment ought to show the same shape of isotherm but a reduced total amount adsorbed. The isotherm in figure 5.3, clearly confirms this fact. The adsorption is slightly shifted to the right and the total volume adsorbed at $p/p_0 = 1$ is about 200 cm^3g^{-1} lower. The two adsorption steps are still identified, but less distinct than in the lower temperature measurement.

ZIF-8 water adsorption isotherms

ZIF-8 is a microporous MOF like $Cu_3(BTC)_2$. Compared to most MOF materials, ZIF-8 is known for its exceptional water stability [107] and therewith an interesting material for water adsorption purposes. Usually, most MOFs are not exceptionally stable to humidity. The nitrogen physisorption isotherm measured at 77 K shows the typical

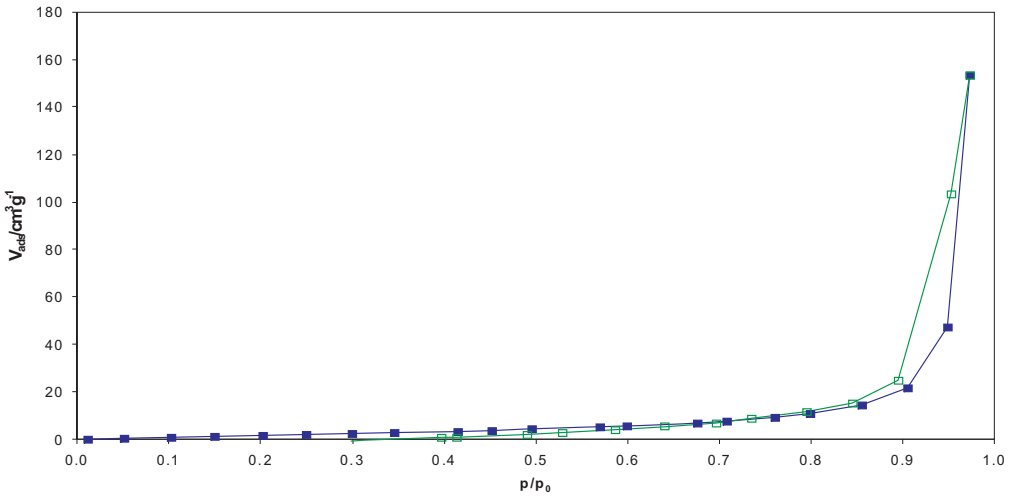

Figure 5.4.: Water adsorption (filled blue squares) and desorption (open green squares) of ZIF-8 at 25 °C.

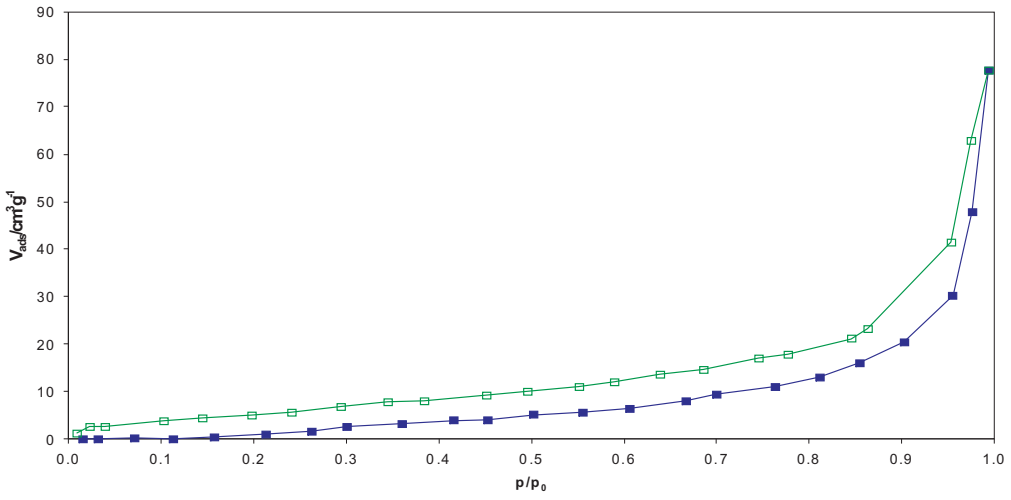

Figure 5.5.: Water adsorption (filled blue squares) and desorption (open green squares) of ZIF-8 at 50 °C.

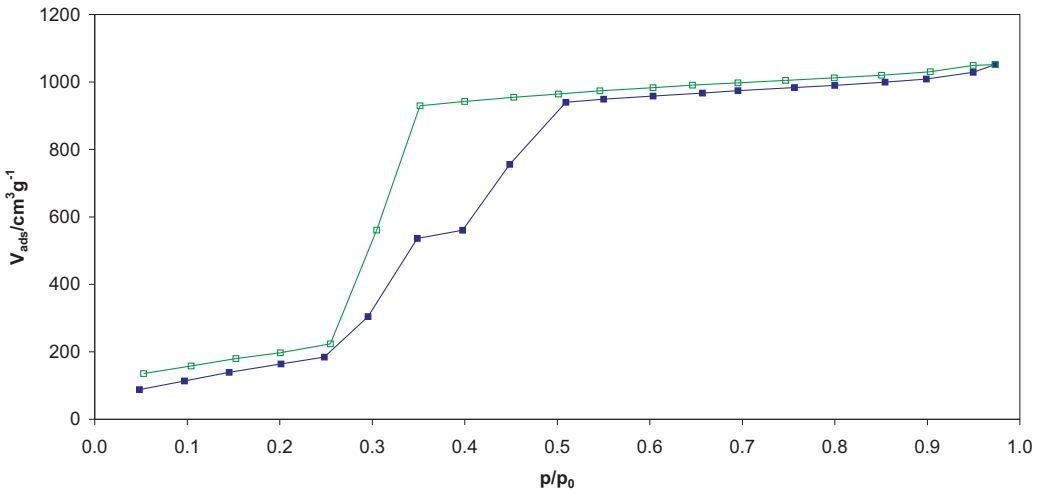

Figure 5.6.: Water adsorption (filled blue squares) and desorption (open green squares) of MIL-100(Fe) at 25 °C.

type I isotherm according to IUPAC classification like $Cu_3(BTC)_2$. The water adsorption isotherm is more of a *type III* shape indicating a weak adsorbent-adsorbate interaction (see figure 5.4). No adsorption occurs up to $p/p_0 = 0.6$ followed by a slight increase of adsorbed volume of about $10\,cm^3g^{-1}$ up to $p/p_0 = 0.8$. Water adsorption starts at $p/p_0 = 0.8$ and reaches its maximum with $150\,cm^3g^{-1}$ at $p/p_0 = 1$. The measurement at elevated temperature yields the expected outcome. The adsorbed volume of water is here even lower with $75\,cm^3g^{-1}$, see figure 5.5. Compared to the copper material, ZIF-8 is composed of zinc-clusters, which do not provide coordination sites for polar molecules. The highly hydrophobic character is probably also a cause for the high water stability.

MIL-100(Fe) water adsorption isotherms

Compared to $Cu_3(BTC)_2$ and ZIF-8, MIL-100(Fe) is a mesoporous MOF exhibiting a polymodal pore size distribution. The two large mesoporous cages of 25 and 29 Å in diameter are composed of microporous supertetrahedra [108]. MIL-100(Fe) revealed a nitrogen physisorption isotherm typical for microporous materials. Here, the uptake in the lower pressure regions is less steep as for example for $Cu_3(BTC)_2$. Two secondary uptakes at $p/p_0 = 0.06$ and $p/p_0 = 0.12$ [108] can be distinguished from the isotherm, which can be assigned to the filling of the mesoporous cages. Both the hydrophilic character given by the iron clusters and the mesoporous character are an indication for a possible use as drying material with high capacities. The water adsorption isotherm measured at 25 °C shows in the lower pressure region almost no water adsorption, see

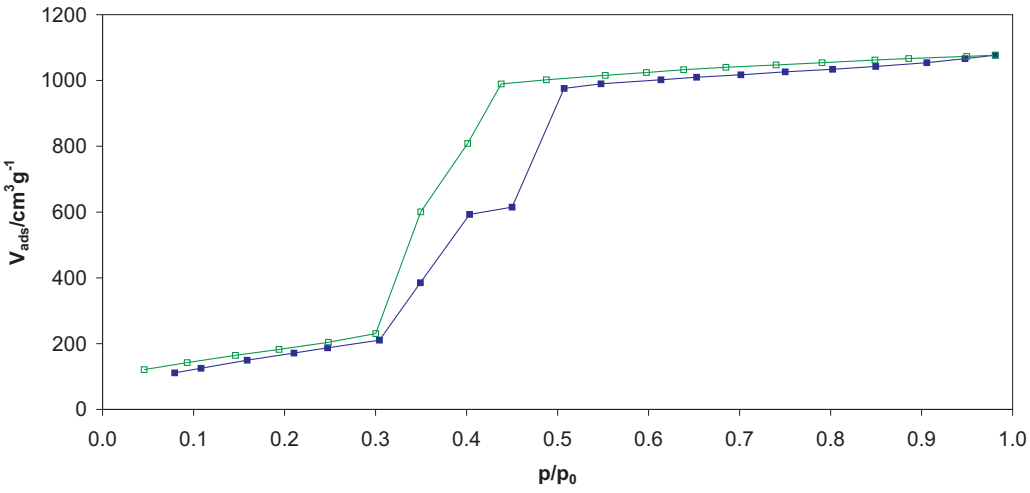

Figure 5.7.: Water adsorption (filled blue squares) and desorption (open green squares) of MIL-100(Fe) at 50 °C.

figure 5.6. Only a small amount of approximately $100\,cm^3g^{-1}$ is adsorbed at pressures below $p/p_0 = 0.5$. This volume is the result of the interaction of water with the iron centers. A second uptake occurs at $p/p_0 = 0.25$ immediately followed by a third step at $p/p_0 = 0.4$. These two step adsorption is the result of the filling of the mesoporous cages. The filling of the smaller 25 Å-cages occurs first, followed by the filling of the larger 29 Å-cage. The isotherm then levels off in a saturation plateau. The desorption branch only shows one distinct desorption step at $p/p_0 = 0.5$. Like $Cu_3(BTC)_2$, the water is not completely desorbed and adsorption and desorption branch do not close. The reason is probably the irreversible chemisorption of water to the iron centers.

The 50 °C measurement (see figure 5.7) yielded an unexpected result. Here, the total amount adsorbed was slightly higher with $30\,m^2g^{-1}$ for the elevated temperature experiment. This behavior can be caused by a small breathing effect of the flexible network.

MIL-101 water adsorption isotherms

MIL-101 is like MIL-100(Fe) a mesoporous MOF with a polymodal pore size distribution. Analogous to MIL-100(Fe), it has two mesoporous cages composed of microporous super tetrahedra. The mesoporous cages are slightly larger with 29 and 34 Å in size. The behavior of the MIL materials is therewith similar in both the nitrogen and the water adsorption experiment, only small differences are distinguishable. The nitrogen physisorption isotherm is here also of a typical *type I* shape [49] with two secondary

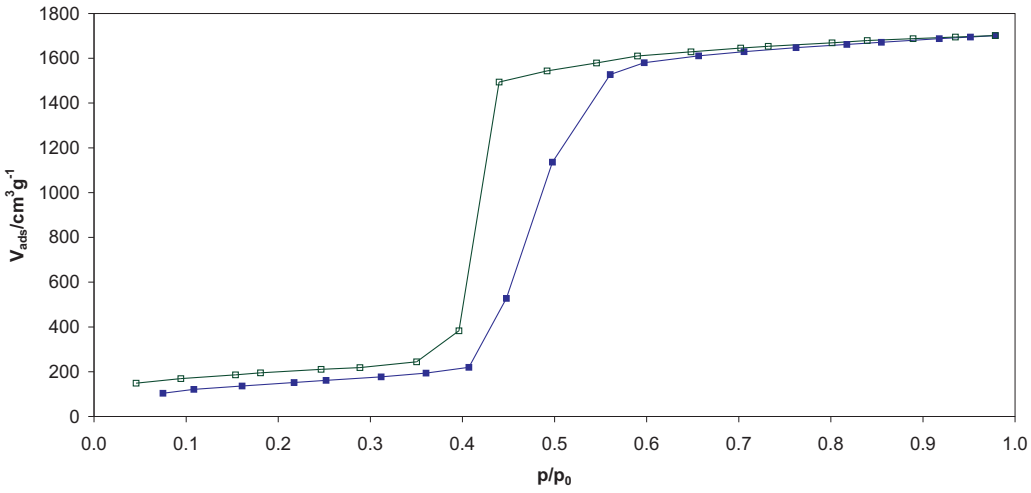

Figure 5.8.: Water adsorption (filled blue squares) and desorption (open green squares) of MIL-101 at 25 °C.

uptakes at $p/p_0 = 0.1$ and $p/p_0 = 0.2$ indicating the filling of the mesoporous cages. The exceptional stability of MIL-101 has already been reported [49]. Moreover, the high specific surface area and the hydrophilic character of the framework lead to the consideration to use this material as drying agent. As for $Cu_3(BTC)_2$ and MIL-100(Fe), the first small adsorption step occurs in the lower pressure region below $p/p_0 = 0.05$, which is similarly attributed to the interaction with the transition metal centers. Since the cages of MIL-101 are even larger than the cages in MIL-100(Fe), the first remarkable step in the water adsorption isotherm occurs at $p/p_0 = 0.4$ in one single step. The consecutive filling of the cages is here not visible. The difference in size of the pores is with 5 Å even larger than for MIL-100(Fe) with 4 Å. The pore filling can thus not only be influenced by the difference in size, but by the hydrophilic character. Apparently, the MIL-101 cages have a similar hydrophilicity leading to an almost concurrent filling behavior. In case of MIL-100(Fe), the hydrophilicity is distinct and the pore size is the crucial factor. Similarly, the desorption branch does not close and a part of the adsorbed volume remains chemisorbed in the pores (170 cm^3g^{-1}). The 50 °C measurement (see figure 5.9) also yields a similar trend: The total amount adsorbed is about 80 cm^3g^{-1} higher than for the lower temperature measurement. Like for the related MIL-100(Fe), this behavior can be attributed to a small breathing effect.

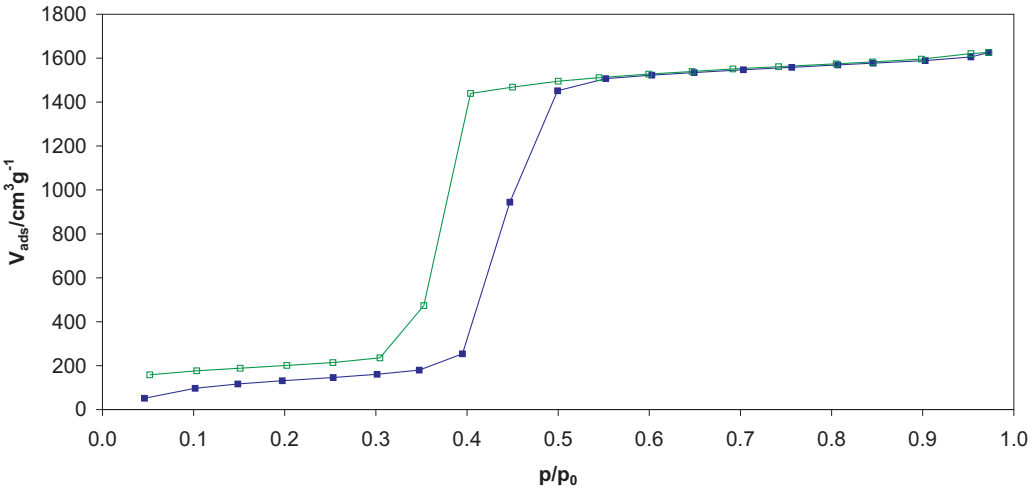

Figure 5.9.: Water adsorption (filled blue squares) and desorption (open green squares) of MIL-101 at 50 °C.

Silica gel water adsorption isotherms

The silica gel investigated in this work has a single point BET surface area of $630\,m^2g^{-1}$ according to the nitrogen physisorption measurement at 77 K, shown in figure 5.1.1. It shows a *type I* shaped isotherm with a steep rise to $125\,cm^3g^{-1}$ adsorbed nitrogen at $p/p_0 = 0.01$. The isotherm gradually increases for $100\,cm^3g^{-1}$ until $p/p_0 = 0.5$ and finally levels off. The experiment therewith revealed a microporous structure of the investigated silica gel.

Water adsorption isotherms of silica gel are shown in figure 5.11. The *type I* behavior in the nitrogen physisorption experiment is not clearly observable, the isotherm shows only a marginal rise in the pressure region $p/p_0 = 0.1$-0.5. In the case of water adsorption, the classification of isotherms according to IUPAC has to be chosen with care. As the adsorbent strongly interacts with the hydrophilic centers of the material, which are in these case silanol groups, a typical monolayer adsorption like in nitrogen physisorption is not given. Therefore, the isotherm should only be used to evaluate the hydrophilicity of the material rather than its pore structure.

In summary, the water adsorption isotherm confirms the typical behavior of silica gel that is more suitable for drying purposes at a higher relative humidity. A slight hysteresis is also observed for the isotherms and in both cases no closure point of adsorption and desorption branch occurs. In terms of nitrogen gas adsorption, this phenomenon occurs when the pore structure of the adsorbent is partly made of a bottle-neck geometry. Still, the isotherm should always close in the lower pressure region. In case of the water ad-

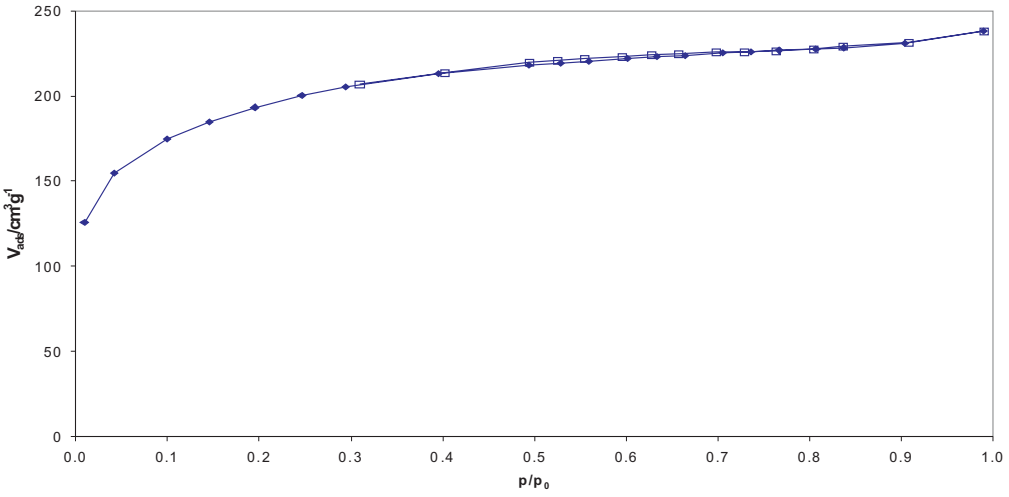

Figure 5.10.: Nitrogen adsorption isotherm of silica gel recorded at 77 K.

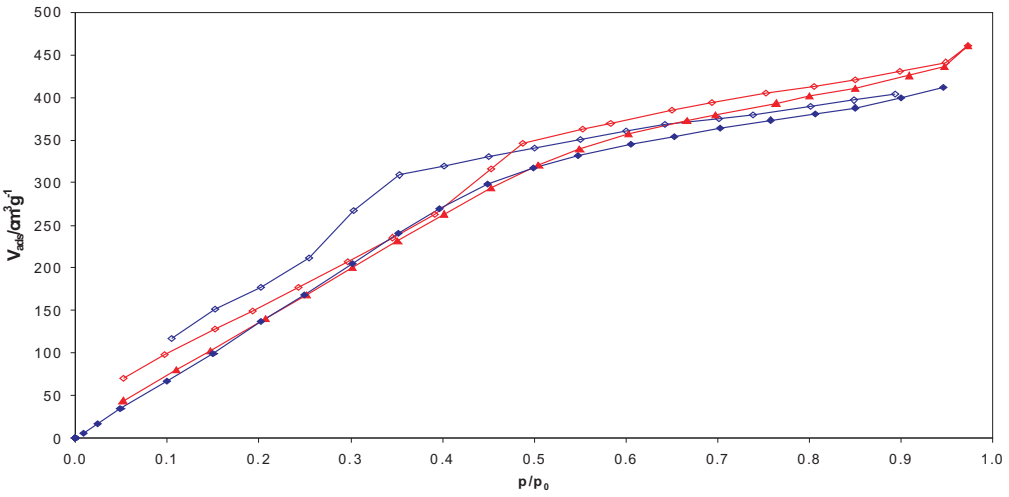

Figure 5.11.: Water adsorption isotherms of silica gel at 25 25 °C (blue) and 80 °C (red). Filled symbols depict adsorption and empty symbols desorption.

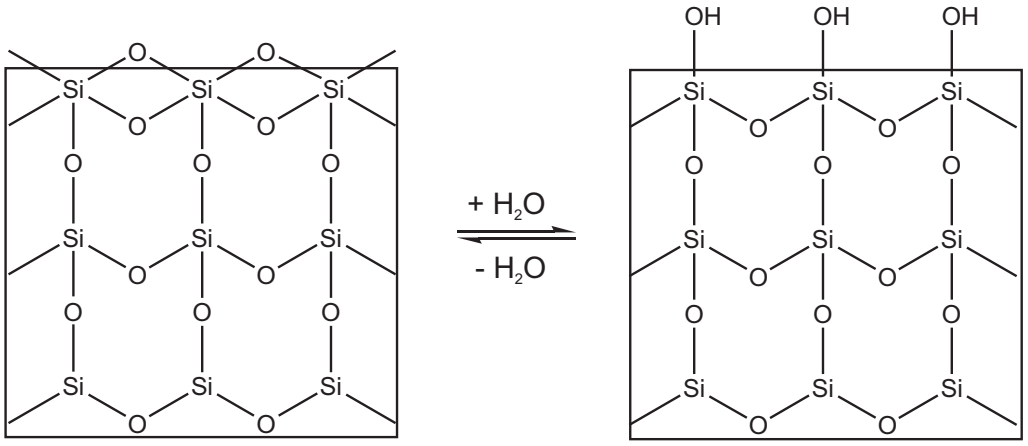

Figure 5.12.: Hydrolysis of siloxyl groups in silica gel.

sorption, this can only be attributed to chemisorption of water to the framework, which in the case of silica gel would be the hydrolysis of the siloxyl groups, see figure 5.12. Regarding temperature dependence, no significant difference in adsorption is observed. Only the hysteresis is much more pronounced in the 25 °C measurement. The reason is the temperature dependence of the hydrolysis of the siloxane groups. Lower temperatures favor the hydrolysis. Thus, the gap between adsorption and desorption branch is more distinct for the 25 °C measurement.

Heats of adsorption, total pore volume and bridging effect

An additional feature of water adsorption is the possibility to calculate the heats of adsorption (HOA). Temperature dependence was already discussed in the foregoing section. Those materials that showed complete stability towards water were also investigated regarding heat of adsorption and total pore volume. Table 5.1 lists total pore volumes determined from water and nitrogen adsorption, as well as the heats of adsorption and specific surface areas [89]. The heat of adsorption for $Cu_3(BTC)_2$ was not calculated, because of its insufficient stability towards water that could have falsified the outcome.

The average values of the materials for the heats of adsorption amount all to about 46 $kJmol^{-1}$. This value is close to the molar enthalpy of evaporation for water (40.69 $kJmol^{-1}$), which corresponds to the energy that is needed to generate hydrogen bridges between the single water molecules. This fact supports the theory that after formation of monolayers additional water molecules coordinate to the water molecules generating hydrogen bridges and therewith forming water clusters in the pores. To characterize the pore structure of all materials, the total pore volume was determined from both nitrogen

Material	S_a $[m^2g^{-1}]^a$	V_{N_2} $[cm^3g^{-1}]^b$	V_{H_2O} $[cm^3g^{-1}]^c$	HOA $[kJmol^{-1}]^d$
$Cu_3(BTC)_2$	1340	0.72	0.55	-
MIL-100(Fe)	1549	0.82	0.81	48.83
MIL-101	3017	1.61	1.28	45.13
ZIF-8	1255	0.64	0.02	44.68

Table 5.1.: Specific surface area S_a, total pore volume V_{N_2}, total pore volume V_{H_2O} and heat of adsorption (HOA) of the investigated MOFs.
[a] Single point BET surface area calculated at $p/p_0 = 0.3$ from nitrogen adsorption isotherm at 77 K
[b] Calculated at $p/p_0 = 0.9$ from nitrogen adsorption isotherm at 77 K
[c] Calculated at $p/p_0 = 0.9$ from water adsorption isotherm at 298 K
[d] Average value calculated from adsorption branches at 298 and 323 K

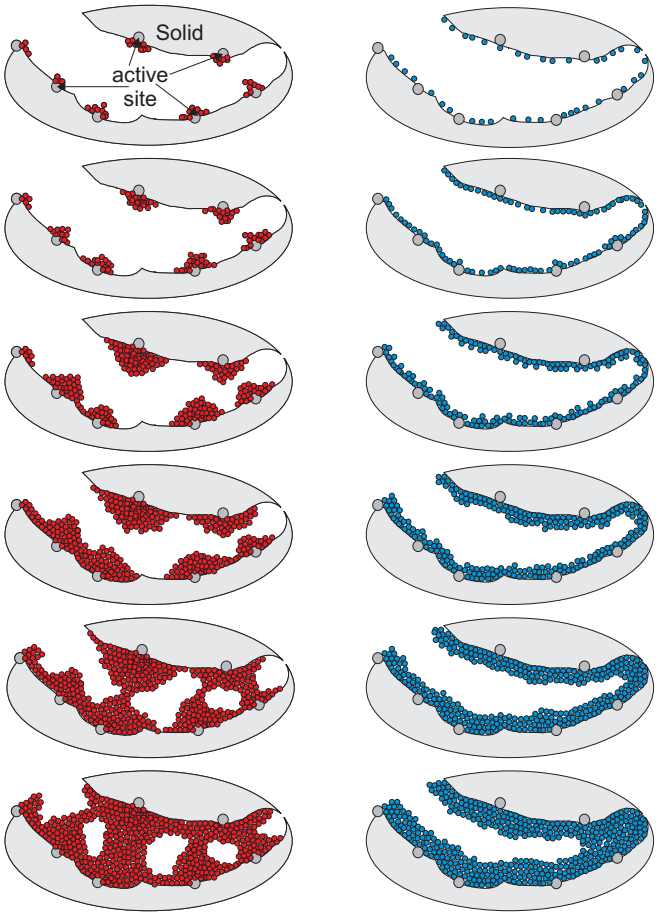

Figure 5.13.: Mechanism of adsorption of polar adsorbate (red dots) and nonpolar adsorbate (blue dots) onto a solid surface with hydrophilic active centers (grey dots).

and water adsorption isotherms. Surprisingly, the values are in all cases lower for the water adsorption. In case of $Cu_3(BTC)_2$, the lower value can be explained by the partial decomposition of the porous structure. ZIF-8 shows the most distinct difference for the total pore volume. This can be attributed to the high hydrophobic character of the framework. At p/p_0= 0.9, almost no water has been adsorbed and the interpretation of data becomes thus not significant in terms of the so-called "bridging effect". On the contrary, the phenomenon can be explained by this theory in case of the water stable materials MIL-100(Fe) and MIL-101. Figure 5.13 shows the example. Red dots depict water molecules. In contrast to water adsorption, nitrogen adsorption (blue dots) occurs consecutively without interaction of the adsorbate.

On very polar surfaces, like zeolites, the water adsorption process should be similar to adsorption of nitrogen by forming a continuous layer in the first step followed by multilayer adsorption. The MOF materials have polar sites due to the metal-oxygen clusters and very non-polar regions due to the organic and mostly aromatic linkers. The aromatic linkers represent the biggest fraction of the inner surface. Water molecules preferably adsorb to the metal-sites, avoiding the hydrophobic areas of the surface. Additional water molecules are bound by hydrogen bridges to these water nucleation sites resulting in the formation of small water clusters. When these water centers grow larger, they meet other water clusters in the pores, for example a cluster of the opposing pore wall. The latter results in the occurrence of free space in the pore above the hydrophilic area and therefore in an apparently reduced pore volume. Due to the strict formation of monolayers and micropore filling in nitrogen adsorption, the calculated pore volume is here always larger than from water adsorption.

Conclusion

Water adsorption isotherms were used to characterize promising MOF materials. The main reason for the different outcome of water and nitrogen adsorption was both the nature of the linker and the metal cluster. The pore size also played an important role. The pore volume was calculated for the water stable materials MIL- 100(Fe), MIL-101 and ZIF-8 for both water and nitrogen adsorption at p/p_0= 0.9 yielding remarkable differences. This phenomenon was explained by the bridging effect that occurs in water adsorption. The material $Cu_3(BTC)_2$ has the highest affinity towards water and might thus be the most promising MOF for drying applications. However, the stability of $Cu_3(BTC)_2$ towards water seems questionable. The water stability will be discussed in detail in the following sections of this chapter. As the MIL materials MIL-101 and MIL-100(Fe) as hydrophilic mesoporous compounds and ZIF-8 as a highly hydrophobic

microporous material show stability towards water, they could be used in drying applications. Compared to $Cu_3(BTC)_2$, the hydrophilicity is less stringent. ZIF-8 shows almost no water adsorption. The MIL materials adsorb water at $p/p_0 \geq 0.3$, which makes them promising for drying at higher relative humidity. The regeneration is thus easier to achieve. $Cu_3(BTC)_2$ would be a better candidate for drying of trace water. In summary, water adsorption isotherms are a useful extension to nitrogen physisorption isotherms. The combination of both measurements provides a detailed insight into the surface characteristics of the materials.

5.1.2. Water adsorption isotherms of molded samples

The water adsorption properties of both the zeolite and $Cu_3(BTC)_2$ monolith were also investigated. The preparation of the monolithic samples and the characterization is extensively described in chapter 4. Naturally, the total adsorption capacity is reduced when active powders are mixed with additives and shaped to monoliths or beads. The reason is on the one hand the reduced total amount of the active species and on the other hand the possible interaction of the additives with the active component. Thus, a reduced total amount of adsorbed water was expected.

Water adsorption isotherm of $Cu_3(BTC)_2$ monolithic samples

The water adsorption of small pieces of the monolithic samples were all measured at 25, 50 and 80 °C. As adsorption is an exothermic process, adsorption should be less efficient at elevated temperatures. The results of the water adsorption experiment confirmed this fact. In figure 5.14, both adsorption and desorption at 25 and 50 °C are plotted together. The adsorption branch of the 25 °C measurement has a similar shape compared with the powdered $Cu_3(BTC)_2$ measurement. Here, the two step adsorption is less pronounced, as the monolith is not made of pure $Cu_3(BTC)_2$. The same is valid for the 50 °C measurement, that shows even less distinct adsorption steps. Additionally, the adsorption occurs at slightly higher relative pressures leading to less steep uptakes than in the 25 °C experiment.

The saturation plateau is reached at smaller volumes in case of the enhanced temperature measurement, which confirms the assumption made beforehand. The difference in adsorbed amount at $p/p_0 = 0.5$ is approximately 70 cm^3g^{-1} less. Both measurements show an additional increase in the pressure region of $p/p_0 = 0.8$-1.0, which is also observed for the powdered samples. The explanation for this uptake is again the condensation of water in the interparticular voids. The desorption branches show the same behavior as

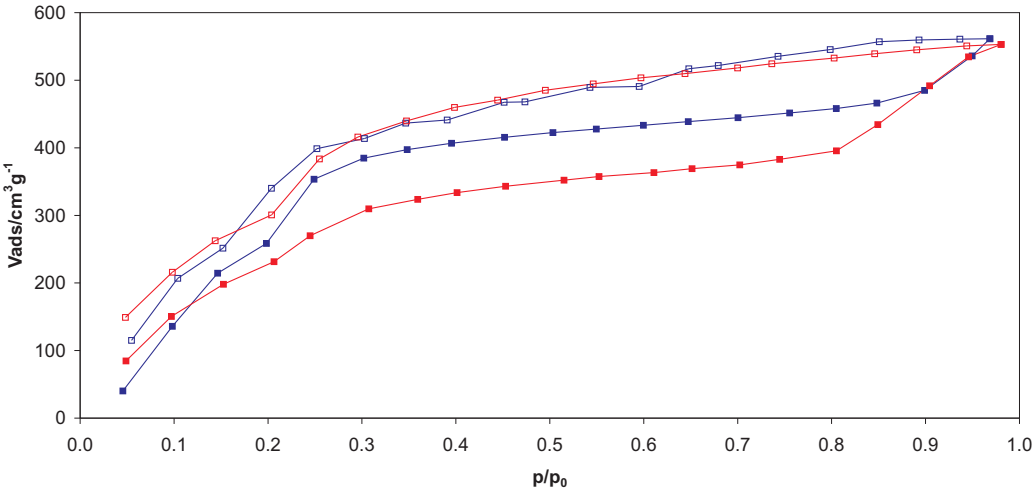

Figure 5.14.: Water adsorption isotherm of the $Cu_3(BTC)_2$ monolith. Filled squares depict the adsorption measurement, empty squares the desorption measurement. Blue curves were measured at 25 °C, red curves at 50 °C.

the powder samples and will therefore not be discussed. The 80 °C measurement was different to the 25 and 50 °C measurement and was therefore plotted in another diagram (figure 5.15). The two step adsorption is no longer discerned in the adsorption branch and the increase is even less steep than in the 50 °C measurement. Moreover, a saturation plateau is not clearly observable. Only the additional adsorption step at higher relative pressure resembles the 25 and 50 °C measurements. The adsorbed amount of water is for this experiment 50 cm^3g^{-1} less (at p/p_0= 0.5) than for the 50 °C isotherm. The desorption branch has a completely different shape. The hysteresis loop is not observable. Instead, the first and most distinct desorption step occurs already at p/p_0= 0.7 and the desorption branch crosses the adsorption branch. This fact hints at a decomposition of the framework. From p/p_0= 0.7-1.0, only slight desorption occurs and 170 cm^3g^{-1} remain adsorbed to the material.

Water adsorption isotherms of zeolite NaA molded samples

Zeolite 4A shows the *type I* isotherm typical for microporous materials. Figure 5.16 shows the water adsorption isotherms of powdered zeolite A as well as a commercial beaded product and the monolithic sample. The powdered sample showed the steepest adsorption uptake in the lower pressure region compared with the molded samples, since there is no binding agent that reduces the solid fraction of the adsorbent. The total adsorbed amount in the saturation region (p/p_0= 0.2-0.9) is also the highest observed

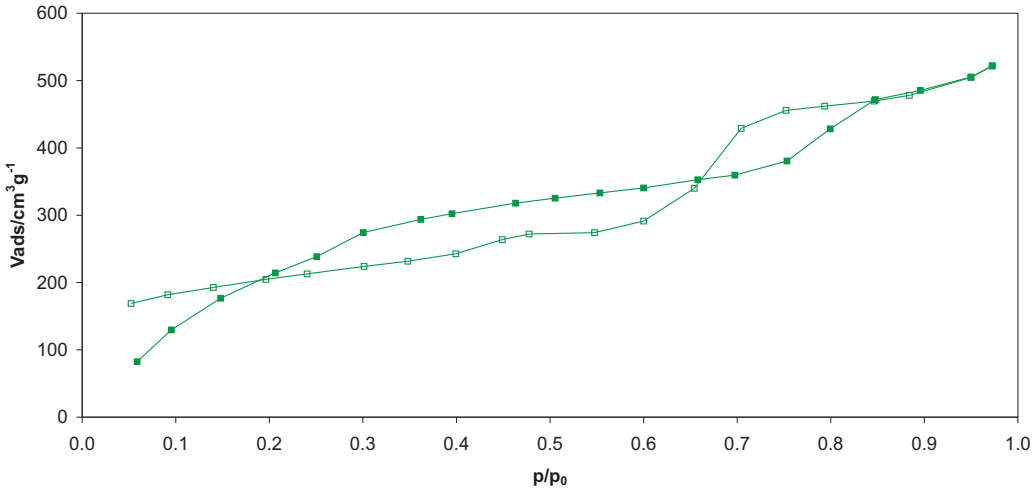

Figure 5.15.: Water adsorption isotherm at 80 °C of $Cu_3(BTC)_2$ monoliths. Filled squares depict the adsorption measurement, empty squares the desorption measurement.

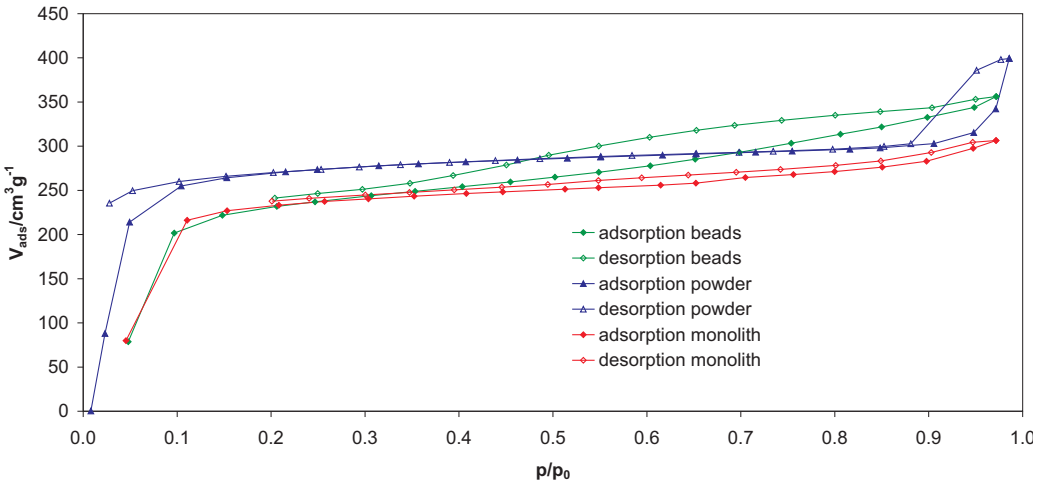

Figure 5.16.: Water adsorption isotherms of zeolite NaA powdered, beaded and monolithic samples at 25 °C.

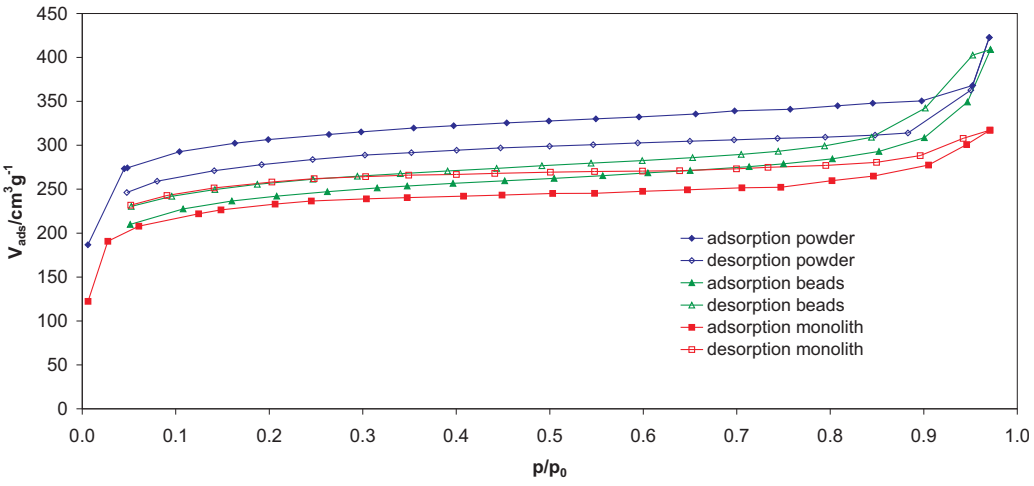

Figure 5.17.: Water adsorption isotherms of zeolite NaA powdered, beaded and monolithic samples at 80 °C.

for the zeolite NaA samples. Compared to the molded samples it is only slightly higher with 286 cm^3g^{-1} (at p/p_0= 0.5). At p/p_0= 0.5 the beaded sample adsorbs 270 cm^3g^{-1} and the monolithic sample 250 cm^3g^{-1}. The monolithic sample can therefore compete against the commercial product and does not loose capacity compared to the powdered sample.

The water adsorption isotherms of all three samples were also recorded at 80 °C. As shown in figure 5.17, the total adsorbed amount of all samples decreases only slightly at lower temperatures. For the use in a technical application, the efficiency would be not sufficient for the application of a thermal swing adsorption cycle since the working capacity is too low.

Conclusion

The monolithic samples of both $Cu_3(BTC)_2$ and zeolite NaA can compete with the commercial beaded products. The total adsorption capacity is comparable. Besides a reasonable total capacity, a good kinetic performance is important for industrial applications. The kinetic performance will be investigated and discussed in the following section.

Silica gel shows a different water adsorption behavior compared to zeolite NaA and $Cu_3(BTC)_2$. Water adsorption occurs here only at higher values of p/p_0. The adsorption capacity is comparable.

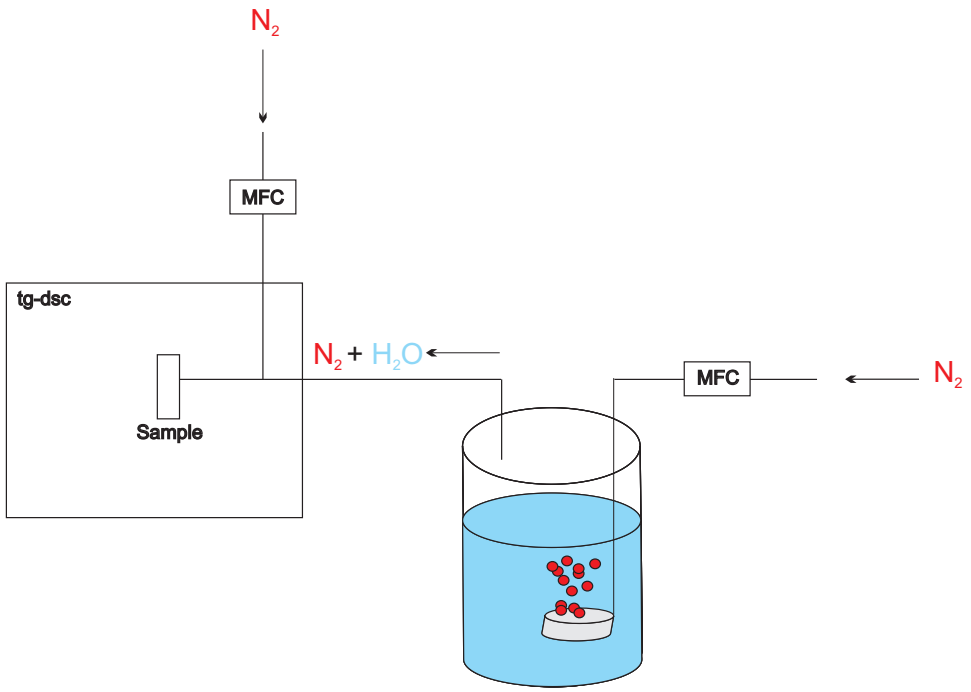

Figure 5.18.: TG-DSC experimental setup with gas flow unit.

5.2. Water adsorption kinetics

In order to assess the kinetic performance of the monolithic samples, dynamic water adsorption experiments were performed. The experimental equipment consisted of a thermal gravimetric setup with a differential calorimetric coupling. The thermal gravimetric unit was equipped with a gas-flow unit, which allowed precise adjustment of moist nitrogen gas streams. A scheme of the equipment is shown in figure 5.18. The moist stream was generated by purging a tempered water bath with nitrogen gas. The calculation of the humidity is described in the following. The content of water vapor of a gas is derived from the ideal gas law

$$p \cdot V = nRT$$

where p is the pressure, V the volume, n the molar amount, R the ideal gas constant and T the temperature. The humidity of a gas can be described using the following equation:

$$p_w \cdot V_{wl} = m_w \cdot R_w \cdot T \cdot \frac{1}{M_w}$$

with

p_w = partial pressure of H_2O at 298 K = 3163.23 hPa

V_{wl} = volume of the gas = 1 l

m_w = mass of water
M_w = molar mass of water = 18 $gmol^{-1}$
R_w = gas constant of water = 461.51 $Jkg^{-1}K^{-1}$

$$m_w = \frac{p_w \cdot V_{wl}}{R_w \cdot T \cdot \frac{1}{M_w}}$$

If a volume V_{wl} of 1 l was assumed at a temperature of 298 K, the amount of water adds up to 41.4 mg, which equals a gas stream of 4.14 mg per 100 ml. The values for the partial pressure of water are tabulated and correspond to the saturation vapor pressure of water over a liquid phase at a given temperature (in this case 3163.23 hPa at 298 K [109]).

Experimental

In a typical experiment, about 25 mg of adsorbent was filled in an Al_2O_3 crucible. The crucible was placed in the thermal gravimetric balance and a temperature program was run. All samples were outgassed for 10 hours. Zeolitic samples were activated at 200 °C, $Cu_3(BTC)_2$ samples at 150 °C. During activation, a purge stream of 60 ml/min of dry nitrogen was applied. The adsorption program was immediately started after the activation program. Here, the sample was also purged with 60 ml/min N_2, whereof 40 ml was dry N_2 and 20 ml was purged through the tempered water reservoir. According to equation 5.2, where $p_{(H_2O)}$ is the partial pressure of the dry N_2 stream and $p_{(H_2O)}{}^*$ the saturated partial pressure of the moist N_2 stream, the relative humidity (RH) of the purge stream was 33.3%

$$\mathrm{RH} = \frac{p_{(H_2O)}}{p_{(H_2O)*}} \mathrm{x}100\% \tag{5.1}$$

$$\mathrm{RH} = \frac{13.79\ \mathrm{gcm}^3}{41.4\ \mathrm{gcm}^3} \mathrm{x}100\% \tag{5.2}$$

$$\mathrm{RH} = 33.3\% \tag{5.3}$$

TG-DSC experiments of powdered samples

In section 5.1, the water adsorption isotherms of both $Cu_3(BTC)_2$ and zeolite NaA were measured. The total adsorbed volume of $Cu_3(BTC)_2$ exceeded the zeolite significantly.

In a first experiment, the monolithic and the powdered samples of zeolite NaA and $Cu_3(BTC)_2$ were kept for 24 hours at a relative humidity of 50 % at 50 °C. A thermal gravimetric analysis was performed on all samples. Even if the TGA of the zeolitic samples were already shown in chapter 4, the data are once again included in the following

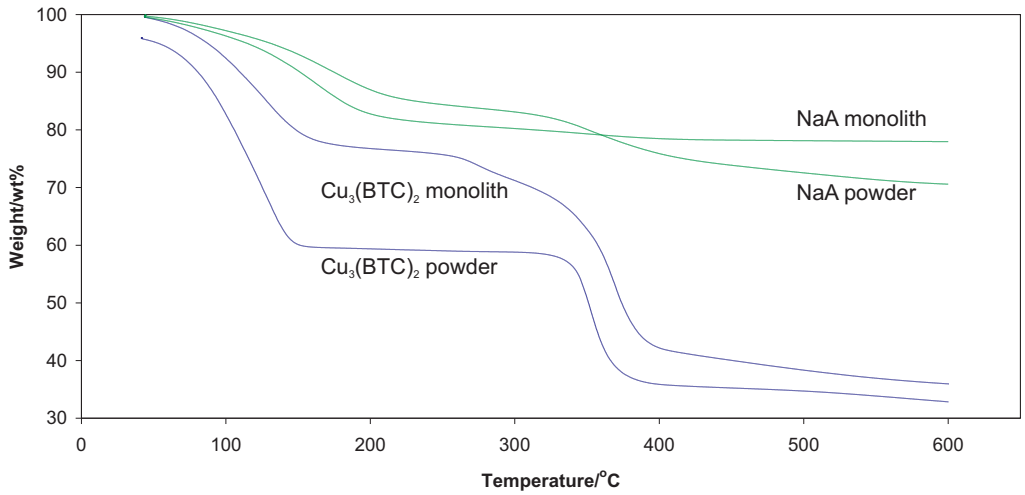

Figure 5.19.: TGA of powdered and monolithic NaA and $Cu_3(BTC)_2$ samples.

diagram. The TG analysis of the $Cu_3(BTC)_2$ samples in figure 5.19 show a pronounced weight loss at lower temperatures (temperature range 40-150 °C) that can be attributed to the desorption of water. The weight loss of the $Cu_3(BTC)_2$ powdered sample is with 41 wt% much higher than the weight loss of the zeolite powdered sample that looses only 19 wt%. The analysis of the monolithic samples yields similar results. Here, $Cu_3(BTC)_2$ looses 24 wt% and zeolite NaA 15 wt% of water. For the kinetic experiments, somewhat lower values are expected, as the relative humidity in this case was with 50% much higher.

The kinetic data were recorded at a relative humidity of 33.3%. The type of crucible that is used strongly influences the kinetics. The results may therefore not be interpreted absolutely, but just for comparison of the different materials. In a first series of measurements, a wired platinum crucible was used. In order to fill the crucible, it had to be lined with filter paper, especially in the case of powdered samples. All data obtained from the measurement in the platinum crucible were different and the absolute values could not be reproduced. The paper used for the measurements always adsorbed water itself, which might be a reason for the different results. Hence, another crucible made of Al_2O_3 was chosen, which led to stable results. The data of the powdered samples are shown in figure 5.2. Initially, the kinetic adsorption is approximately the same for both materials. After one hour, the difference in adsorbed amount is only 0.66 wt%. The difference increases to 1.25 wt% after 2 hours. The saturation value for zeolite NaA is reached at 20.74 wt% after 230 minutes. $Cu_3(BTC)_2$ adsorbs more water with 37.3 wt%, but equilibrium is attained only after 480 minutes.

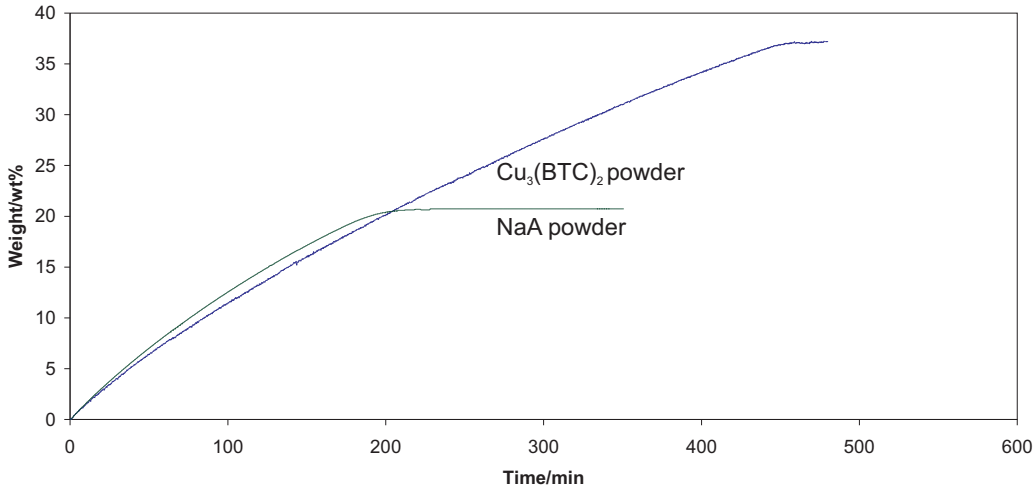

Figure 5.20.: Kinetic water adsorption of NaA and $Cu_3(BTC)_2$ powdered samples using an Al_2O_3 crucible.

In summary, $Cu_3(BTC)_2$ has no advantage over zeolite A regarding adsorption kinetics. Water adsorption happens slower than for the zeolite. Still, the absolute adsorption capacity is higher for $Cu_3(BTC)_2$.

TG-DSC experiments of monolithic samples

The results of the monolithic samples yielded another outcome than the powdered ones. Figure 5.21 shows the adsorption curves for both $Cu_3(BTC)_2$ and zeolite NaA monolithic samples. In this case, $Cu_3(BTC)_2$ shows a faster adsorption rate than zeolite NaA. After one hour of measuring time, $Cu_3(BTC)_2$ had already adsorbed 12.12 wt%, which accounts for more than one third of the total capacity (30.92 wt%). At the same time, the zeolite had adsorbed 8.64 wt%, which is more than 40% of the total capacity (20.20 wt%). After two hours of reaction time, the difference in adsorbed amount is even higher with 14.55 wt% for the zeolite sample and 19.75 wt% for the $Cu_3(BTC)_2$ sample. In summary, the $Cu_3(BTC)_2$ monolith has both a better water capacity and higher adsorption capacity than the zeolitic monolith.

Comparison of TG-DSC experiments with TGA and water adsorption isotherms

Table 5.2 summarizes the TG-DSC results for all samples, as well as the adsorbed amount of water obtained from the water adsorption isotherms at $p/p_0 = 0.3$, which corresponds to a relative humidity of 33%. Thus, the values obtained from both measuring methods

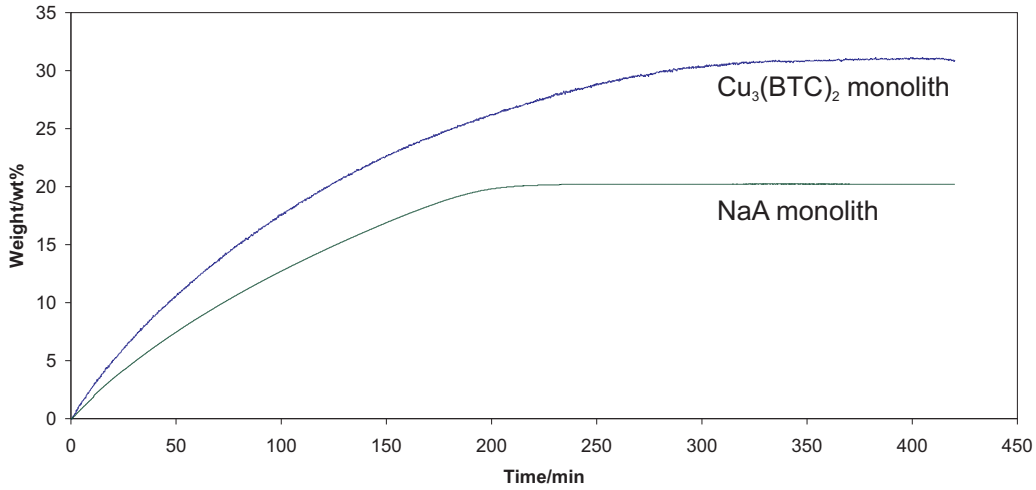

Figure 5.21.: Kinetic water adsorption of NaA and $Cu_3(BTC)_2$ monolithic samples.

	NaA powder	NaA monolith	$Cu_3(BTC)_2$ powder	$Cu_3(BTC)_2$ monolith
Isotherm m^*_{ads} [wt%]	14.71	19.32	45.02	30.92
TG-DSC m^{**}_{ads} [wt%]	20.95	20.20	37.21	31.07

Table 5.2.: Water adsorption capacities of NaA and $Cu_3(BTC)_2$ samples determined with different methods.
*determined at p/p_0= 0.3
**determined at a relative humidity of approximately 33.3%

should be comparable. The results for the monolithic samples correspond well with each other. The minor variations can be attributed to the slight difference in humidity at which the values were measured. In contrast, the values of the powdered sample are not comparable. In case of $Cu_3(BTC)_2$, the TG-DSC analysis yielded a lower value. The opposite is valid for the zeolite NaA powder. Here, a higher value was obtained from the TG-DSC analysis.

Conclusion

Generally, the water adsorption kinetics of $Cu_3(BTC)_2$ are almost comparable to zeolite NaA. In case of the monolithic samples, adsorption kinetics are better for $Cu_3(BTC)_2$.

5.3. Water stability

Water stability is of great importance for any use in industrial applications. Materials that even slightly decompose are undesirable for a use at ambient conditions. These materials would require careful treatment and therewith expensive technologies.

Stability after direct contact with water

All MOF materials were tested regarding their water stability by using a simple test method. All samples were immersed in deionized water and heated to 50 °C for 24 hours. They were then filtered and dried at ambient conditions. ZIF-8 and both MIL materials showed no change in their XRD patterns and were therefore classified as water stable. $Cu_3(BTC)_2$ was investigated further, as the water adsorption experiments already suggested certain instability. This simple experiment confirmed that the use of $Cu_3(BTC)_2$ as desiccant is not suitable. Direct contact with water changes the framework irreversibly as can be seen in the XRD pattern in figure 5.22. A use of $Cu_3(BTC)_2$ in the air drying cartridge is thus questionable as the adsorbent has to tolerate a high relative humidity. Test rig experiments with $Cu_3(BTC)_2$ for compressed air drying are discussed in chapter 6. Even though $Cu_3(BTC)_2$ decomposed in water, a use for adsorption of traces of water, for example in sensing technology, still seems to be possible.

Stability after water adsorption

Since $Cu_3(BTC)_2$ turned out to be unstable when immersed in water, advanced investigations regarding water stability were made. XRD experiments showed a complete change in structure, after a direct contact with water. The specific surface area was measured after the recording of water adsorption isotherms at several temperatures, as even pronounced decomposition of the framework cannot be detected by XRD.

Table 5.3 lists specific surface areas of $Cu_3(BTC)_2$ after the water adsorption isotherms at 25, 50 and 80 °C were measured. Already at 25 °C, the framework looses 55 % of its specific surface area. After the 50 °C recording, the value decreases by additional 3 %. After the 80 °C measurements, almost no porosity remains.

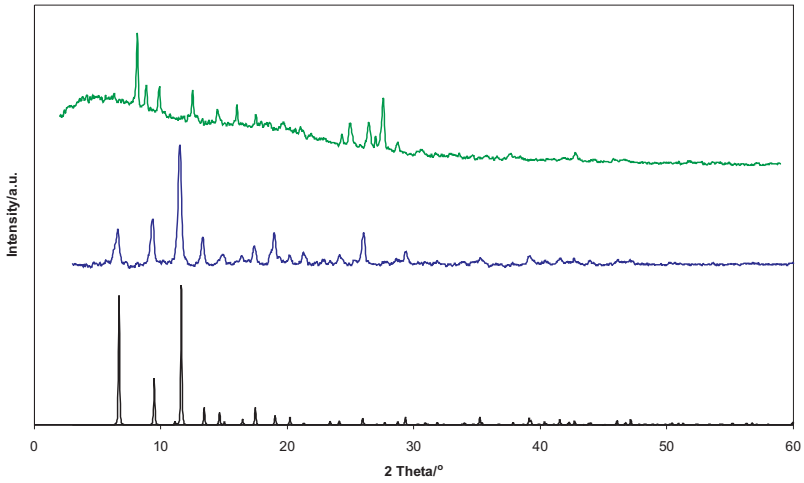

Figure 5.22.: XRD patterns of several $Cu_3(BTC)_2$ samples: The black pattern shows the calculated pattern, the dark blue the untreated sample and the light blue one the sample after the water contact.

Sample	S_a $[m^2g^{-1}]$
As made	1508
After H_2O adsorption (25 °C)	822
After H_2O adsorption (50 °C)	785
After H_2O adsorption (80 °C)	3

Table 5.3.: Specific surface areas of $Cu_3(BTC)_2$ after water adsorption at 25, 50 and 80 °C. Single point BET surface area calculated at $p/p_0 = 0.3$ from nitrogen physisorption at 77 K.

Conclusion

As the framework decomposes even at ambient temperatures during water adsorption in the gaseous phase, the use of $Cu_3(BTC)_2$ in any drying applications is therefore questionable.

6. Air drying

In order to assess the drying capacity of $Cu_3(BTC)_2$, the material was tested on an air drying test rig [110] of the *Mahle Filtersysteme GmbH*. On the one hand, the material was tested as pelleted bodies that were provided by the *BASF Group*. Another point of investigation was to compare the drying capacity of the monolithic samples with the beaded or pelleted form. In the following, the test program of the test bench is described.

Test procedure

A scheme of the setup is shown in figure 6.1. Principally, the dryer is purged with a moist compressed air stream with a relative humidity of 97-100%. The humid air is generated in a water vessel with an external heating jacket. The flow rate is adjusted to 330-350 $lmin^{-1}$, which is regulated by a PID controller. The inlet temperatures vary from 69-73 °C. System pressure is adjusted to 12 bars. Both temperature and pressure are recorded online at the in- and outlet of the cartridge.

The test procedure of the MAHLE test rig is based on the method of the SAE standard [111] (Society of automotive engineers) with only minor variations. Here, the cycling is dependent on time; whereas the SAE applies pressure controlled cycling. A graphical sketch of the temporal test procedure is shown in figure 6.2.

The test procedure involves two principal parts. The first part serves to ensure an even conditioning of all samples. The cartridge is loaded and reloaded with a cycle time of 210 seconds until the dew point depression (D_p) falls below 5 °C. The cartridge is then defined as saturated. The saturation is followed by a recovery phase with cycle times of 30 seconds. Regeneration continues until D_p exceeds 30 °C. This first step of saturating and recovery is iterated three times. After the conditioning phase, the actual performance test is started. The loading time is adjusted to 20 seconds for 2 hours. After the 2 hours, it is gradually increased by further 10 seconds. The cycling continues until a D_p of 14 °C is reached. The cycle time is recorded, as it will be applied for the last step of the performance test. The cycling continues in 10 second steps until the cartridge reaches a D_p of 5 °C. At this D_p one can assume a total saturation of the

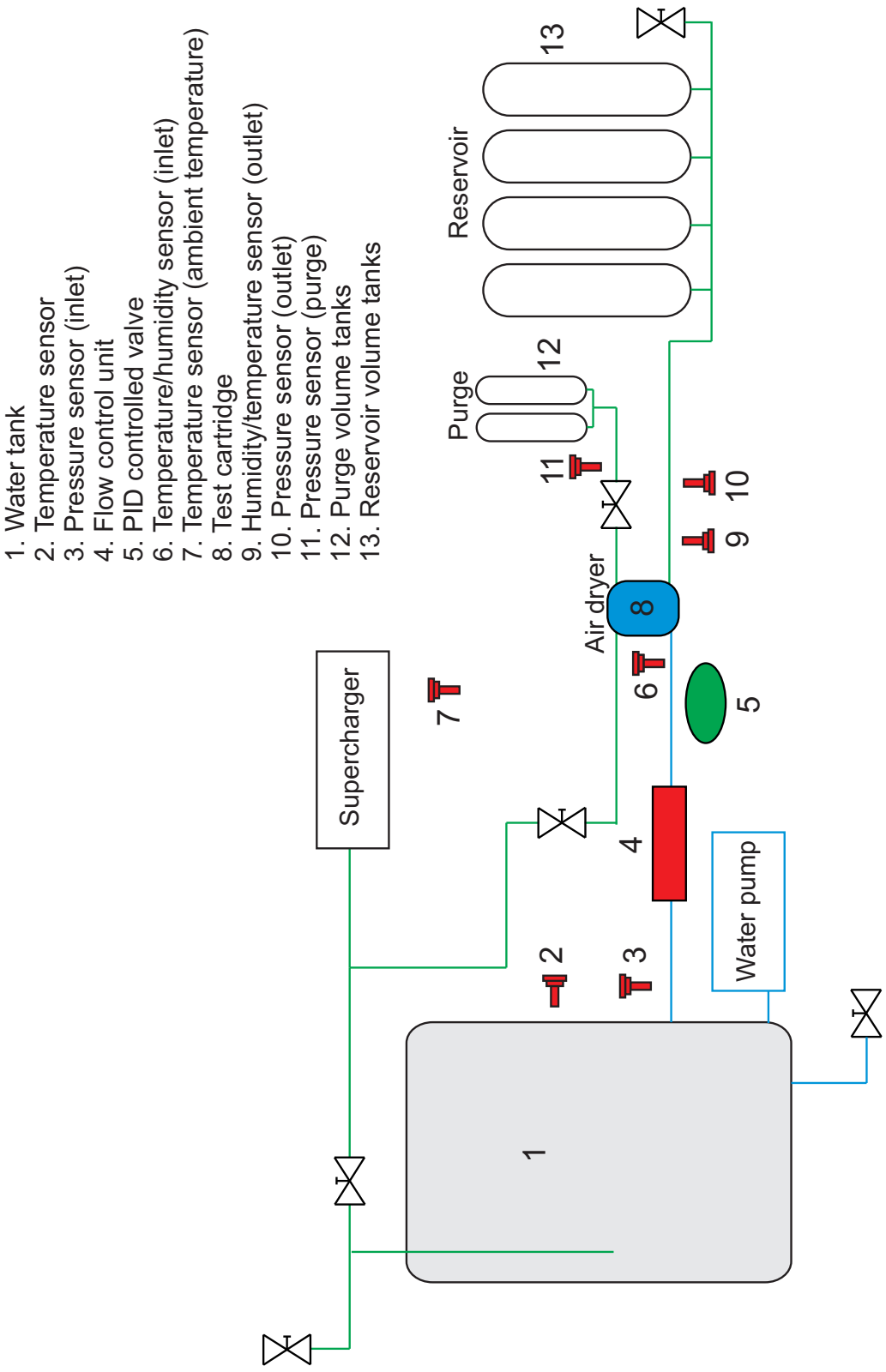

Figure 6.1.: Flow chart of the air drying test rig

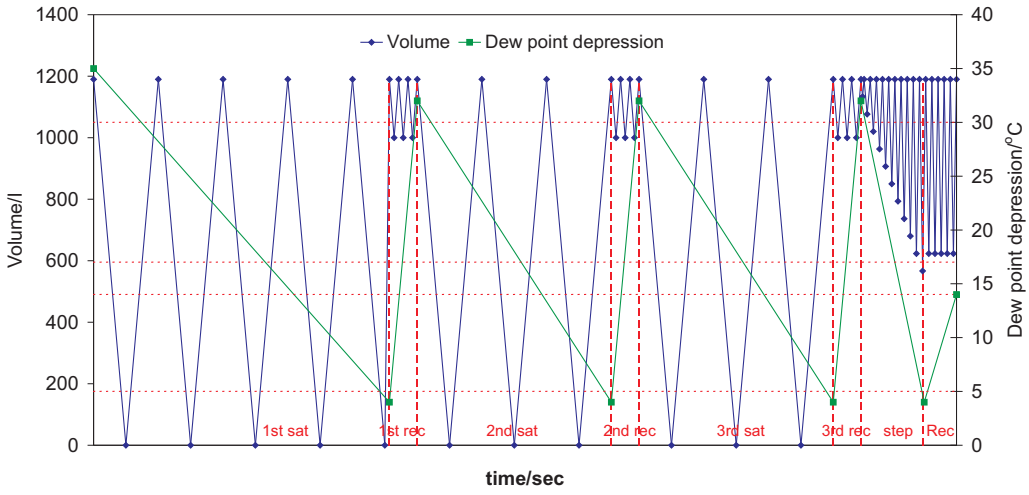

Figure 6.2.: Temporal course of the air drying test rig test procedure including conditioning phase and performance test.

desiccant. In order to test if the material still can be recovered, cycling continues until a D_p of 14 °C is obtained. As cycle time, the one that was recorded after a D_p of 14 °C was reached is chosen. A cartridge that does not reach a D_p of 5 °C or 15 °C is categorized as insufficient.

The picture in figure 6.3 shows a photograph of the test rig. The compressor unit is not visible, as it is located in the room behind the rig.

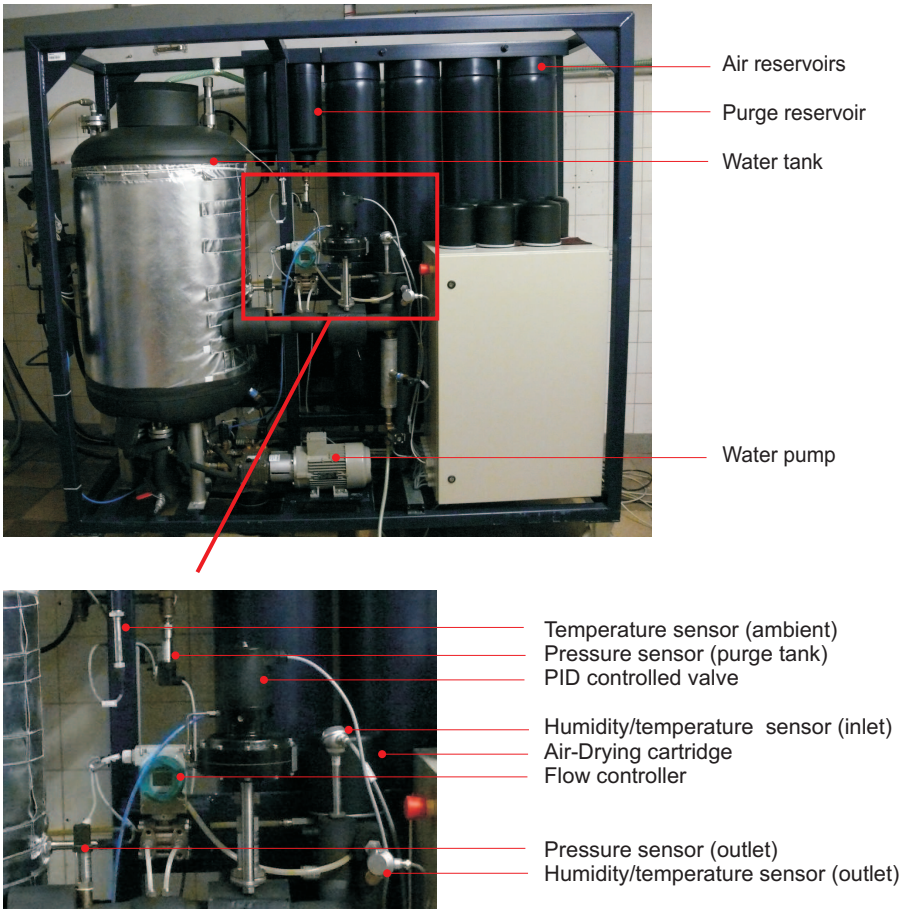

Figure 6.3.: Picture of the air drying test rig

6.1. Air drying with commercial samples

In order to establish a basis of comparison for the monolithic materials, commercially available samples were tested first. These included silica gel and zeolite NaA from *Grace Davison* and $Cu_3(BTC)_2$ pellets from *BASF*. The cartridges were filled with 1.2 l of material and tested according to the procedure described above. The diagram in figure 6.4 shows the results of the test. The results of $Cu_3(BTC)_2$ are not included, as the cartridge could not enter the performance test. The dew point depression D_p never fell below 5 °C. Detailed discussion of the drying tests with pelleted $Cu_3(BTC)_2$ is presented in the following section, since they resemble the results for the $Cu_3(BTC)_2$ monolithic sample.

In the diagram, both the dew point depression D_p and the humidity at the outlet of the cartridge are plotted against the cycle volume. As the cycle time was increased by 10 seconds after every two hours, the cycle volume steadily increased by approximately

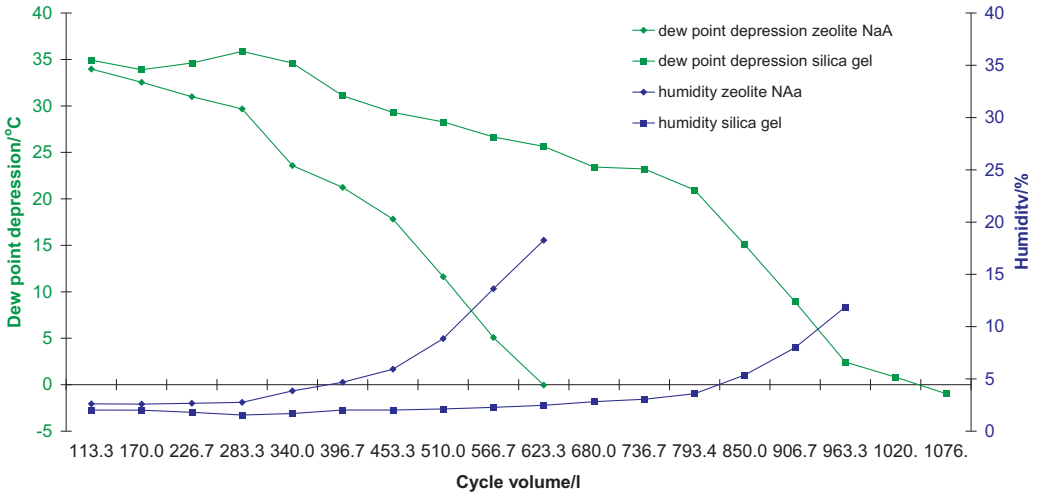

Figure 6.4.: Results of the test rig experiment with silica gel and zeolite NaA commercial samples.

113 l, which intensified the conditions. The ideal behavior is expected to show a slightly decreasing curve, which indicates a continuously high dew point depression D_p.

The zeolite NaA cartridge showed a poorer performance than the silica gel cartridge. The dew point depression D_p falls below the 5 °C limit after the tenth cycle. The silica gel cartridge maintains its drying performance for six more cycles. The humidity values mirror these results. The zeolite NaA cartridge shows a breakthrough already after six cycles, whereas the silica gel keeps a low humidity until the thirteenth cycle has passed. Moreover, the level of humidity of the silica gel cartridge is in the beginning lower (2.02 °C) than the zeolite NaA cartridge (2.62 °C). If one knows the water adsorption isotherms of both materials, the outcome of the test procedure seems logical. As a fully saturated moist air stream is used for the drying test, the silica gel has an advantage over the zeolitic material. Drying performance of silica gel should increase at higher relative humidity. The zeolite shows best results for complete removal of humidity at lower humidity levels.

Summing up these results, the use of silica gel as desiccant is most suitable for the air drying cartridge. In the following section, the drying tests using $Cu_3(BTC)_2$ samples are discussed.

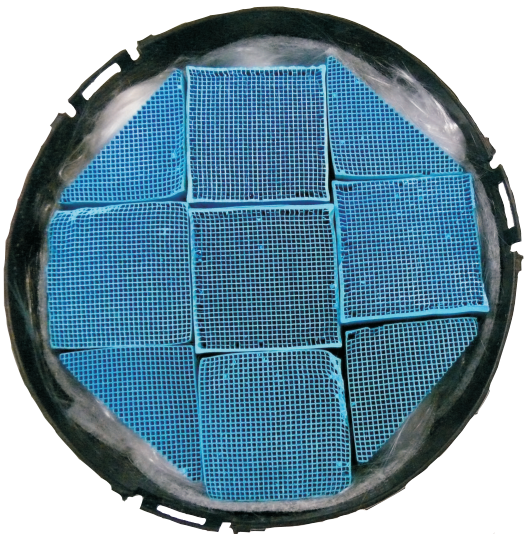

Figure 6.5.: Air drying cartridge with $Cu_3(BTC)_2$ monoliths.

6.2. Air drying with monolithic samples

In a second test series, the monolithic samples were tested with the same test procedure that is described in the foregoing section. The monoliths were cut in strands. A part of the samples had to be cut in half in order to make them fit into the cylindrical cartridge. The resulting voids were filled with glass wool. One example of a filled cartridge is shown in picture 6.5. The zeolitic monoliths were dried at 200 °C for 2 hours before they were mounted in the cylinder. $Cu_3(BTC)_2$ monoliths were dried at 150 °C.

The monolithic $Cu_3(BTC)_2$ sample cartridge could not pass the drying performance test. During the first phase that serves for conditioning of the cartridges, the pressure dew point did not exceed the 30 °C level, which is a requirement for the performance test to start. As there are no values available for the performance test, the humidity values of the conditioning phase are shown in figure 6.6. These were recorded at the outlet of the test cartridge. In the diagram, the humidity during the first 100 cycles of the test is plotted against the cycles of the regenerating phase. At the starting point of the test, the cartridge should have been saturated first in the saturation phase with 210 s cycles until the D_p is less than 5 °C. As the initial D_p values was already below 5 °C, the test automatically entered the regenerating phase. This indicates that the material did not dry the air stream sufficiently regarding the preset requirements. The only possibility to evaluate the drying behavior was to plot the data of the regenerating phase.

An initial sharp decrease in the very first cycles is noticeable (see figure 6.6). The humidity then levels off at approximately 20%. This value is certainly not logical and

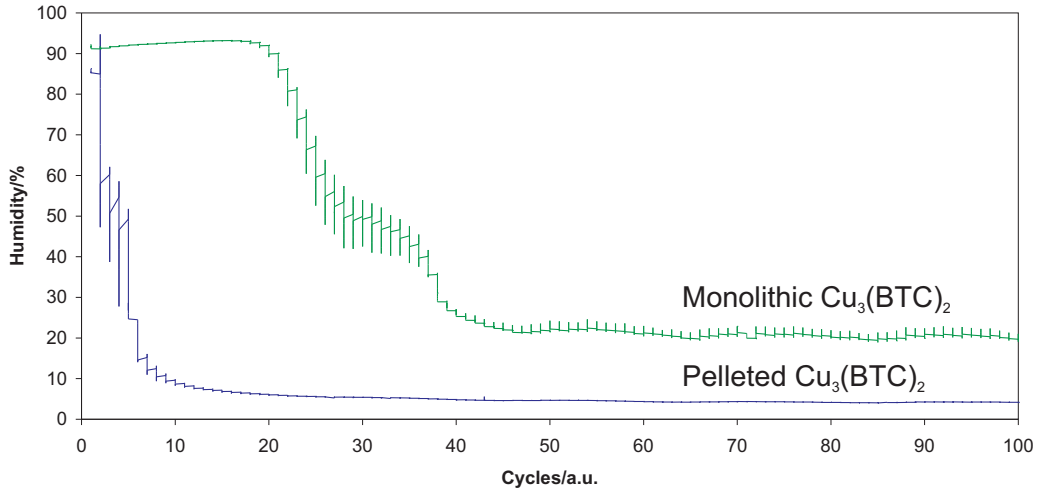

Figure 6.6.: Result of the test-rig experiment using $Cu_3(BTC)_2$ monoliths (green curve) and commercial $Cu_3(BTC)_2$ pellets (blue curve).

the curve has to be interpreted with care. Apparently, the material only dried the air in the beginning of the cycling until it was fully saturated. As more humid air approached, no more water was adsorbed leading to a condensation inside the cartridge. Hence, it was not possible to record 100% humidity at the outlet. When in contact with water, the material partly decomposes, as shown in chapter 5. The cartridge was opened afterwards and the monoliths were analyzed regarding specific surface area and powder XRD. The XRD pattern showed no remarkable change, but the specific surface area decreased to $154.90\,m^2g^{-1}$, which is less than 45% of the original value. The material decomposed when in contact with the humid air stream, which was confirmed by the decrease in specific surface area.

Like the cartridge with the monolithic $Cu_3(BTC)_2$ product, the $Cu_3(BTC)_2$ pelleted product could not enter the performance test. It showed a similar behavior to the monolithic sample. The results are also included in figure 6.6. The specific surface area decreased here to $167\,m^2g^{-1}$, which is less than 40% of the original value.

Surprisingly, even the cartridge with monolithic zeolite NaA could not pass the drying test. Figure 6.7 shows a similar result like the $Cu_3(BTC)_2$ monolithic samples. The performance test was not entered and the test was aborted in the saturation phase. Like the $Cu_3(BTC)_2$ monolith, the humidity first decreases sharply and then levels off at 20% humidity. The explanation is here also an insufficient drying behavior, which prohibited the initiation of the performance test. Zeolite NaA is stable towards water. There was no decrease of surface area after the test, the specific surface area amounted

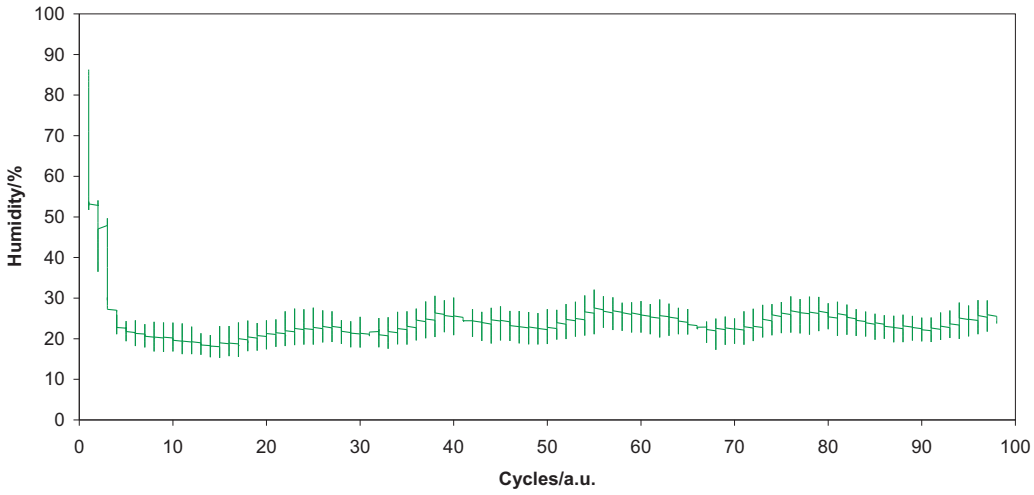

Figure 6.7.: Result of the test-rig experiment using zeolite NaA monoliths

to $564\,m^2g^{-1}$. Thus, another reason led to the outcome of the test. The commercial beaded product passed the performance test, which indicates that not only the type of material, but also the appropriate immobilization of the desiccant is crucial for a suitable drying performance. The adsorption isotherms that were presented in chapter 5.3 showed reasonable water adsorption capacity compared to the pelleted product. Contrarily, the kinetic tests showed a distinct difference between the powdered and the monolithic sample. The reason for the failure of the air drying test can only be due to an insufficient kinetic performance.

In summary, only the commercial zeolitic and silica gel products could pass the drying test. Both $Cu_3(BTC)_2$ samples and the zeolite NaA monoliths failed and could not even pass the first conditioning phase. $Cu_3(BTC)_2$ can be categorized as inappropriate for drying purposes. The investigations in the foregoing chapters already showed an insufficient stability towards water, which was only confirmed by the test rig experiments.

7. n-Heptane drying

Diesel fuel is one of several products that are obtained from the refining of crude oils. Crude oils are naturally generated complex mixtures of a multitude of hydrocarbon-type constituents [112]. In general, most of the crude oil products produced in a refinery is used as transportation and combustion fuels, among them gas fuels and liquid fuels. Gas fuels are refinery gas and liquefied petroleum gas (LPG). Refinery gas mostly consists of methane and ethane and is burnt as a fuel gas in the refinery itself. LPG is a mixture of propane and butane and is used both as a heating and motor fuel. Liquid fuels include among others gasoline, kerosene and gas oil. Usually, these products differ in their boiling ranges and therewith adapt to the required properties of the application.

Diesel fuel is obtained from the gas oil fraction of the refined crude oil. Gas oil consists of a light and heavy fraction in a boiling range between 200 and 350 °C. Predominantly, the gas oil is used as automotive diesel fuel. Compared to the Otto-engine, the diesel engine ignites the fuel without electrical ignition. The intake-air is strongly compressed leading to a rise in temperature that is sufficient to induce a self-ignition of the fuel in the cylinders [112]. The ignitability is the crucial factor that describes the willingness of the fuel to ignite in the hot, compressed intake-air of the engine. Generally, the paraffinic hydrocarbons possess the best ignitability, aromatic hydrocarbons the poorest. The ignitability of diesel fuel is characterized by the cetane number, a similar value to the octane number of gasoline.

The exact composition of diesel fuel is not easy to obtain. The distillation fraction of gas oils differs in composition depending on the crude oil. After refining, various additives like ignition improver, anti-foaming and cold flow additives are added to the fuel. Additionally, analysis is difficult and complex [113]. Standard diesel fuels are usually not characterized regarding hydrocarbon composition, but by properties like ash content, water content, sulfur content, flash point and cetane index. All these facts lead to the conclusion that an exact definition of the composition of diesel fuel is hardly possible. Merely a description can be considered as a useful characterization.

Taking all the afore mentioned points into consideration, diesel fuel can be regarded as a mixture mainly containing straight chained hydrocarbons with a chain length from

approximately C_7 to C_{18}, cyclic hydrocarbons, and aromatics with a content not exceeding 15 wt% [9]. Only the amount of aromatics or polyaromatics is well defined, as they contribute to NO_x and PM emission, respectively.

In the following chapter, the n-heptane drying behavior of the materials $Cu_3(BTC)_2$, zeolite NaA, zeolite X and silica gel was investigated at 25 and 80 °C. The purpose was to evaluate the suitability of the materials for diesel drying. The drying was recorded at two different temperatures, which should account for an adsorption and a desorption step. Adsorption should happen at the lower temperature (25 °C) until saturation is reached. When the material is flushed with a diesel fuel stream at elevated temperatures (80 °C), a part of the adsorbed water is desorbed due to the lower adsorption capacity at elevated temperatures. The larger the difference in drying capacity, the better the performance of the material. Additionally, the stability of the materials in n-heptane and diesel fuel was determined.

7.1. n-Heptane drying isotherms

As the analysis of water content in diesel fuel turned out to be imprecise and almost not reproducible with the available equipment, a long-chained and unbranched hydrocarbon was chosen as a comparable diesel fuel reference. n-Heptane was selected as a suitable medium, because it is easy to handle, non-toxic and relatively cheap compared to other long-chained hydrocarbons. Additionally, the solubility of water in n-heptane at ambient temperatures is much higher than for example for n-decane, which had probably been the most suitable reference substance for diesel fuel. n-Heptane also offers an sufficiently high boiling point with 99 °C, taking into consideration the measurements at elevated temperatures.

Moreover, all results regarding the drying of n-heptane can be interpreted not just as a simple model for the dewatering of diesel fuel, but simply as an investigation of drying a commonly used organic solvent. One might assume that there already exist a vast amount of data regarding n-heptane drying, but only few reports of n-heptane drying are available in literature [114, 115]. The only report that employs the Karl-Fischer coulometric titration as major analyzing technique was submitted by a Chinese group [114]. In this work, only one point of the isotherm was measured using a commercial beaded zeolite 4A material. Others report on the selective adsorption of water over organic solvents [116, 117].

Experimental

- Preparation
  n-Heptane drying isotherms were measured according to the following description: n-Heptane was dried above beaded zeolite 4A overnight. The remaining water content was checked twice by Karl-Fischer Titration (KFT) to confirm total dryness (water content ≤ 1). A 1000 ml double-necked round bottom flask was dried at 150 °C for several hours. After it was cooled down to room temperature in an desiccator, it was filled with 400 ml of the dried n-heptane and sealed immediately with a greased ground-in glass stopper (NS23) and a small silicon stopper (NS14). The flask was intensely shaken for about a minute. After several hours the water content was measured by KFT. The adsorbent was outgassed overnight in a 10 ml Schlenk tube. The outgas temperature for zeolitic samples was 200 °C, MOFs and silica gels were outgassed at 150 °C. The weight of the Schlenk tube was recorded. The Schlenk tube and the round-bottom flask were transferred to a poly propylene glove bag, which was purged with nitrogen and sealed properly to avoid any leakage or exchange with the atmosphere. Additionally, the glove bag was equipped with 200 ml of activated zeolite 4A in beaded form. After 24 hours, the flask was opened and a part of the activated adsorbent was transferred to the flask. The flask was sealed again and taken out. The Schlenk tube was weighed again to calculate the amount of adsorbent in the flask. The flask was tempered in a water bath (25 or 80 °C).

- Measurement
  After 24 hours, the water content was measured by KFT. A 10 ml single-use syringe was used to withdraw at least 6 ml of n-heptane. Prior to sample taking, the syringe was rinsed with approximately 10 ml of sample from the flask. The water content was measured by KFT and all sample weight withdrawn from the flask were recorded.

- Dosage
  A specific amount (roughly 20 ml) of moist n-heptane was added through the septum to the flask. The usual water concentration of n-heptane was about 40 ppm and always analyzed prior to dosage. The flask was then carefully swayed to obtain a mixing of the n-heptane. After 18-24 hours the water content was analyzed again and a new volume of moist n-heptane was dosed to the flask.

- Evaluation of the data
  A typical data sheet is shown in table 7.1. The differences in water content are calculated and expressed as the adsorbed amount of water. Therewith, the connection of equilibrated water content (x-axis) and adsorbed amount in weight percentage can be plotted in a diagram. The isotherm provides information about the total adsorbed amount or the drying capacity as well as the pore structure if one considers the shape of the curve.

Sources of error and relative standard deviation

The reproducibility of results that were obtained from the same sample is strongly depended on both the water content and the volume of analyzed sample. Naturally, the repeatability as well as the accuracy becomes better the higher the volume of analyzed sample. The relative standard deviation (S_{rel}) decreases with increasing sample weight. For samples with water concentrations of about 40 ppm, S_{rel} averages 1.2 % assuming the use of 5 g of sample [118]. In order to decrease S_{rel}, a high weight of sample was chosen. Moreover, the abort criteria for analysis were carefully chosen. After the endpoint was detected, the titration was continued for another 120 seconds. These settings led to reproducible results even in the lower ppm region. In some cases, when the sample was exceptionally dry, the obtained result was slightly negative (-0.01 to -0.8). This was the result of the low drift value, which was often alternating between zero and one. The drift values are averaged at the end of the analysis and subtracted from the total value, which can sometimes lead to negative numbers. In these cases, the result was assumed to be zero. Analysis of samples that were used in 80 °C isotherms were even more challenging. As the electric conductivity is dependent on temperature, the sample had to be cooled down to ambient temperature prior to analysis. Ideally, the samples should have had the same temperature. As the ambient temperature varied a few degrees over the whole period of work, this condition was not given and has to be taken into account when interpreting the data.

Presentation of data

In the following, the measured data are presented in a single diagram. Although all materials were analyzed several times with the same method, plotting all data in the

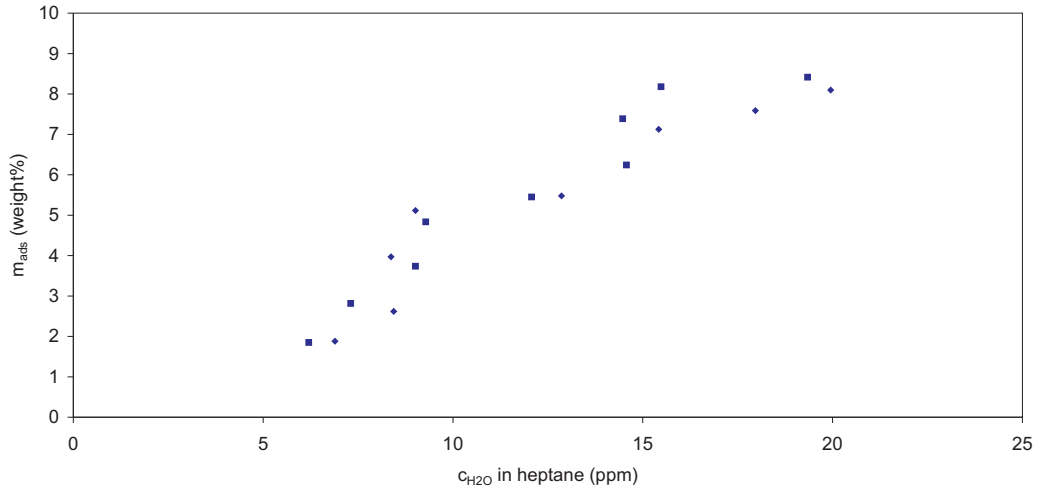

Figure 7.1.: n-Heptane drying isotherms of $Cu_3(BTC)_2$ measured at 25 °C.

same diagram is the most reasonable way. The single measurements always showed the same course, but complete superimposal was not possible. On the one hand, this is due to the sensitive measuring technique and on the other hand to the sources of error that were already discussed above.

7.1.1. Drying isotherms of $Cu_3(BTC)_2$

$Cu_3(BTC)_2$ shows in the drying experiment of n-heptane an isotherm comparable to the water adsorption isotherm. The experimental conditions did not allow the recording of the drying in the really low concentration ranges, since the initial water concentration of the n-heptane samples was never zero. After the adsorbent was added to the n-heptane sample, no dosage of moist n-heptane was therefore needed. The first dose was then relatively high.

The n-heptane drying isotherm of $Cu_3(BTC)_2$ at 25 °C is presented in figure 7.1. The isotherm starts at a moisture content of about five ppm of water with an adsorbed amount of almost 2 wt%. It was assumed that this first adsorption step is caused by the coordination of water to the copper centers. The isotherm than exhibits two additional steps of adsorption at about 8 and 15 ppm. In both cases, the increase in adsorption of water can be attributed to the pore filling of the smaller and larger cage, like in the water adsorption experiment.

The first step adds up to an adsorbed amount of approximately 5 wt%, the second step adds up to about 8.3 wt%. Considering the size of the cages of $Cu_3(BTC)_2$, the smaller pore should be filled first. Despite this fact, the hydrophilicity of the pore is here more important leading to the filling of the bigger and more hydrophilic pore like in the water adsorption experiment. As the total adsorbed amount for the first adsorption step is larger than for the second one, this clearly pictures the filling of the larger 9 Å-pore.

Evidently, the two adsorption steps in the n-heptane drying isotherm are not as pronounced as in the water adsorption experiment. The drying isotherms could not be completely superimposed. Still, the result was reproducible and the outcome was always of the two-step shape. The measuring technique surely cannot compete with the gas adsorption experiments performed with fully-automated equipment. Sources of error are here much more at hand. These include weighing errors of the adsorbent, the n-heptane sample and finally the Karl-Fischer method itself.

Nonetheless, the experiment provides a glance at the adsorption behavior of the material in a liquid environment. The fact that the outcome of the experiment closely resembles the water adsorption isotherms argues for the reliability of the present results. Eventually, the method itself clearly can be improved by automating some of the experimental steps or the preparation of the n-heptane samples. However, down to the present day, no automated equipment is known to be available on the market.

The recording of n-heptane drying isotherms at elevated temperatures shows a similar two-step adsorption process. Figure 7.2 shows the drying isotherm of $Cu_3(BTC)_2$ at 80 °C. The total adsorbed amount is significantly lower with 1.8 wt% for the first adsorption step and 3.5 wt% for the second step. It is therewith in accordance with the results of the water adsorption isotherms. Compared to the lower temperature measurement, the adsorption was shifted to lower ppm values, which accounts for a better drying performance at elevated temperatures.

Point	V_{Sample} [ml]	c_{Sample} [ppm]	$V_{Analysis}$ [ml]	$V_{1Sample}$ [ml]	$m_{H_2O\ added}$ [mg]	$m_{H_2O\ adsorbed}$ [wt%]	t_{equil} [h]
0	400	8.3	23	377	0	2.31	24
1	377	0	18	359	1.01	3.06	78
2	381	0	19	362	2.16	4.53	24
3	404	0.4	26	378	0.7	5.19	24
4	400	0	28	372	0.93	5.73	22
5	393	0.5	20	373	0.97	6.42	19
6	394	0.6	25	369	1.12	7.33	24
7	390	0.3	21	369	0.93	6.07	23
8	390	7.1	19	371	1.03	5.76	26
9	392	11.0	20	372	0	5.76	24

Table 7.1.: V_{Sample} - volume of the total *n*-heptane
c_{Sample} - water content of V_{Sample}
$V_{Analysis}$ - volume withdrawn for Karl-Fischer analysis
$V_{1Sample}$ - new volume of the total *n*-heptane
$m_{H_2O\ added}$ - amount of H_2O added to the *n*-heptane in mg
$m_{H_2O\ adsorbed}$ - amount of adsorbed water expressed in wt%

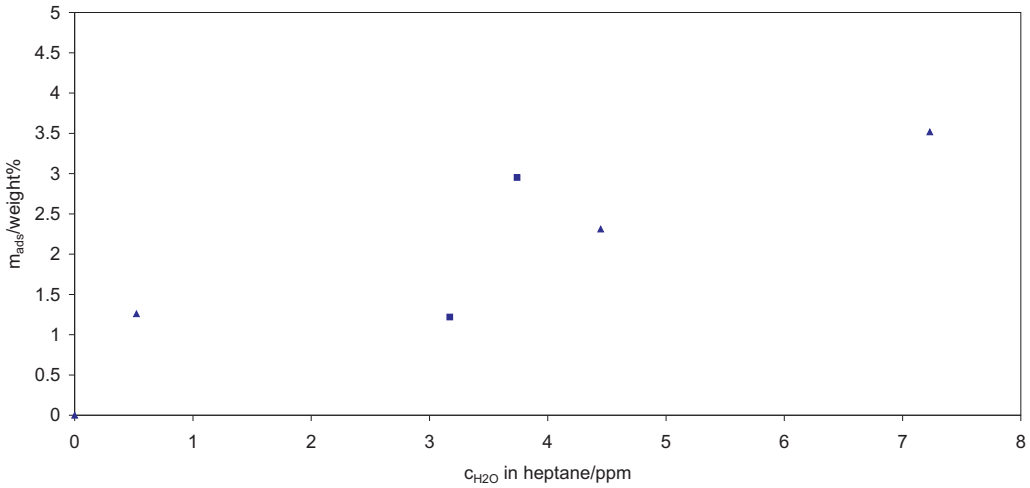

Figure 7.2.: n-Heptane drying isotherm of $Cu_3(BTC)_2$ measured at 80 °C.

7.1.2. Drying isotherms of zeolitic samples

Drying isotherms of zeolite NaA

Zeolite 4A shows a similar behavior in the n-heptane drying experiment as in the water adsorption isotherms. The course of the isotherm is of a typical *type I* shape, shown in figure 7.3. Zeolite 4A with its 4 Å-pores should exclusively adsorb the water molecules in the n-heptane sample, as n-heptane is too large to fit into 4 Å pores (kinetic diameter 4.3 Å). A drying efficiency close to 100% or down to 1 ppm is therewith possible until the material is fully saturated. When fully saturated with water, the isotherm reaches a saturation plateau at about 5 wt% adsorbed water. Compared to $Cu_3(BTC)_2$, the *type I* behavior of zeolite NaA is more suitable for drying.

Adsorption at 80 °C decreases the total adsorption capacity to averaged 2 wt%. Hence, the decrease compared to the 25 °C measurement is 3 wt%. For the use in a thermal swing adsorption cycle, the difference in capacity might be too low for an economic use.

The drying isotherms of zeolite X

Zeolite X has bigger pores than the NaA type with 13 Å in diameter. The total water adsorption capacity is therewith higher. The plotted data in figure 7.5 show an adsorbed value of about 13 wt% in the region below 5 ppm. The capacity exceeds 18 wt% in the region 20-25 ppm. The shape can be compared with *type I* course in a nitrogen physisorption measurement. Zeolite X is a appropriate material for drying in the trace

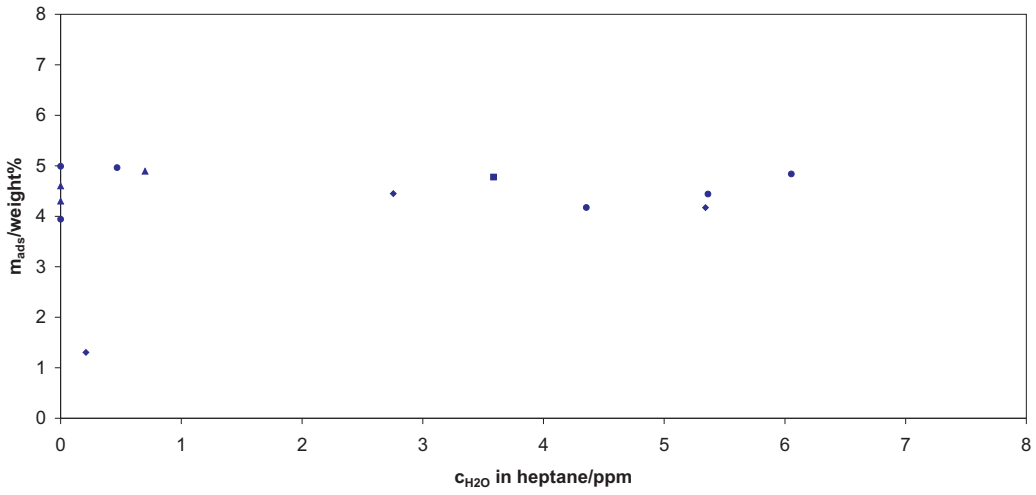

Figure 7.3.: n-Heptane drying isotherm of zeolite NaA at 25 °C.

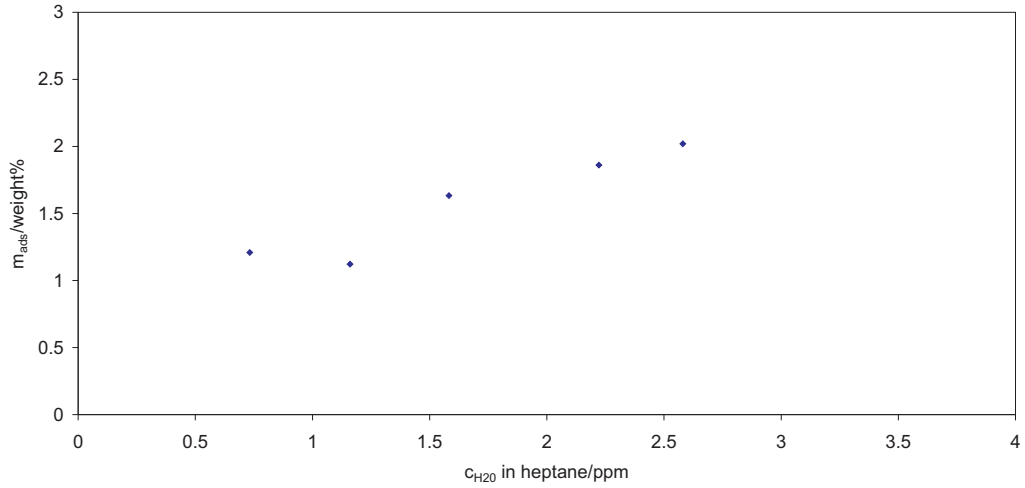

Figure 7.4.: n-Heptane drying isotherm of zeolite NaA at 80 °C.

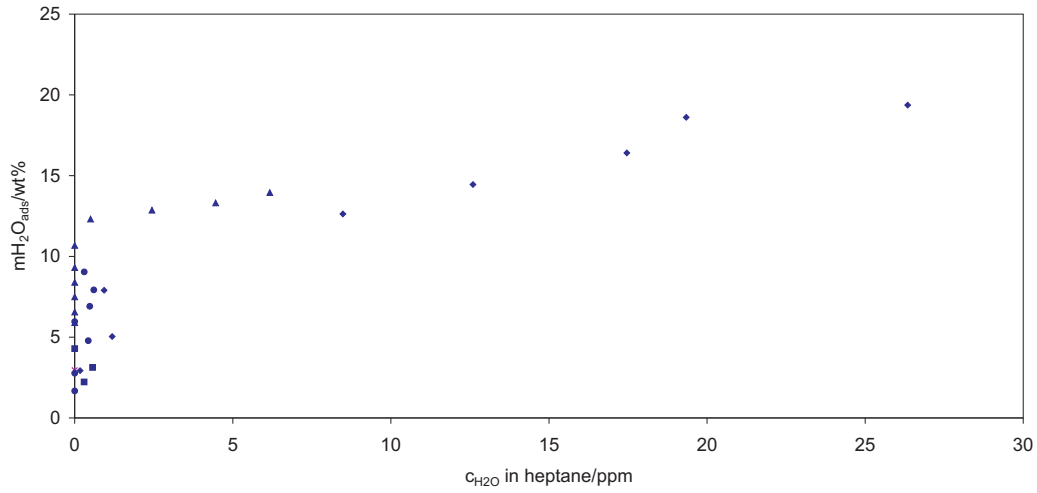

Figure 7.5.: *n*-Heptane drying isotherm of zeolite X at 25 °C.

area, since it adsorbs water from *n*-heptane at lowest water concentrations from 1 to 2 ppm. All measured isotherms showed an increase in the higher ppm region rather than saturation, which is also observable in the present diagram.

A common observation in all experiments was a steep increase of adsorbed amount in the higher ppm-regions. These values were unreasonably high and could not be explained in terms of adsorption. They were therefore neglected in the data evaluation. The occurrence for the excessive increase might arise when the adsorbent is saturated with water and the further added water accumulates at the hydrophilic powder. It is not adsorbed, but cannot be detected by the titration anymore and the adsorbed amount seems to increase unnaturally strong.

At 80 °C, the total adsorption capacity of zeolite X falls to 3.8 wt%, which can be seen in figure 7.6. The shape of the data is still of the *type I* behavior with a sharp rise between 0 and 0.5 ppm followed by a saturation plateau. The difference in adsorbed amount at 25 and 80 °C amounts to 7.2 wt%, which is much higher than for NaA zeolite. Zeolite X is supposedly suitable for liquid drying in terms of a thermal swing cycle. The material could dry the liquid stream at moderate temperatures. Close to saturation, the cartridge could be flushed with the hot diesel fuel stream coming from the injection system. Part of the water would be desorbed and led back to the tank. The results show that the higher the temperature gradient of the system the better the yield regarding the efficiency.

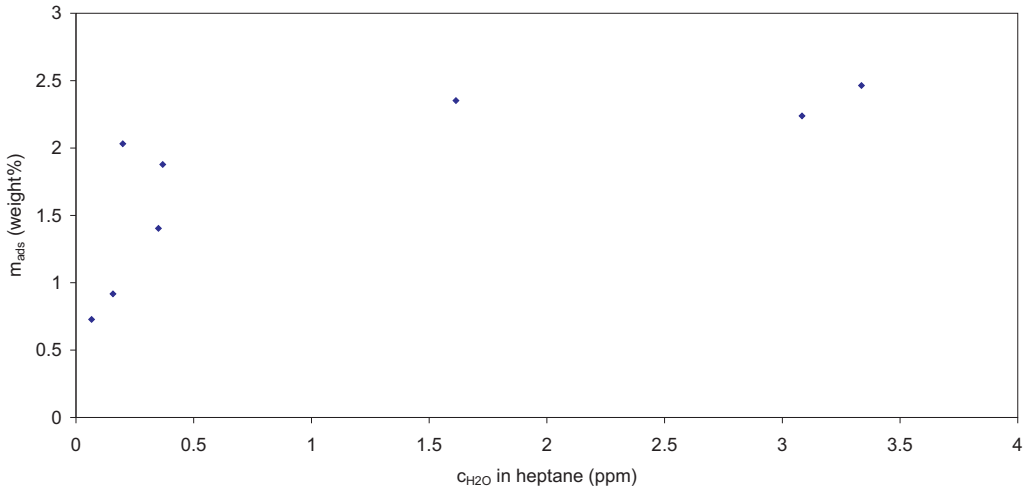

Figure 7.6.: n-Heptane drying isotherm of zeolite X at 80 °C.

7.1.3. Drying isotherms of silica gel

Silica gel shows similar behavior in the drying isotherm compared to the gas adsorption experiments. The course of the isotherm is linear in the beginning and levels off in a saturation plateau, see figure 7.7. Below 10 ppm, only 2 wt% of water is adsorbed. The adsorbed amount reaches a maximum of about 5.8 wt% at 30 ppm. Like for the other materials, the isotherm exhibited a sharp rise in the higher ppm regions, which did not seem to be reasonable. These values were excluded from the diagram. Apparently, the water accumulated at the surface of the powder after the material was fully saturated. An increase in water concentration could therefore not be detected, which resulted in a steep increase of the isotherm. Compared to the zeolitic materials, silica gel is like $Cu_3(BTC)_2$ not suitable for the drying in the trace area. The total capacity is similar to NaA zeolite. As silica gel turned out to be unusable for the trace water drying of n-heptane, no measurements at elevated temperatures were performed.

7.2. n-Heptane and diesel fuel stability

Like for water adsorption in gaseous phases, the diesel fuel desiccant needs to maintain its stability and adsorption properties during use. Degradation of the framework and a resulting reduced performance is not desirable. In order to assess the stability of the different adsorbents, the specific surface area was measured after the recording of the n-heptane drying isotherms. Additionally, the materials were stored in diesel fuel and

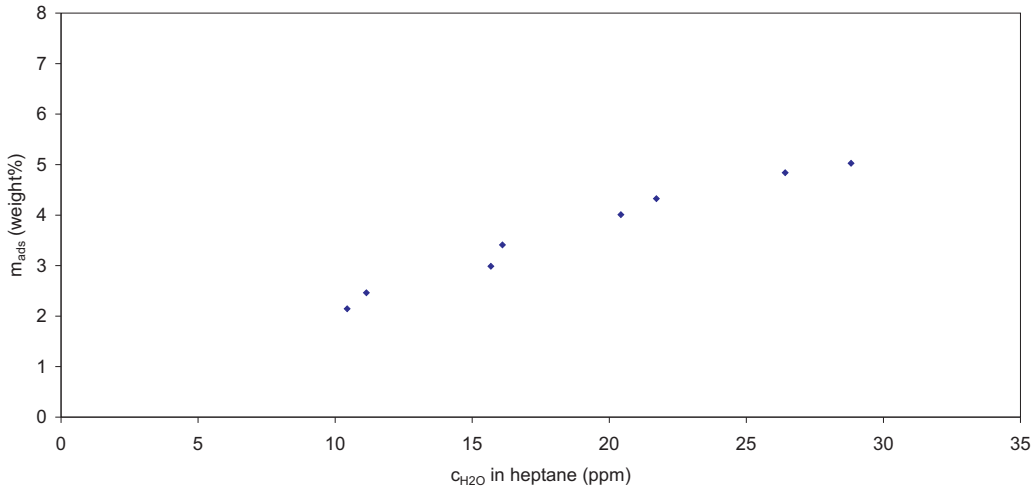

Figure 7.7.: n-Heptane drying isotherm of silica gel at 25 °C.

water at ambient conditions and also analyzed regarding specific surface area. As not all materials turned out to be suitable for drying purposes, only the zeolitic materials and $Cu_3(BTC)_2$ were investigated.

Experimental

$Cu_3(BTC)_2$, zeolite NaA and zeolite X were stored in water and diesel fuel at ambient conditions. After nine months the samples were filtered and washed with ethanol. The samples were dried at 80 °C for 10 minutes. This procedure was repeated three times to ensure complete removal of diesel. $Cu_3(BTC)_2$, zeolite NaA and zeolite X samples that were used for the recording of the n-heptane drying isotherms were filtered and briefly dried in air.

n-Heptane and diesel stability

Table 7.2 lists the results of the experimental series. The zeolitic materials are both completely stable towards diesel, n-heptane and water. $Cu_3(BTC)_2$ shows like for water a certain instability with a decrease of more than 50 %. The values for the drying samples are a bit better with loss of surface area about 20 % for the 25 °C measurement and 30 % for the 80 °C measurement. In summary, the stability of $Cu_3(BTC)_2$ is insufficient for the drying of both n-heptane and diesel.

Material	S_a $[m^2g^{-1}]$
$Cu_3(BTC)_2$ as made*	1509
$Cu_3(BTC)_2$ in water*	0
$Cu_3(BTC)_2$ in diesel*	647
$Cu_3(BTC)_2$ after n-heptane drying at 25 °C*	1203
$Cu_3(BTC)_2$ after n-heptane drying at 80 °C*	1091
Zeolite NaA as made**	639
Zeolite NaA in water**	629
Zeolite NaA in diesel**	584
Zeolite NaA after n-heptane drying at 25 °C**	599
Zeolite NaA after n-heptane drying at 80 °C**	574
Zeolite X as made*	638
Zeolite X in water*	668
Zeolite X in diesel*	661
Zeolite X after n-heptane drying at 25 °C*	644
Zeolite X after n-heptane drying at 80 °C*	631

Table 7.2.: Specific surface areas of $Cu_3(BTC)_2$, zeolite NaA and zeolite X.
*Single point BET surface area calculated at $p/p_0 = 0.3$ from nitrogen physisorption at 77 K
**Single point BET surface area calculated at $p/p_0 = 0.3$ from water adsorption at 298 K.

8. Summary and conclusion

In the present work, MOF materials were investigated regarding their water adsorption and desorption behavior. The basis for these investigations was the possible use of new MOF materials for drying of compressed air streams and diesel fuel or *n*-heptane, respectively. Additionally, different approaches to immobilize $Cu_3(BTC)_2$ were presented. These included the manufacturing of monoliths made of $Cu_3(BTC)_2$ and zeolite NaA. Their drying performance was evaluated on an air drying test rig. *n*-Heptane drying isotherms of the materials $Cu_3(BTC)_2$, zeolite NaA and X, and silica gel are presented in the last part of this work.

In order to evaluate the drying performance of $Cu_3(BTC)_2$ in the test rig experiment, a suitable immobilization of $Cu_3(BTC)_2$ had to be developed. The chosen possibilities included the deposition of $Cu_3(BTC)_2$ on cordierite monoliths as well as the manufacturing of honeycomb $Cu_3(BTC)_2$ monoliths. As an alternative, the formation of $Cu_3(BTC)_2$ paper sheets and the crystal growth of $Cu_3(BTC)_2$ on pulp fibers were performed.
The in-situ synthesis on cordierite monoliths was unsatisfying. Crystal growth was scarce and deposition occurred only at the cutting edges of the ceramic. XRD patterns could not confirm the presence of $Cu_3(BTC)_2$ and the specific surface area was around $50\,m^2g^{-1}$. Different approaches including pre-treatment of the samples and varying synthetic procedures did not improve the results. In contrast, the manufacturing of $Cu_3(BTC)_2$ monolith with siloxane ether and methyl cellulose as plasticizer and binding agent resulted in mechanically stable monolithic structures with surface areas up to $480\,m^2g^{-1}$. As a reference for further experiments, NaA zeolite monolithic samples were also prepared.
Another possibility to immobilize the materials was the formation of paper sheets. The resulting papers showed an inhomogeneous distribution of powder and it was therefore difficult to determine both the content of $Cu_3(BTC)_2$ powder in the paper and its specific inner surface area. It was decided to move over to an in-situ synthesis of $Cu_3(BTC)_2$ on pulp fibers. Different pulp qualities were chosen for the experiments. The outcomes were samples with surface areas ranging from almost zero to more than $300\,m^2g^{-1}$. The

distribution of the crystals over the fibers was here rather homogeneous. The lignin residue of the pulp fibers was the determining factor for the success of the deposition.

The water adsorption properties of the materials $Cu_3(BTC)_2$, ZIF-8, MIL-100(Fe) and MIL-101 as well as the zeolites NaA, X and silica gel were presented.
In summary, the MOF materials turned out to be unsuitable for drying purposes. ZIF-8 is highly hydrophobic and showed almost no affinity towards water. This high hydrophobicity causes an exceptional chemical stability towards water. The MIL materials do adsorb water, but only at relative pressures from $p/p_0 = 0.5$, which is not sufficient in terms of drying. Still, they are also highly stable towards water. $Cu_3(BTC)_2$ shows the best water adsorption behavior, but total stability towards water is not given.
As $Cu_3(BTC)_2$ was the most interesting of the selected MOFs, the water adsorption properties were investigated further, both in test rig experiments for air drying cartridges for compressed air braking systems and *n*-heptane drying isotherms.
The monolithic samples made of $Cu_3(BTC)_2$ and zeolite NaA prepared in this work were also analyzed. These could definitely compete with commercial beaded samples regarding the static experiments. The kinetic performance of the $Cu_3(BTC)_2$ monolith exceeded the zeolite NaA monolith.

After the preparation of samples, the materials were evaluated on an air drying test rig regarding their drying performance. This test procedure is used for the evaluation of drying cartridges, which are part of a compressed air braking system in heavy and medium duty vehicles. The air drying cartridge ensures the removal of moisture before the compressed air enters the braking systems. For these test series, samples with commercial beaded zeolite NaA, silica gel, $Cu_3(BTC)_2$ and the monolithic zeolite NaA and $Cu_3(BTC)_2$ monolith were prototyped.
The $Cu_3(BTC)_2$ samples did not enter the performance test due to insufficient drying performance. The failure of the test is the result of the incomplete water stability of $Cu_3(BTC)_2$. The zeolite NaA monolith could also not enter the test. In this case, the problem can be attributed to the molding of the material, which did not yield a satisfying kinetic performance.

The *n*-heptane drying isotherms of the materials $Cu_3(BTC)_2$, zeolite NaA, zeolite X and silica gel was performed employing Karl Fischer coulometric titration. *n*-heptane

was chosen as a reference for diesel fuel. In a possible application, one of the materials should be used for the drying of trace water in diesel fuel after a diesel filter with automatic water disposal. In the system, the adsorbent should adsorb the water at low temperatures. The regeneration could be introduced by flushing the material with the dried diesel fuel at higher temperatures.

The most appropriate material for drying is zeolite X. The difference in adsorbed amount at two different temperatures (25 and 80 °C) was the highest. Additionally, the water is adsorbed at low concentrations. Zeolite NaA showed the same behavior, but the difference in adsorption capacity was less pronounced. $Cu_3(BTC)_2$ and silica gel are less suitable, since the drying takes place at higher concentrations of water. Moreover, $Cu_3(BTC)_2$ slowly decomposes when in contact with *n*-heptane or diesel fuel, whereas the zeolite materials show complete stability in both media.

Bibliography

[1] E. Dickson, J. Ryan, M. Smulyan, *The Hydrogen Energy Economy: A realistic Appraisal of Prospects and Impacts*, **1977**, New York, Praeger

[2] D. Bruhn, D. Danner, L. Endruschat, P. Gerigk, C. Girnus, J. Göbert, H. Gross, D. Kruse, C. Rasmussen, R. Schopf, R. Volkheimer, *Kraftfahrzeugtechnik*, **2005**, Westermann

[3] M. Uchino, M. Nakanu, U.S. Patent 6.503.301 B2, *Fuel Vapour Treatment Cannister*, **2000**, Tokyo, Tennex Corporation

[4] A. Blackwood, *SAE Tech. Paper Series*, **2004**, *2004-01-2631*

[5] D. Ruthven, S. Farooq, K. Knaebel, *Pressure Swing Adsorption*, **1994**, Weinheim, VCH

[6] C. Skarstrom, U.S. Patent 2.944.627, *Method and Apparatus for Fractionating gaseous Mixtures by Adsorption*, **1958**, Esso Research and Engineering Company

[7] P. Guerin de Montgareuil, D. Dominé, U.S. Patent 3.155.4668, *Process for Separating a Binary Gaseous Mixture by Adsorption*, **1964**, L'Air Liquide Société Anonyme pour L'Etude et L'Exploitation des Procédes George Claude, Paris

[8] DIN EN 590, *Diesel Fuel - Requirements and Test Methods*, **2004**

[9] European Automobile Manufacturers Association, *World Wide Fuel Charter*, **2000**, ACEA, Bruxelles

[10] M. Gänswein, P. Koppi, P. Küsgens, S. Siegle, WO 2008/023029 A2, *Fuel Filter*, **2008**, MAHLE International GmbH

[11] M. Gänswein, *Automobiltechn. Zeitschr.*, **2008**, 9, 780

[12] B. Elvers, *Handbook of Fuels*, **2008**, Weinheim, Wiley-VCH

[13] L. McCusker, F. Liebau, G. Engelhardt, *Pure Appl. Chem.*, **2001**, *73*, 381

[14] Z.-Y. Yuan, B. Su, *J. Mater. Chem.*, **2006**, *16*, 663

[15] C. Kresge, L. Leonowicz, W. Roth, J. Vartuli, J. Beck, *Nature*, **1992**, *359*, 710

[16] J. Weitkamp, *Solid State Ion.*, **2000**, *131*, 175

[17] V. Menon, S. Komarneni, *J. Porous. Mater.*, **1998**, *5*, 43

[18] P. Krawiec, M. Kramer, M. Sabo, R. Kunschke, H. Fröde, S. Kaskel, *Adv. Eng. Mater.*, **2006**, *8*, 293

[19] I. Senkovska, S. Kaskel, *Micropor. Mesopor. Mater.*, **2008**, *112*, 108

[20] A. Dillon, M. Heben, *Appl. Phys. A*, **2001**, *72*, 133

[21] J. Rowsell, A. Millward, K. Park, O. Yaghi, *J. Am. Chem. Soc.*, **2004**, *126*, 5666

[22] S. Kaskel, F. Schüth, K. Sing, J. Weitkamp, *Handbook of Porous Solids*, **2002**, Weinheim, Wiley VCH

[23] S. Kitagawa, R. Kitaura, S. Noro, *Angew. Chem.*, **2004**, *116*, 2388

[24] O. Yaghi, H. Li, C. Davis, D. Richardson, T. Groy, *Acc. Chem. Res.*, **1998**, *31*, 474

[25] M. Eddaoudi, J. Kim, N. Rosi, D. Vodak, J. Wächter, M. O'Keeffe, O. Yaghi, *Science*, **2002**, *295*, 469

[26] B. Hoskins, R. Robson, *J. Am. Chem. Soc.*, **1989**, *111*, 5962

[27] H. Li, M. Eddaoudi, M. O'Keeffe, O. Yaghi, *Nature*, **1999**, *402*, 276

[28] O. Yaghi, M. O'Keeffe, N. Ockwig, H. Chae, M. Eddaoudi, J. Kim, *Nature*, **2003**, *423*, 705

[29] M. Eddaoudi, D. Moler, H. Li, T. Reineke, M. O'Keeffe, O. Yaghi, *Acc. Chem. Res.*, **2001**, *34*, 319

[30] A. Cheetham, G. Férey, T. Loiseau, *Angew. Chem. Int. Ed.*, **1999**, *38*, 3268

[31] G. Desiraju, *Nature*, **2001**, *412*, 397

[32] B. Panella, *"Hydrogen Storage by Physisorption on Porous Materials"*, Thesis, **2006**

[33] J. Rowsell, O. Yaghi, *Angew. Chem.*, **2005**, *117*, 4748

[34] H. Furukawa, M. Miller, O. Yaghi, *J. Mater. Chem.*, **2007**, *17*, 3197

[35] A. Millward, O. Yaghi, *J. Am. Chem. Soc.*, **2005**, *127*, 17998

[36] R. Banerjee, A. Phan, B. Wang, C. Knobler, H. Furukawa, M. O'Keeffe, O. Yaghi, *Science*, **2008**, *319*, 939

[37] B. Wang, A. Coté, H. Furukawa, M. O'Keeffe, O. Yaghi, *Nature*, **2008**, *453*, 207

[38] R.-Q. Zou, H. Sakurai, Q. Xu, *Angew. Chem. Int. Ed.*, **2006**, *45*, 2542

[39] J. Seo, D. Wang, H. Lee, S. Jun, J. Oh, Y. Jeon, K. Kim, *Nature*, **2000**, *404*, 982

[40] K. Schlichte, T. Kratzke, S. Kaskel, *Micropor. Mesopor. Mater.*, **2004**, *73*, 81

[41] C. Wu, A. Hu, L. Zhang, W. Lin, *J. Am. Chem. Soc.*, **2005**, *127*, 8940

[42] L. Alaerts, C. Kirschhock, M. Maes, M. van den Veen, V. Finsey, A. Depla, J. Martens, G. Baron, P. Jacobs, J. Denayer, D. De Vos, *Angew. Chem.*, **2007**, *119*, 4371-4375

[43] R. Morris, P. Wheatley, *Angew. Chem. Int. Ed.*, **2008**, *47*, 4966

[44] P. Horcajada, C. Serre, G. Maurin, M. Ramsahye, F. Balas, M. Vallet-Regi, M. Seban, F. Taulelle, G. Férey, *J. Am. Chem. Soc.*, **2008**, *130*, 6774

[45] U. Müller, M. Schubert, F. Teich, H. Puetter, K. Schierle-Arndt, J. Pastré, *J. Mater. Chem.*, **2005**, *16*, 626

[46] S. Chui, S. Lo, J. Charmant, A. Orpen, I. Williams, *Science*, **1999**, *283*, 1148

[47] G. Férey, C. Mellot-Draznieks, C. Serre, F. Millange, *Acc. Chem. Res.*, **2004**, *38*, 217

[48] A. Henschel, K. Gedrich, R. Kraehnert, S. Kaskel, *Chem. Comm.*, **2008**, *35*, 4192

[49] G. Férey, C. Mellot-Draznieks, C. Serre, F. Millange, J. Dutour, S. Surblé, I. Margiolaki, *Science*, **2005**, *309*, 2040

[50] G. Férey, C. Serre, C. Mellot-Draznieks, F. Millange, S. Surblé, J. Dutour, I. Margiolaki, *Angew. Chem. Int. Ed.*, **2004**, *43*, 6296

[51] Y. Liu, V. Kravtsov, R. Lasena, M. Eddaoudi, *Chem. Comm.*, **2006**, 1488

[52] H. Wu, W. Zhou, T. Yildrim, *J. Am. Chem. Soc.*, **2007**, *129*, 5314

[53] C. Baerlocher, W. Meier, D. Holson, *Atlas of Zeolite Framework Types*, **2001**, Amsterdam, Elsevier

[54] W. Löwenstein, *Am. Mineralogist*, **1954**, *39*, 92

[55] R. Tschernich, *Zeolites of the World*, **1992**, Phoenix, Geoscience Press

[56] R. Barrer, *Hydrothermal Chemistry of Zeolites*, **1982**, Academic Press, London

[57] D. Breck, *Zeolites Molecular Sieves*, **1974**, Wiley, New York

[58] J. Newsam, *Solid State Chemistry : Compounds*, **1992**, Oxford University Press, New York

[59] D. Breck, W. Eversole, R. Milton, T. Reed, T. Thomas, *J. Am. Chem. Soc.*, **1956**, *78*, 5963

[60] R. Milton, U.S. Patent 2.822.244, *Molecular Sieve Adsorbents*, **1959**, Union Carbide Corporation, New York

[61] B. Lok, C. Messina, R. Patton, R. Gajek, T. Cannan, E. Flannigen, *J. Am. Chem. Soc.*, **1984**, *106*, 9062

[62] R. Wadlinger, E. Rosinski, C. Plank, U.S. Patent 3 375 205, *Synthetic Zeolite*, **1968**, Mobil Oil Corporation, New York

[63] T. Graham, *Philos. Trans. R. Soc. London*, **1861**, *252*, 204

[64] W. Patrick, U.S. Patent 1.29.724, *Silica Gel and the Process of Making the Same*, **1919**, W.R. Grace Co.-Conn, Baltimore

[65] R. Iler, *The Chemistry of Silica*, **1979**, New York, John Wiley & Sons

[66] F. Roquerol, J. Roquerol, K. Sing, *Adsorption by Powders and Porous Solids*, **1998**, Academic Press, San Diego

[67] K. Sing, D. Everett, R. Haul, L. Moscou, R. Pierotti, J. Roquerol, T. Siemienieska, *Pure Appl. Chem.*, **1985**, *57*, 603

[68] I. Langmuir, *J. Am. Chem. Soc.*, **1916**, *38*, 2221

[69] I. Langmuir, *J. Am. Chem. Soc.*, **1918**, *40*, 1361

[70] S. Brunauer, S. Emmet, E. Teller, *J. Am. Chem. Soc.*, **1938**, *60*, 309

[71] R. Bunsen, *Liebigs Ann. Chem.*, **1853**, *86*, 265

[72] K. Fischer, *Angew. Chem.*, **1935**, *48*, 394

[73] J. Verhoff, E. Barendrecht, *J. Electroanal. Chem.*, **1976**, *71*, 305

[74] E. Scholz, *Fresenius Z. Anal. Chem.*, **1980**, *306*, 394

[75] E. Scholz, *Fresenius Z. Anal. Chem.*, **1982**, *312*, 460

[76] D. Zacher, A. Baunemann, S. Hermes, R. Fischer, *J. Mater. Chem.*, **2007**, *17*, 2785

[77] J. Gascon, S. Aguado, F. Kapteijn, *Micropor. Mesopor. Mater.*, **2008**, *113*, 132

[78] H. Guo, G. Zhu, I. Hewitt, S. Qiu, *J. Am. Chem. Soc.*, **2009**, *119*, 1646

[79] J. Rowsell, O. Yaghi, *J. Am. Chem. Soc.*, **2006**, *128*, 1304

[80] G. Keller, *Chem. Eng. Prog.*, **1995**, 11

[81] H.-G. Fritz, J. Hammer, *Chem. Ing. Tech.*, **2005**, *77*, 1588

[82] C. Trefzger, *"Herstellung zeolithischer Wabenkörper"*, Thesis, **2003**

[83] U. Hammon, *"Methanolumsetzung zu Olefinen an Zeolith ZSM-5 - Verfahrens- und Kontaktgestaltung"*, Thesis, **1987**

[84] W. Mitchelle, W. Moore, U.S. Patent 2.973.327, *Bonded Molecular Sieves*, **1961**, Union Carbide Corporation, New York

[85] R. Wusirika, I. Morris, European Patent EP 0 706 824 A1, *Low Expansion Molecular Sieve and Method of Making the Same*, **1995**, Corning Inc., New York

[86] R. Lapasin, S. Pricl, *Rheology of Industrial Polysaccharides, Theory and Applications*, **1995**, Blackie Academic & Professional

[87] J. Schuetz, *Ceramic Bulletin*, **1986**, *65*, 12

[88] O. Töppel, *Prüfung von Pappe, Zellstoff und Holzstoff*, **1993**, Vol. 3, Springer Verlag, Heidelberg

[89] P. Küsgens, M. Rose, I. Senkovska, H. Fröde, A. Henschel, S. Siegle, S. Kaskel, *Micropor. Mesopor. Mater.*, **2009**, *120*, 325

[90] P. Küsgens, S. Siegle, S. Kaskel, *Adv. Eng. Mater.*, **2009**, *11*, 93

[91] S. Mintova, V. Valtchev, *Zeolites*, **1996**, *16*, 31

[92] V. Valtchev, S. Mintova, I. Vultchev, V. Lazarova, *Chem. Comm.*, **1994**, 2087

[93] C. Biermann, *Handbook of Pulp and Papermaking*, **1996**, Academic Press, San Diego

[94] TAPPI Standard Method T214, *Kappa Number of Pulp*

[95] I. Pearl, *The Chemistry of Lignin*, **1967**, Marcel Dekker Inc., New York

[96] K. Sarkanan, C. Ludwig, *Lignins*, **1971**, Wiley-VCH, New York

[97] S. Hermes, D. Zacher, A. Baunemann, C. Woll, R. Fischer, *Chem. Mater.*, **2007**, *19*, 2168

[98] S. Hermes, F. Schröder, R. Chelmowski, C. Woll, R. Fischer, *J. Am. Chem. Soc.*, **2005**, *127*, 13744

[99] J. Oh, W. Shim, J. Lee, J. Kim, H. Moon, G. Seo, *J. Chem. Eng. Data*, **2003**, *48*, 1458

[100] M. Gruszkiewicz, J. Simonson, T. Burchell, D. Cole, *J. Therm. Anal. Calor.*, **2005**, *81*, 609

[101] A. Michaelides, S. Skoulika, E. Bakalbassis, J. Mrozinsky, *Crys. Growth & Des.*, **2003**, *3*, 487

[102] A. Kondo, T. Daimaru, H. Noguchi, T. Ohba, K. Kaneko, H. Kanoh, *J. Coll. Inter. Sci.*, **2007**, *314*, 422

[103] Q. Fang, G. Zhu, M. Zue, Q. Zhang, J. Sun, X. Guo, S. Qiu, S. Xu, P. Wang, D. Wang, Y. Wei, *Chem. Eur. J.*, **2006**, *12*, 3754

[104] X. Lin, A. Blake, C. Wilson, X. Sun, N. Champness, M. George, P. Hubberstey, R. Mokaya, M. Schröder, *J. Am. Chem. Soc.*, **2006**, *128*, 10753

[105] J. Castillo, T. Vlugt, S. Calero, *J. Phys. Chem.*, **2008**, *112*, 15934

[106] Y. Cheng, A. Kondo, H. Noguchi, H. Kajiro, K. Urita, T. Ohba, K. Kaneko, H. Kanoh, *Langmuir*, **2009**, *25*, 4510

[107] K. Park, Z. Ni, A. Coté, J. Choi, R. Huang, F. Uribe-Romo, H. Chae, M. O'Keeffe, O. Yaghi, *Proc. Natl. Acad. Sci.*, **2006**, *103*, 10186

[108] P. Horcajada, S. Surblé, C. Serre, D.-Y. Hong, Y.-K. Seo, J.-S. Chang, J.-M. Grenèche, I. Margiolaki, G. Férey, *Chem. Comm.*, **2006**, *27*, 2820

[109] R. Werneke, *Industrielle Feuchtemessung: Grundlagen, Methoden, technische Anwendungen*, **2003**, Weinheim, Wiley-VCH

[110] D. Townsend, A. Blackwood, E. Howard, *SAE Tech. Paper Series*, **1999**, *1999-01-3774*

[111] SAE Standard J 2384, *Air Dryer Test Procedure*, **2006**

[112] F. Förster, *Das Buch vom Erdöl*, **1967**, Hamburg, BP Petroleum Benzin und Aktiengesellschaft

[113] F. Wang, K. Qian, L. Green, *Anal. Chem.*, **2005**, *77*, 2777

[114] S. Junlong, H. Guangxiang, L. Tonglin, *Petrochem. Ind. Tech.*, *Journal written in chinese*, **2008**, *15*, 15

[115] D. Eaves, P. Sewell, *I&EC Pro. Des. Dev.*, **1964**, *4*, 361

[116] J. Gu, W. Lu, L. Jiang, H. Zhou, T. Lu, *Inorg. Chem.*, **2007**, *46*, 2835

[117] C. Serre, F. Millange, C. Thouvenot, M. Nogues, G. Marsoulier, D. Louer, G. Férey, *J. Am. Chem. Soc.*, **2002**, *124*, 13519

[118] Mettler Toledo, *Grundlagen für die coulometrische Karl-Fischer-Titration*, Applikationsbroschüre 32

A. Acknowledgement

In dem Zeitraum der Promotion wurde ich von vielen Menschen in unterschiedlichen Bereichen unterstützt und möchte mich hier herzlich dafür bedanken.
Besonderer Dank gilt:

Prof. Dr. Stefan Kaskel für die stete Unterstützung und die wissenschaftliche Betreuung dieser Arbeit.

Prof. Dr. Vladimir Reschetilowski vom Institut für Technische Chemie für die freundliche Übernahme des Zweitgutachtens.

Dr. Sven Siegle für die Betreuung der Arbeit bei der MAHLE Filtersysteme GmbH.

Prof. Dr. Ing. Hans-Gerhard Fritz und **Alina Zgaverdea** vom Institut für Kunststofftechnologie der Universität Stuttgart für die Hilfe bei der Herstellung der $Cu_3(BTC)_2$ Monolithe.

Dr. Michal Sabo für viele hilfreiche Diskussionen und Unterstützung während meiner ersten Zeit an der TU Dresden.

Marcus Rose, Nicole Klein und **Dr. Irena Senkovska** für die Unterstützung bei den Messungen und vielen fruchtbaren Diskussionen. Dem gesamten **AK Kaskel** für die freundliche Aufnahme in den Arbeitskreis während meiner Aufenthalte in Dresden.

Aleksandar Radlovic für die Hilfe bei allen Arbeiten rund um den Lufttrockn-erprüfstand bei der MAHLE Filtersysteme GmbH.

Joachim Reichle, Eva Martinez und **Christina Schulte** von der MAHLE International GmbH für die personelle Betreuung und die Bereitstellung dieser Stelle.

Der gesamten Abteilung **LDL** bei der MAHLE Filtersysteme GmbH für ein tolles Arbeitsklima in den letzten drei Jahren.

Meinen Doktorandenkollegen **Eike Stitterich, Thomas Deuß** und **Eva Popp** für viele kurzweilige Stunden und Abende während dieser drei Jahre.

Meinen Eltern, Geschwistern und Verwandten, die alle auf Ihre Weise zu dem Gelingen dieser Arbeit beigetragen haben.